Doctoral Dissertation

Numerical Simulation on High-frequency Mechanical Impact Treated Gusset Welded Joints and the Local MIL-HDBK-5D Equivalent Stress Based Fatigue Assessment

(高周波機械衝撃処理を施したガセット溶接継手の数値解析と MIL-HDBK-5D 等価応力に基づく局所疲労評価)

DAI PEIYUAN

June 2023

Graduate School of Engineering,
Osaka University

A Dissertation for Doctor of Engineering Degree submitted to

Osaka University

Graduate School of Engineering

Division of Global Architecture

Department of Naval Architecture and Ocean Engineering

in
June 2023

Supervised by
Professor Naoki Osawa

Committee members

Professor Kazuhiro Iijima

Graduate School of Engineering, Osaka University

Professor Ninshu Ma

Joining and Welding Research Institute, Osaka University

Abstract

Fatigue enhancement by High-frequency Mechanical Impact (HFMI) treatment mainly arises from the introduced compressive residual stresses (RS), local grain refinement, and weld toe geometry improvement. The improvement effects from compressive RS are diminished depending on the fluctuation range and stress ratio of the fatigue load.

However, existing local stress based methods, such as nominal stress, structural hot-spot stress, and effective notch stress approaches, are unable to quantitatively consider HFMI-induced RS, local work hardening, and the behavior of stress relaxation under fatigue loading. This means that numerous fatigue tests are necessary to obtain S-N curves for each process condition when investigating the effect of HFMI process parameters (such as the peening indentation, peening tool radius, peening angle, and peening frequency) on fatigue improvements.

This study proposes a multi-process numerical simulation model to estimate local RS and improved shape profiles induced by HFMI treatment in welded joints. HFMI-treated flat plate and out-of-plane gusset welded joint specimens are fabricated using SM490 steel. The surface topography for the treated zone, RS before and after the HFMI process, and thermal cycles during the welding process are experimentally investigated to calibrate and validate the proposed simulation approach. Both simulated local deformed shape profiles and RS are in good agreement with the measurements.

A local MIL-HDBK-5D equivalent stress (LMES) based fatigue assessment approach is then proposed to investigate the fatigue life of the out-of-plane gusset welded joints made of SM490 steel considering the means stress effect. The LMES range is identified by the elastic-plastic local stress cycle (EP-LSC) which is simulated by the muti-process finite element (FE) analysis including welding, post-weld treatment (including Post-weld heat treatment or HFMI), and fatigue load process. The LMES distribution suggests a shift of the crack initiation site in the HFMI groove with an increasing external fatigue load. Based on the maximum LMES range of each specimen, nominal S-N data for as-welded (AW) and HFMI specimens are consolidated into a single curve. This LMES based S-N curve can be used for evaluating fatigue life comprising the influence of HFMI-induced RS, cyclic stress relaxation, and local weld toe geometry welded joints studied in this work.

Acknowledgments

Three years of doctoral studies are coming to an end. First of all, I would like to express my sincere appreciation to my supervisor, Prof. Naoki Osawa, for his professional and detailed guidance in my research work. I am very appreciative of the opportunity he gave me to join the laboratory of Ocean Material Engineering of the Department of Naval Architecture and Ocean Engineering of Osaka University. In this laboratory, I can work on the research project that interests me - the fatigue assessment of welded structures, which will have long-term implications for my future career development.

I would like to express my sincere gratitude to Prof. Sherif Rashed for his guidance in dynamics explicit FE analysis. Prof. Sherif Rashed is extremely responsible and always guided me attentively and carefully step by step to complete my research work.

I am very grateful to Dr. Donghui Ma for his help in the experiments including welding, residual stress measurement, and fatigue tests. His wide experience and knowledge in welding fatigue research have helped me complete this dissertation successfully. I also acknowledge Dr. Yukihide Yoshihara for the fatigue test data of PWHT joints.

Finally, I would like to thank the members of Prof. Osawa's laboratory, and the members of the Technical Research Institute in Hitachi Zosen Corporation. I also thank my family and friends for their long-term support. Without all your help, this dissertation could not have been completed.

DAI PEIYUAN

Table of Contents

CHAPTER 1

Background

1.1 Factors affecting fatigue of welded joints

Fatigue is a common mode of structural damage [1-2]. When a structures is subjected to cyclic loading, the repeated stress cycles cause microscopic cracks to initiate and propagate within the material. These cracks gradually grow in size with each stress cycle until they reach a critical size, at which point catastrophic failure can occur without any significant deformation or warning signs. For welded structures, the vicinity of the weld bead, such as the weld toe and weld root, is more likely to be the crack initiation site due to geometric discontinuities or welding defects [3]. Since the welded joint is usually a weak point of the entire structure, researches on fatigue failure in welded structures has attracted extensive attention from industry and academia for over a century [4]. There are many factors which affect the fatigue of welded joints including the weld shape, weld imperfection, size effects, residual stresses, and Material properties.

1.1.1 Weld shape

Weld toe is the junction of the plate face and weld metal. The abrupt change in cross-section shape near the weld toe leads to uneven stress distribution along the thickness direction when the welded structure is subjected to external loads, as shown in Fig. 1.1. The magnitude of the peak stress depends the several factors, such as the weld type, dimension of structures, and toe radius [5]. For example, a fillet weld usually has more severe stress concentration compared with that of a butt weld; a smooth weld toe with a larger toe radius can help reduce stress concentrations and enhance fatigue performance [6-9].

Some of the joints, such as shown in Fig 1.1 (b), has another feature called weld root which also causes stress concentrations due to geometric discontinuities [10-12]. For partial penetration welds, weld root is similar to a pre-existing crack if it is transverse to the external loading. In such case, weld root can be more severe than weld toe and become the crack initiation site. Since post-weld treatments, such as the peening treatment and TIG dressing, are hard to be applied at weld root, the potential risk of root-caused failure should be diminished by mean of reasonable weld design and welding processes [13].

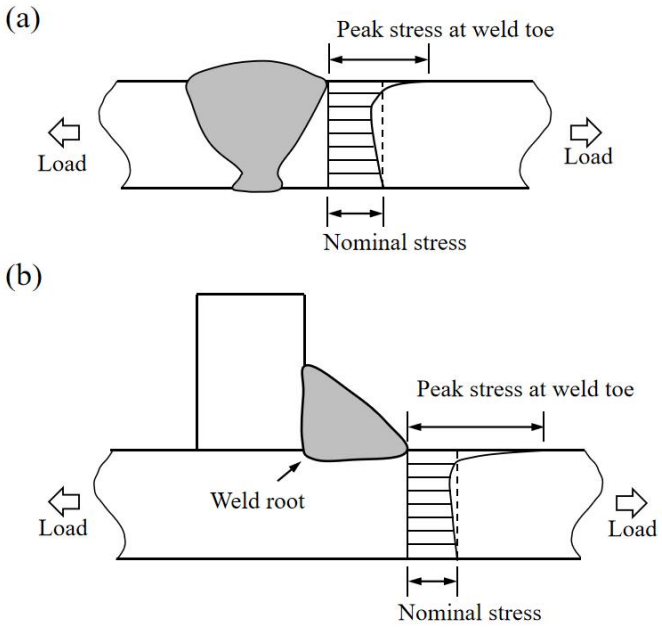

Fig. 1.1 Stress concentration at weld toe for (a) the butt joint and (b) T-joint

1.1.2 Weld imperfection

Weld imperfections are widely present in practical welded structures [14,15]. From the aspect of fatigue, these imperfections can be divided into two categories: welding flaw and misalignment [16,17]. Typical welding flaws include the lack of fusion, incomplete penetration, undercut, under filled, overlap, porosity, etc. These defects can also cause stress concentrations, similar to the action of weld toe and root. If a welding flaw becomes the region with most severe stress concentration, for welded structures, fatigue cracks will be prone to initiate at this flaw and thus reduce the fatigue strength. In addition, the structure with a high fatigue performance is more sensitive to weld flaw [4,5]. For example, the butt joints, especially for those subjected to the grinding process, has a relatively smooth weld toe shape. Therefore, the stress concentration at weld flaw is more likely to exceed that at weld toe and become a crack initiation site.

Misalignment, including axial misalignment and angular distortion shown in Fig. 1.2, is another important weld imperfection which affects the fatigue performance. When an axial load is applied to the welded joint, misalignment leads to the introduction of local secondary bending stress, thus reducing fatigue life [18,19]. This secondary bending stress does not cause new crack initiation site, but increase the severity of existing defects (such as welding flaw , weld toe, and weld root). In addition, the effect of misalignment on fatigue life is slight under purely bending load.

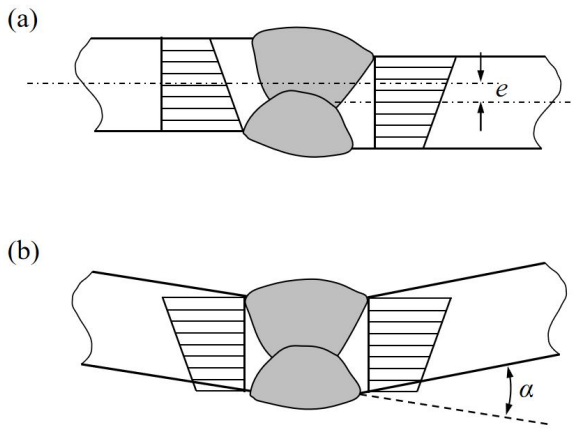

Fig. 1.2 Misalignment in welded joint. (a) Axial; (b) Angular.

1.1.3 Size effects

In general, the fatigue strength of a structure decreases with increasing size [20]. For non-welded parts, the large size means an increased probability of defects and an increased severity of stress concentrations due to geometry. For welded structure, size effects are mainly associated with geometry-related stress concentrations. The magnitude of stress concentration at the weld toe increases and thus reduces the fatigue performance, with the increasing dimensions of the welded joint such as plate thickness and attachment length. Existing design recommendations [21] or design guidelines [22] introduce a strength reduction factor γ_t to consider size effects if the plate thickness t is larger than t_0 = 16-25mm, as described in Eq.(1).

$$\gamma_t = \left(t_0 / t\right)^n \tag{1}$$

where t_0 is the plate thickness corresponding to design S-N curve; t is the actual plate thickness; n is the exponent depending on the type of weld detail.

1.1.4 Residual stresses

Welding residual stresses are inevitably introduced into the vicinity of the heat-affected zone (HAZ) after welding, due to the non-linear plastic behavior of the material caused by rapid local heating and cooling [23, 24]. Welding residual stress usually presents high tensile stresses, especially for structures with thick dimensions [25,26]. These tensile stresses increase the level of the mean stress under dynamic loading and thus reduces the fatigue strength of the structure [27].

Although tensile residual stress is considered to be a harmful factor for the fatigue strength of a structure, there is usually no need to consider residual stresses specifically in the structure design, as their effects are already included in the design S-N curve. However, for stress relieved components with negligible residual stress, the beneficial effects of residual stress reduction may not be ignored [21]. In such cases [5], the permissible stress ranges depend on mean stress (expressed by stress ratio *R*), as shown in Fig. 1.3. For fully tensile load (R>0), the fatigue data from stress-relieved joints are virtually the same as that of as-welded joints, while a considerable difference in fatigue performance is observed for cases with R<0.

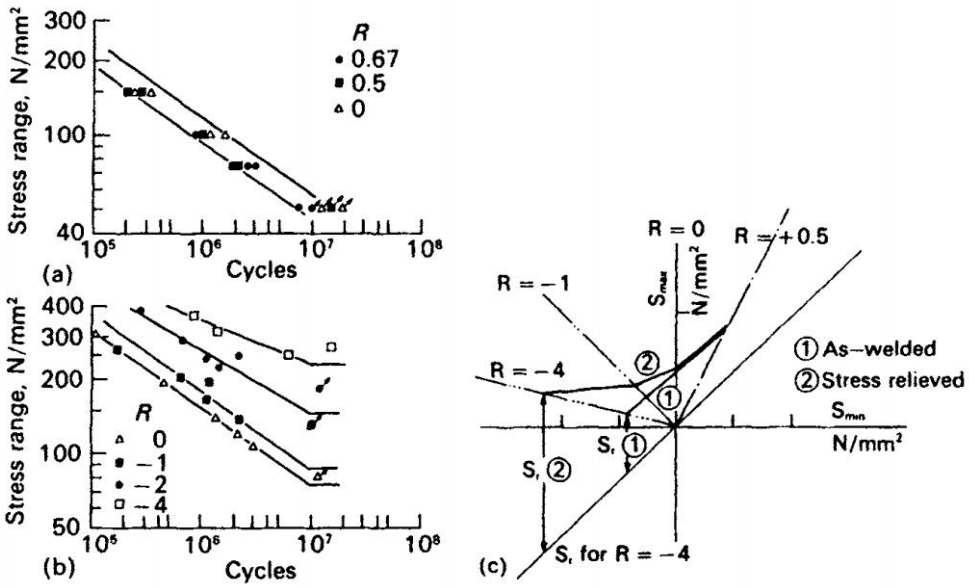

Fig. 1.3 Fatigue tests results of stress-relieved fillet welds in steel for (a) $R > 0$, (b) $R < 0$. (c) Fatigue strengths at 2×10^6 cycles for as-welded and stress-relieved joints [5].

1.1.5 Material properties

The influence of material properties on material fatigue strength is mainly manifested in the crack initiation phase. For non-welded materials with a smooth surface, the crack initiation life is a dominant part of the total fatigue life [2, 28]. Therefore, their fatigue strength normally increase with the material tensile strength. However, the tensile strength of materials has a slight effect on fatigue life for as-welded joints [29, 30]. This is due to the facts that there are always unavoidable defects in the welded structure (such as weld flaws, weld toe, and root) and the crack initiation life of welded components made of high strength steel is sensitive to notch effects which offset the beneficial effect of tensile strength on fatigue. In addition, the rate of crack propagation is relatively insensitive to microstructure

and material tensile strength. This means that the usage of high-strength steels can not improve the fatigue strength in the crack propagation phase.

1.2 High Frequency Mechanical Impact (HFMI) treatment

1.2.1 Overview of HFMI treatment

To enhance fatigue performance, several post-weld improvement techniques are developed and applied in industrial manufacturing [31]. As mentioned in section 1.1, there are many factors that affect fatigue life. Herein, the residual stress factor and the weld shape factor are relatively facilitate to control actively after welding. Post-weld improvement techniques can also be characterized as two types: residual stress methods and weld geometry improvement methods, as shown in Fig. 1.4.

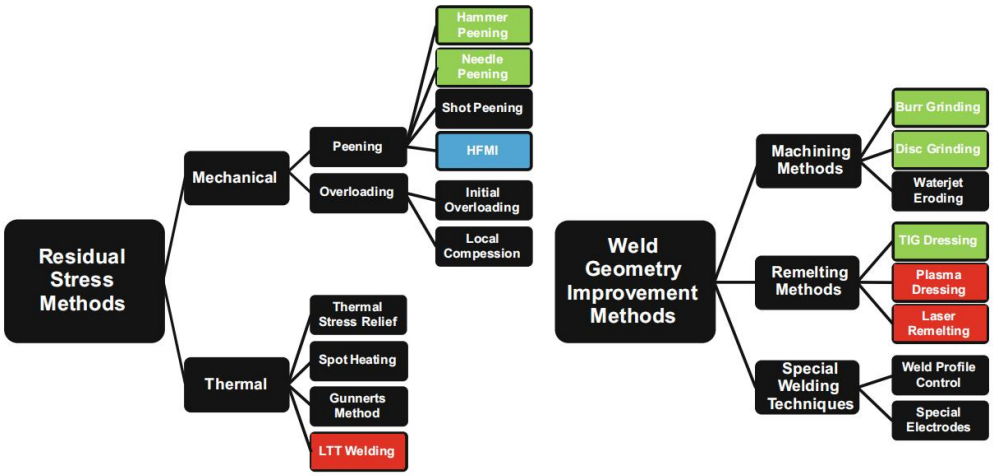

Fig. 1.4 Overview of different weld improvement techniques [31].

Among these post-weld improvement techniques, High-frequency Mechanical Impact (HFMI) treatment is developed as a new post-welded technique and has shown tremendous potential for fatigue life improvement [32-33]. This treatment has attracted the interest of both industry and research institutions due to its dependability, efficiency, and user-friendliness. Recommendations from International Institute of Welding (IIW) [33] use the term of HFMI treatment to describe a variety of related technologies, including ultrasonic impact (UIT), ultrasonic peening (UP), ultrasonic peening treatment (UPT), high frequency impact treatment (HiFiT), pneumatic impact treatment (PIT), and ultrasonic needle peeing (UNP). The HFMI peening system consists mainly of the peening gun and energy sources, as shown in Fig. 1.5. Despite the diverse power sources, the operating principles of these technologies are identical: a cylindrical pin is accelerated hit the weak points of the specimen with a high frequency (> 90 Hz) thus achieving fatigue life enhancement. The

appearance of the weld toe before and after HFMI treatment is shown in Fig. 1.6.

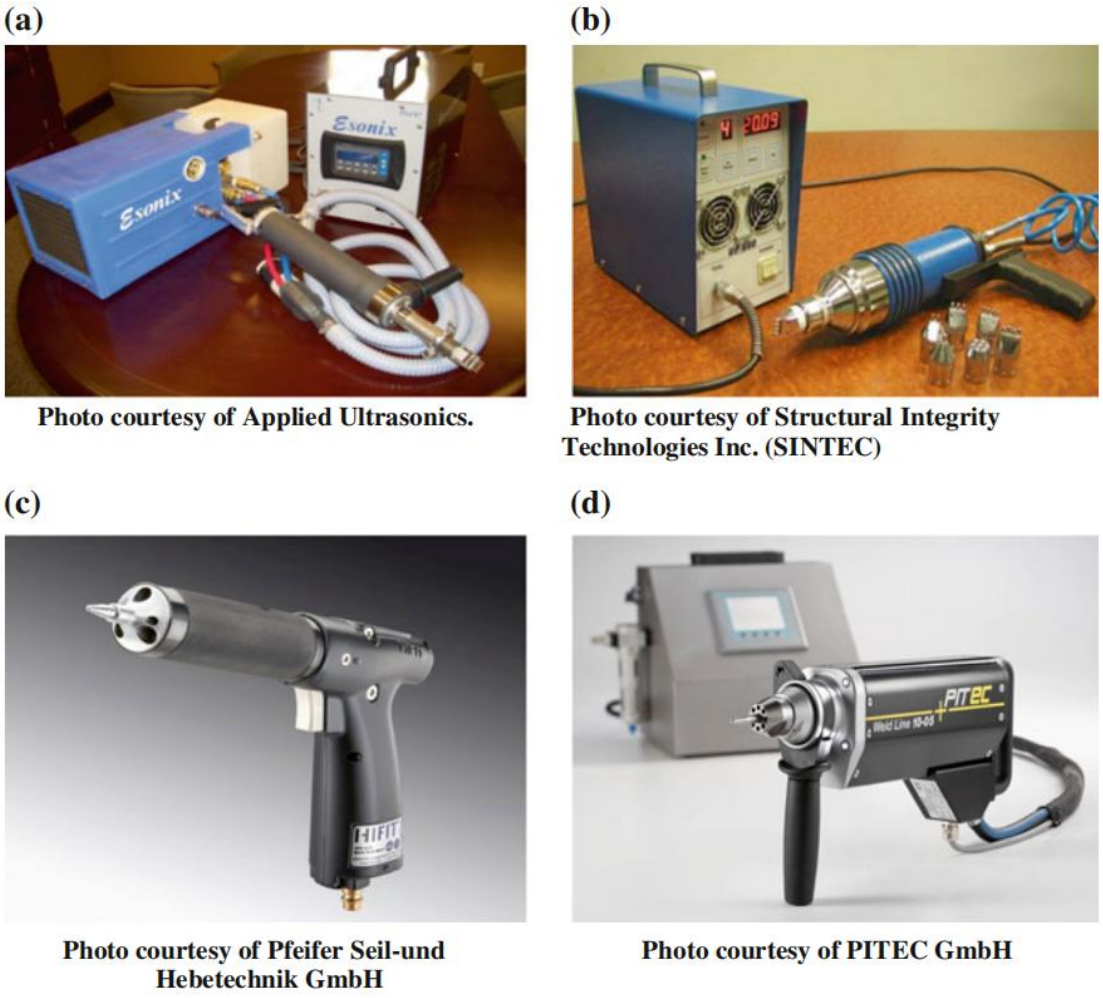

Fig.1.6 Typical HFMI devices available worldwide. (a) UIT, (b) UP, (c) HiFiT and (d) PIT.

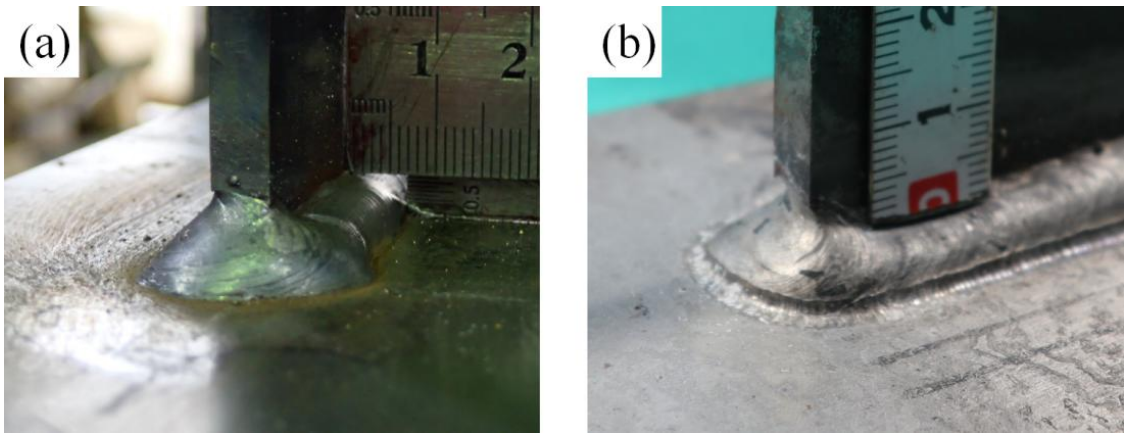

Fig.1.7 Appearance of weld toe. (a) As-welded toe, and (b) HFMI-treated toe.

1.2.2 Beneficial effects of HFMI treatment on fatigue improvement

It is known that HFMI treatment can improve the fatigue performance of welded joints.

International Institute of Welding (IIW) recommendation by Marquis and Barsoum [33] describes the HFMI-enhanced fatigue class as a function of the base materials' yield strength (f_y): approximately 12.5% increases in fatigue strength per 200MPa in f_y. The HFMI treatment provides the most significant fatigue strength improvement for structure steel with $f_y > 950$MPa, up to 8 FAT-class.

The favorable benefits of HFMI treatment on fatigue enhancement arise from the introduced compressive residual stresses (RS), local grain refinement, and weld toe geometry improvement. As-welded (AW) RS at the weld toe, which typically exhibits high tensile stress, can be replaced by HFMI-induced compressive RS. This compressive RS reduces the mean stress level under dynamic loading and improves the structure's fatigue resistance [2-3]. HFMI treatment can generate a strain-hardened layer and refine the microstructure of materials. Yamaguchi et al.[34] investigated the effects of local work hardening on fatigue performance using arc-welded ultra-high strength steel joints treated by micro-needle peening. They found that the twin boundary of lath martensite is prone to be a crack initiation site for AW joints; the peening process can change the microstructure near the weld toe, prevent crack initiation at the boundaries and enhance the fatigue toughness. Moreover, the weld toe geometry can be improved by HFMI treatment. The weld toe with a radius of < 1 mm is expanded into an HFMI groove with a typical depth of 0.2-0.6 mm and width of 3-6 mm [33], which reduces the stress concentration and thus improves fatigue performance.

1.2.3 Numerical investigation on HFMI Treatment

Many studies focused on numerical simulations of the HFMI-induced stress field using the finite element method (FEM). Baptista et al. [35] developed a full dynamic model of the hammer peening process based on finite element (FE) analysis code ABAQUS. The hammer peening load of 7 MPa was determined by using strain gauges that were glued on the hammer tool and then applied to the tool' model as an instantaneous load in explicit FE analysis. The fully dynamic model allows more complex simulations, such as primary impacts as well as secondary impacts that occur between each stroke, showing superiority over static models. This simulation method is termed force-controlled simulation (FCS) in the follow-up research. Hu et al. [36] established a 3-D dynamic FE model to analyze the elastic-plastic ultrasonic impact treatment (UIT) process of multiple impacts on the 2024 aluminum alloy. The influences of UIT parameters, such as impact velocity, pin diameter, feeding speed, and offset distances, on the RS distribution were investigated and the desired

RS can be obtained by optimizing the controlled parameters. Deng et al. [37] studied the effects of HFMI-induced RS on fatigue improvement for butt joints using a structural hot spot stress approach. The stress distribution at the vicinity of the treated weld toe was simulated by a 3-D FE model using the FCS method. The initial velocity determined by a high-speed video camera was applied in HFMI simulation. Ernould et al. [38] proposed a method for characterizing the pin kinetic during the HFMI treatment. The contact force and hammer frequency are measured with strain gages, and both primary and secondary impacts were considered in the simulation. Schubnell et al. [39] introduced a process parameter, coverage value, to quantify the process quality for HFMI treatment. They investigated the influence of this parameter on RS state and work hardening for flat specimens with different steel grades. The simulation work was performed using the commercial software Abaqus and VUAMP user subroutine.

An alternative method of the FCS for HFMI analysis is called displacement-controlled simulations (DCS) [40]. In the DCS, the peening tool is modeled as a rigid body, and its displacement is set during the treatment. The axial movement of the tool is usually simplified as sinusoidal motion ignoring secondary impacts [41]. Foehrenbach et al. [42] compared the HFMI-induced RS obtained by the FCS with those given by the DCS as well as with the measured RS by the neutron diffraction method, using HFMI-treated S355J2H2 flat plates. The two methods show similar predicted accuracy of RS, but the calculation time of FCS was about 3 to 4 times longer than that of the DCS. In addition, FCS needed more input parameters: impact velocity and contact force, which increased the cost of usage. Khurshid et al. [43] investigated RS induced by UIT in S355, S700MC, and S960 grades streel experimentally and numerically. The DCS was carried out considering the effect of different materials models. The results revealed that simple isotropic hardening models and strain rate-dependent isotropic hardening models can sufficiently estimate the RS state to a depth of less than 0.8 mm. Banno et al. [44] numerically investigated the influence of under and over-treatment on the RS state induced by HFMI. It was observed that a high feed rate of treatment can influence the RS state near the treated surfaces, and the increasing hits were independent of the amount of RS for over-treatment conditions.

Recent works focused on the RS relaxation or stability in HFMI-treated welds after single or multiple cyclic external loads. Although the beneficial effects of HFMI treatment are related to induced-compressive RS, the values can be reduced when the sum of the local RS and external load exceeds the fy of materials. Hence, it is needed to also consider the RS

relaxation under the external load while assessing the benefits of HFMI for the treated structures. Leitner et al. [45] studied the effect of cyclic loading on compressive RS fields induced by HFMI post-weld treatment using mild steel S355 and high-strength steel S960 specimens. They performed the first five load-cycles simulations and compared the simulated RS with that of X-ray measurement. It was shown that RS relaxation mainly occurs during the first cycle and the change of RS within 2-5 cycles can be ignored. Schubnell et al. [46] compared RS relaxation under single tension and compression overloads for HFMI-treated joints made of different grades of steel. High compression loads lead to full RS relaxation at the weld toe of S960QL and moderate relaxation for S355J2, while High tension loads lead only to slight relaxation. Ruiz et al. [47] performed HFMI and cyclic loading simulations of out-of-plane gusset welded joints to investigate the RS relaxation under constant amplitude and compressive spike loads with various amplitudes. The recommendations on RS relaxation simulation were presented in their work.

It has so far been a challenge to develop a practical and efficient numerical analysis system for estimating HFMI-induced RS in welded structures, although the analytical framework for HFMI simulations has been established. The balance between accuracy and efficiency of calculation is an important issue in numerical studies. As mentioned above, a reliable prediction of RS fields can be obtained by detailed FE modeling, such as the use of fine FE meshes, complex material hardening models, accurate pin motion, and contact force. However, such a simulation model needs more computational cost and numerous analytical parameters, making it difficult to solve engineering problems, especially for large welded structures.

1.2.4 Fatigue assessment approach for HFMI-treated joints

IIW recommendations [21,33] provide several assessment approaches of fatigue life based on the nominal, structural hot-spot, and effective notch stresses. The improvement effect of HFMI treatment is taken into account by introducing an enhancement factor and modifying the slope of design S-N curves. The FAT classes of design curves are described as functions of stress ratio and yield stress. However, these approaches need to be calibrated by a large amount of fatigue test data and sometimes lead to overly conservative assessments. Yildirim et al. [48, 49] examined all available experimental data on the fatigue strength of HFMI-treated joints by using the effective notch stress approach and the structural hot-spot stress approach. They found that the existing IIW characteristic curve is conservative with respect to more than 95% of available fatigue test data. Further research

[50-53] has validated this view. In addition, these methods are unable to quantitatively consider HFMI-induced RS and the behavior of stress relaxation under fatigue loading. This means that numerous fatigue tests are necessary to obtain S-N curves for each process condition when investigating the effect of HFMI process parameters (such as the peening indentation, peening tool radius, peening angle, and peening frequency) on fatigue improvements. It will significantly increase the period and cost of industrial product design.

The fracture mechanical approach is an alternative way to estimate the fatigue life of HFMI-treated joints [53-55]. HFMI-induced local RS and deformed shape profiles are obtained by 3-D finite element (FE) analysis. Then, the weight function approach is applied to calculate the SIF value considering the RS on the crack face. The crack propagation life is calculated based on fatigue crack growth laws. Although the fracture mechanics based approach can predict the fatigue life considering the RS, it has a more complicated calculation process and is therefore difficult to apply to practical problems. Furthermore, it is hard to create a FE mesh with cracks considering the deformed shape caused by HFMI and to determine the size of the initial crack.

1.3 Mean stress effect correction methods

Even if the materials are subjected to the same stress range, different mean stress level can lead to can lead to variations in fatigue strength. It is known that the tensile residual stress increases the mean stress level of the fatigue cycle, resulting in a reduction in the fatigue life of structures. Therefore, mean stress analysis is necessary to quantitatively evaluate the effect of residual stress on fatigue strength of welded structures. Several mean stress analysis methods are presented in this section.

1.3.1 Goodman approach

The most well-known correction method of mean stress effect is Goodman relation [56-58] (also called Goodman diagram). This relation can be described by the following equation:

$$\sigma_a = \sigma_w \left(1 - \frac{\sigma_m}{\sigma_T}\right) \tag{2}$$

where σ_a is the stress amplitude for fatigue loading with a nonzero mean stress; σ_w is the stress amplitude for completely reversed loading; σ_m is the mean stress of fatigue loading; σ_T is the ultimate tensile strength of the material. This equation characterizes a linear

relationship between the mean stress and the permissible fatigue stress range.

1.3.2 IIW recommendation approach

IIW [33] provides a fatigue strength modification method considering the effect of residual stresses state and mean stress effects (expressed by the stress ratio R) based on the fatigue enhancement factor $f(R)$. This factor $f(R)$ can be used to correct the FAT class of design S-N curve, so that the effect of residual stresses can be taken into account. Three cases are distinguished based on structural characteristics and stress conditions.

(1) Un-welded structure with negligible residual stress (< 0.2 f_y) or stress-relived welded components; The effects of constraints and secondary stress has been fully consideration in analysis; No constraints in assembly.

$$f(R)=\begin{cases}1.6 & ,R<-1\\ -0.4R+1.2 & ,-1\le R\le 0.5\\ 1 & ,R>0.5\end{cases} \tag{3}$$

(2) Small-scale and thin-well structures with short welds; Un-welded structures with thermal-cut edges; No constraints in assembly.

$$f(R)=\begin{cases}1.3 & ,R<-1\\ -0.4R+0.9 & ,-1\le R\le 0.25\\ 1 & ,R>0.25\end{cases} \tag{4}$$

(3) Two- or three-dimensional welded components; Thick-wall welded structures; Components welded with strong external constraints.

$$f(R)=1 \tag{5}$$

1.3.3 MIL-HDBK-5D approach

For load-control fatigue data, MIL-HDBK-5D Standard [59] provides an approach to consolidate the S-N data of aluminum alloy materials at various stress ratios based on an equivalent stress parameter $\Delta\sigma_{\text{n-eq}}$. The new S-N curve is described by the following equation:

$$\Delta\sigma_{\text{n-eq}}=\sigma_{\max}\left(1-R\right)^{\alpha} \tag{6}$$

$$\log N=c_1+c_2\log\Delta\sigma_{\text{n-eq}} \tag{7}$$

where $\sigma_{\max}$ is the maximum value in the nominal stress cycle; R is the stress ratio; N is the

number of cycles to failure; c_1, c_2, and α are material parameters.

Matsuoka et al.[60, 61] investigated the fatigue crack initiation life of welded joints using the MIL-HDBK-5D approach. The hot-spot stress component based equivalent stress range $\Delta\sigma_{h\text{-}eq}$ can be described as the following equation:

$$\Delta\sigma_{\text{h-eq}} = (K\Delta\sigma)^{\alpha}\left(K\Delta\sigma_{\max} + \sigma_{\text{RS}}^{*}\right)^{1-\alpha} \tag{8}$$

$$\sigma_{\text{RS}}^{*} = \begin{cases} f_{\text{y}} - K\Delta\sigma_{\max} & ;\ f_{\text{y}} < K\Delta\sigma_{\max} + \sigma_{\text{RS}} \\ \sigma_{\text{RS}} & ;\ \text{otherwise} \\ -f_{\text{y}} - K\Delta\sigma_{\min} & ;\ -f_{\text{y}} > K\Delta\sigma_{\min} + \sigma_{\text{RS}} \end{cases} \tag{9}$$

where f_{y} is the yield stress; K is the structural stress concentration factor; $\Delta\sigma$ is the nominal stress range; $\sigma_{\min}$ is the minimum stress in the fatigue cycle; σ_{RS} is the residual stress; σ^{*}_{RS} is the stabilized residual stress. Stress relaxation is determined by the yield strength of materials and the hot-spot stress. Eq. (9) explains the variation in the RS due to fatigue loading. In their study, a series of fatigue test data in AW conditions were analyzed. The welding RS for each specimen was estimated by the inherent strain method. Matsuoka utilized the least squares method to fit the material parameter α = 0.6485 in Eq. (8).

1.4 Problem statement

1.4.1 HFMI simulation

It has so far been a challenge to develop a practical numerical analysis system for estimating HFMI-induced RS in welded structures. In the actual HFMI processing, the movement of the pins is complex and random. So far, there was no consensus on how to determine the parameters involved in the HFMI simulation, although the analytical framework has been established during the last decade.

The notch radius at the weld toe or HFMI groove affects the stress concentration as well as the fatigue performance. Therefore, accurate simulation of the shape profile of HFMI groove is essential for the complete fatigue life assessment system which can consider the fatigue improvement by HFMI. However, few studies have presented the simulated shape profile at HFMI-treated weld toe and its validation, and they focused mainly on the HFMI-induced RS.

The balance between accuracy and efficiency of calculation is an important issue in numerical studies. Ultra-fine mesh is necessary for HFMI simulation to calculate dramatically altered stresses at the treated regions. On the other hand, welding RS needs to

be taken into account as an initial condition for HFMI analysis. Previous researchers have used the same ultra-fine mesh in welding analysis as in HFMI simulation, which results in an unnecessary waste of computational resources making it difficult to solve engineering problems, especially for large welded structures.

1.4.2 Fatigue assessment of HFMI-treated joints

IIW recommendations provide several assessment approaches of fatigue life based on the nominal, structural hot-spot, and effective notch stresses. The improvement effect of HFMI treatment is taken into account by introducing an enhancement factor and modifying the slope of design S-N curves. The FAT classes of design curves are described as functions of stress ratio and yield stress. However, these approaches need to be calibrated by a large amount of fatigue test data and sometimes lead to overly conservative assessments.

In addition, these methods are unable to quantitatively consider HFMI-induced RS and the behavior of stress relaxation under fatigue loading. This means that numerous fatigue tests are necessary to obtain S-N curves for each process condition when investigating the effect of HFMI process parameters (such as the peening indentation, peening tool radius, peening angle, and peening frequency) on fatigue improvements. It will significantly increase the period and cost of industrial product design.

1.5 Objective and Framework

1.5.1 Specific objectives

Given the literature gap, this first objective of this study is to propose a multi-process numerical simulation model to estimate local RS and improved shape profiles induced by HFMI treatment in welded joints. Firstly, the welding simulation is performed by thermal-elastic-plastic finite element (TEPFE) analysis using a coarse finite element (FE) mesh model. The zooming technique is then applied to transfer simulated as-welded RS to the ultra-fine mesh used in HFMI analysis as initial stresses. Finally, the numerical analysis of HFMI-induced RS is carried out using the optimized displacement-controlled numerical simulation method. An HFMI-treated out-of-plane gusset welded joint specimen was fabricated using SM490 steel. The surface topography for the treated zone, RS before and after the HFMI process, and thermal cycles during the welding process were experimentally investigated to calibrate and validate the proposed simulation approach.

The second objective is to propose a local MIL-HDBK-5D equivalent stress (LMES) based fatigue assessment approach to investigate the fatigue lives of HFMI-treated gusset

welded joints made of SM490. The LMES range is identified by the elastic-plastic local stress cycle simulated by the muti-process finite element analysis, including welding, HFMI, and fatigue loading processes. Using the LMES, Fatigue test results of AW and HFMI joints are consolidated into a single S-N curve. This LMES based S-N curve can be used for evaluating fatigue life comprising the influence of residual stress, cyclic stress relaxation, and local weld toe geometry for welded joints studied in this work.

1.5.2 Framework of the thesis

This thesis can be divided into six chapters.

1) In chapter 1, the background of this work is presented, including numerical simulation of HFMI treatment and the fatigue assessment approaches. The main objectives and framework of this thesis are also discussed.
2) In chapter 2, the numerical and experimental investigations of an HFMI-treated flat plate made of SM490 steel are performed to better understand the features of HFMI-induced residual stresses and local shape profile. A dynamic explicit elastic-plastic FE (EP-FE) model is developed based on the commercial FE code MSC. Dytran. Mesh sensitivity analysis is conducted to determine the suitable FE element sizes near the treated zone with a balance of computational accuracy and efficiency. The effects of HFMI parameters including peening length and indentation are investigated numerically. The recommendations of optimum simulation conditions are presented based on simulation results.
3) In chapter 3, a practical and efficient numerical simulation procedure for the HFMI treatment of welded joints is proposed. The local RS and shape profile are studied by performing thermal-elastic-plastic FE (TEPFE) welding and subsequent dynamic explicit FE (DEFE) HFMI analyses of the out-of-plane gusset welded joints. The zooming technique is employed, and the as-welded stress calculated by using a coarse FE mesh is transferred to the ultra-fine mesh as the initial loading of HFMI analysis. In HFMI analysis, an optimized DCS method is developed. The peening tool's FE mesh is modified so that the wide groove profile caused by the lateral movement of the tool can be simulated. The validation is carried out by comparing calculated HFMI groove profiles and the RS distributions with those measured by the 3-D Scanner and X-ray equipment.
4) In chapter 4, a local MIL-HDBK-5D equivalent stress (LMES) based fatigue assessment approach is proposed. This new stress parameter called LMES is calculated based on

local elastic-plastic stress cycle, which allows quantitative assessment of residual stress effect on fatigue life. To validated this approach, a set of as-welded and PWHT gusset joints is fabricated using SS400 steel, followed by stress measurements and bending fatigue tests with stress ratios of R=-1. To obtain the stress distributions of specimens, welding, PWHT, and cyclic external load analysis were performed by using elastic-plastic finite element (FE) code JWEIAN. The mean stress effect related to RS is analyzed by using the equivalent stress parameter in MIL-HDBK-5D approach.

5) In chapter 5, the LMES range is employed as the stress parameter for fatigue assessment of HFMI-treated gusset joints. This stress parameter is identified from the local stress cycle along the surface of the HFMI groove for specimens subjected to cyclic loads. The local stress cycle is simulated by a muti-process simulation system including thermal-elastic-plastic FE (TEP-FE) welding analysis, dynamic explicit elastic-plastic FE (EP-FE) HFMI analysis, and EP-FE cycling loading analysis. To validate the proposed fatigue assessment approach, a set of AW and a set of HFMI out-of-plane gusset joints are fabricated using SM490 steel, followed by uni-axial fatigue tests with stress ratios of R = 0. Combined with the simulated stress results, the LMES based S-N curve is calculated, which enables a quantitative evaluation of the improvement effects of HFMI treatment.
6) In chapter 6, the overall summary of the thesis is presented. Recommendations for future research of fatigue assessment of welded structures improved by HFMI are also concluded.

CHAPTER 2

Numerical simulation of HFMI treatment on the flat plate

2.1 Introduction

To better understand the features of HFMI-induced residual stresses and local shape profile, an HFMI-treated flat plate made of SM490 steel (f_y=388 MPa) is investigated numerically and experimentally. A dynamic explicit elastic-plastic FE (EP-FE) model is developed based on the commercial FE code MSC. Dytran. The elastic-plastic behavior of materials during the HFMI treatment is considered using a non-linear isotropic hardening model.

The validity of the proposed HFMI simulation process is examined by comparing the results of flat plate peening obtained by numerical simulation with the experiment. The residual stress on the surface of the flat plate is measured by the X-ray diffraction method. The shape profile of the HFMI groove is measured by a laser scanner.

Mesh sensitivity analysis is conducted to determine the suitable FE element sizes near the treated zone with a balance of computational accuracy and efficiency. The effects of HFMI parameters including peening length and indentation are investigated numerically. The recommendations of optimum simulation conditions are presented based on simulation results.

2.2 Experimental work

A HFMI treated flat plate specimen of SM490 is used in this work, as shown in Fig. 2.1. The dimension of the specimen is 100×80×9 mm. The HFMI treatment is carried out by a robotic peening machine (see Fig. 2.1(a)) along a straight path of 80 mm with a travel speed of 10 mm/s and a hammering frequency of 80 Hz. A pin with a tip radius of 1.5 mm is applied in the peening process. The flat plate is held in place by bolts during HFMI treatment, as shown in Fig. 2.1(a). A 3-D laser-scanner equipment (LS100CN) is used to measure the peening indentation profile after treatment. To evaluate residual stress on the surface of specimen, the X-ray diffraction testing is employed with 2 mm measuring radius. The measurement location is shown in Fig. 2.1(b).

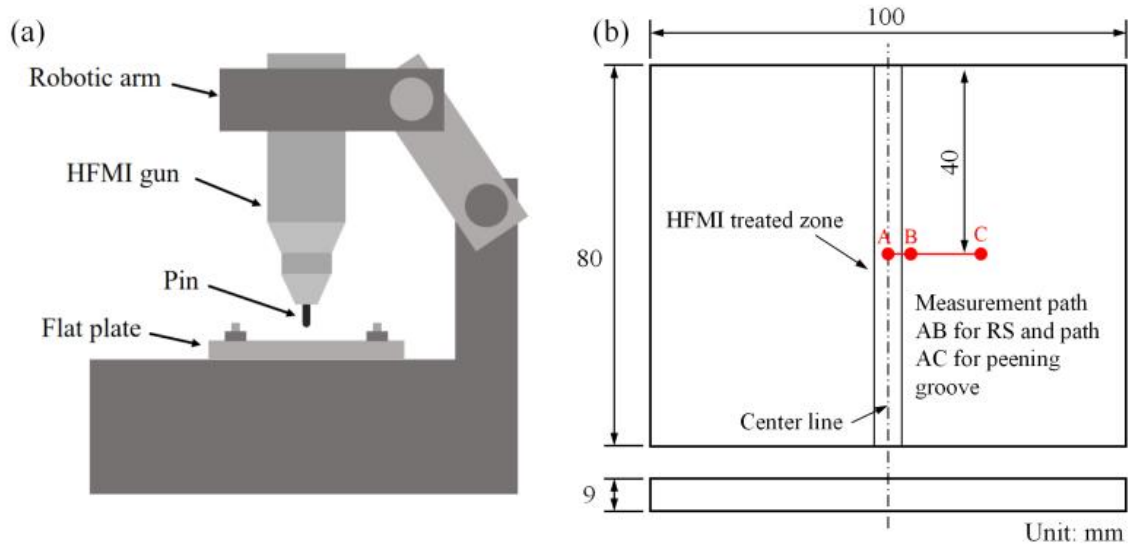

Fig. 2.1 (a) HFMI equipment, (b) geometry of flat plate specimen.

It should be noted that the mentioned experimental parameters do not follow strictly the IIW recommendations. However, the hammering treatment used in this work is still described as HFMI treatment since the processed result meets the IIW recommended value, e.g. 0.2 mm peening depth, which is shown in detail in subsequent sections.

2.3 Elastic-plastic dynamic FE analysis

A 3-D FE mesh using 8-node solid element is developed with the same geometry of the flat plate specimen, as shown in Fig 2.2. To save the computing time, only half of the flat plate (Y-Z plane as symmetric plane) is modeled due to the symmetry. The size of the smallest element in the vicinity of treated zone is 0.15×0.15×0.15 mm. For the rest of the mesh, the element size increases with the distance to treated zone in order to balance analysis efficiency and accuracy. A pin with a radius of 1.5 mm is meshed as a rigid surface, using 4-node 2-D shell element. In the HFMI analysis, all nodes on the lower back face and nodes near the hole used for fixed specimen are constrained in X, Y and Z direction. Symmetric boundary condition is applied on the Y-Z plane at the same time. The pin is constrained in X direction and X, Y, Z axis rotation, the displacement is controlled along the Y (flat motion) and Z (sine motion) direction for peening treatment. A contact pair is defined between the tool's tip (master surface) and the specimen (slave surface), using the penalty function method. The friction coefficient is set to be 0.3. It was reported that good agreement with RS measurement is achieved by performing partial length HFMI simulation [47]. To save analysis time, the peening length is set to 6mm in simulation.

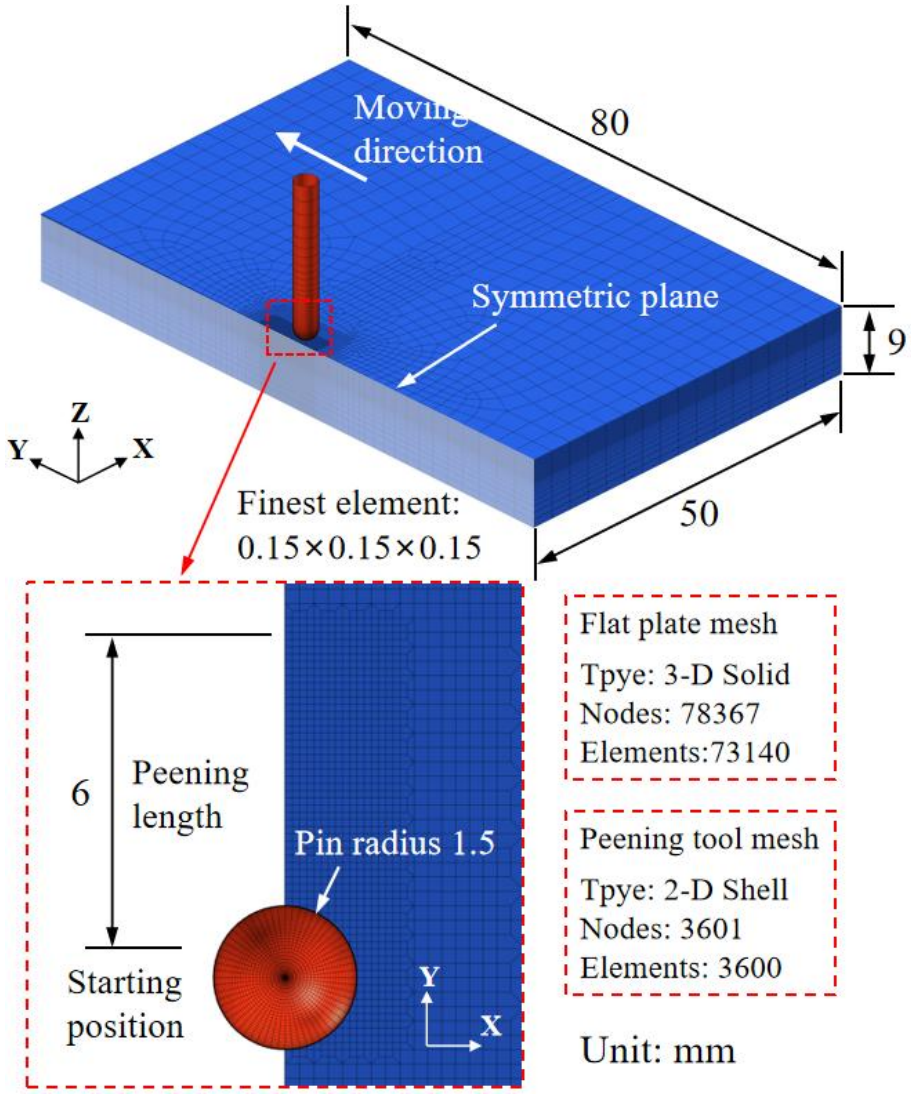

Fig. 2.2 FE mesh of the flat plate and peening tool.

Displacement-controlled (DC) simulations method is employed in this analysis due to easy access to analysis parameters and less computing time comparing with force-controlled (FC) simulations method. For DC simulations, the amplitude of pin displacement a is an essential parameter which is the sum of enforced indentation u_e and the distance between pin tip and upper surface of the specimen d, as shown in Fig. 2.3(a). However, it is different to directly obtain the enforced indentation u_e by measurements due to the elasticity of the material. One method is to investigate the relationship between u_e and u_p, and then calculate the u_e according to the experimental u_p. To determine the indentation in this study, four HFMI peening simulation cases with assumed u_e of 0.22, 0.25, 0.35 and 0.5 mm are performed, so that the fitted curve is obtained according to assumed u_e and simulated u_p, as shown in Fig. 2.3(b). The measured u_p is 0.209 mm, so the u_e is 0.234 mm from the fitted

curve. The distance d is assumed to be 1 mm and it is taken into account when creating the FE mesh model. Thus, the amplitude a is set to 1.234 mm in HFMI simulation.

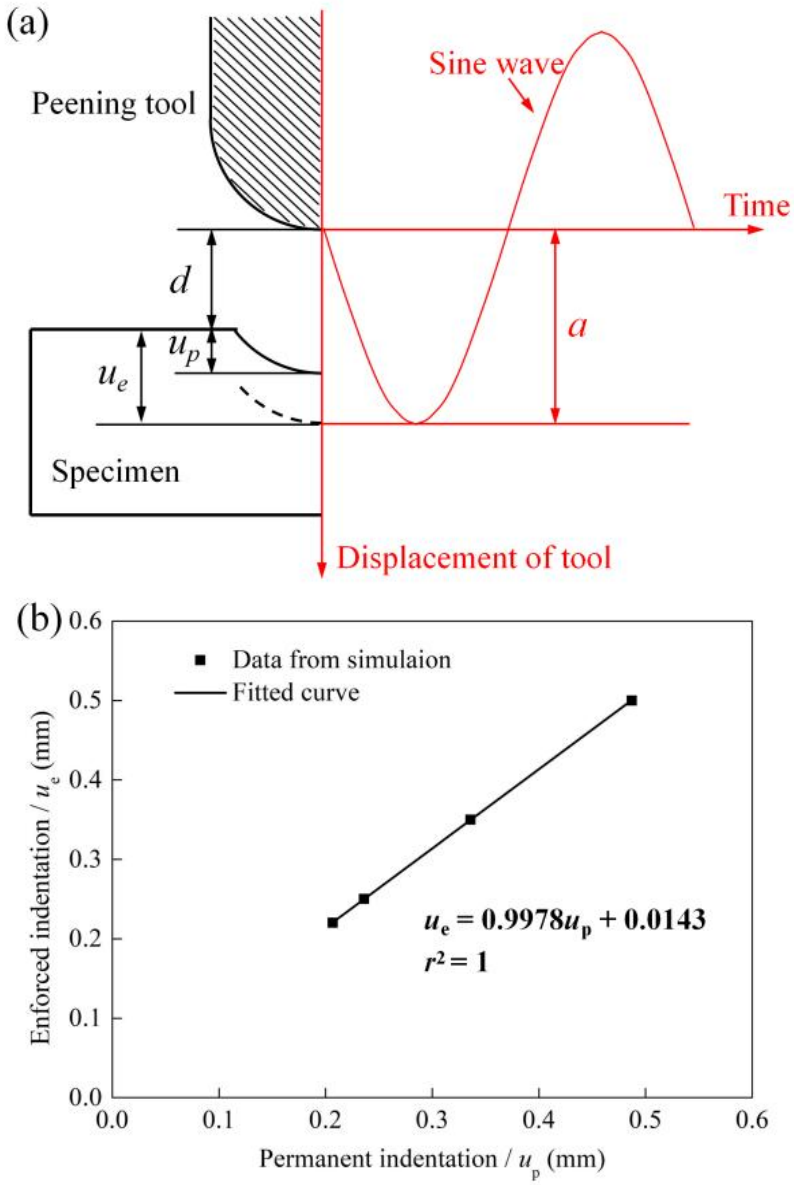

Fig. 2.3 Identification of amplitude of pin displacement a in Z-direction. (a) Schematic diagram of the normal motion (Z-direction) of the tool, (b) Relationship between enforced indentation u_e and permanent indentation u_p.

The choice of material hardening model is an important issue in HFMI analysis as it has a significant impact on the RS distribution. Foehrenbach et. al [42] compared simulated RS field obtained by using isotropic, kinematic and Chaboche hardening models. It revealed that best agreements with RS measurements was achieved by means of Chaboche hardening model, and a simple isotropic model gave an acceptable RS distribution up to 0.8 mm depth. In this work, non-linear isotropic hardening model is chosen, and material data is prepared

from full stress-strain curve, as shown in Fig. 2.4. MSC. Dytran allows the engineering stress-strain data to be used as the standard input data. The elastic modulus E and yield strength σ_0 are updated with incremental steps according to the accumulated plastic strain ε_p. The initial E and σ_0 are set to 210 GPa and 388 MPa respectively. The Poisson's ratio v is set to 0.3. In addition, the effects of strain rate-dependent hardening is ignored in the current study.

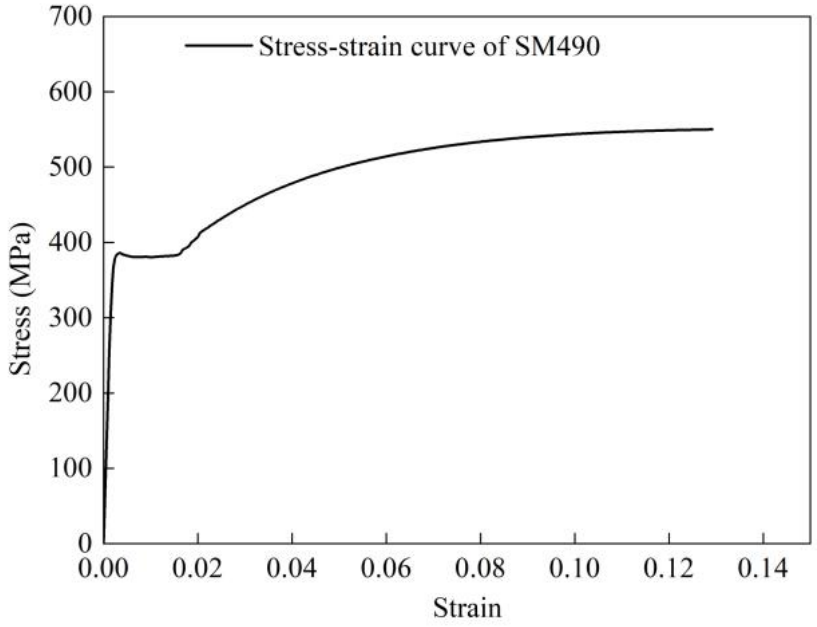

Fig. 2.4 stress-strain curve of SM490 steel.

To reduce the cost of analysis, the load rate scaling method was employed in HFMI simulation. The concept of this method is to artificially increase the impact velocity and frequency, so that the same simulated process is completed in a shorter time step while keeping the similar effect of experiment. The load rate scaling method is used to shorten the simulation time and achieve a good accuracy if model has rate-independent materials. In this work, the up-scaling rate is set to 80, which means that the actual travel speed and hammering frequency used for simulation are 800 mm/s and 6400 Hz respectively, 80 times higher than the experimental parameters.

2.4 Comparison of Numerical Results with Experiment

Fig. 2.5 shows the comparison of simulated and experimental peening groove profile. The peening depth is over 0.2 mm, which fulfills the IIW recommendations [33]. Both peening width and depth obtained by FEM match with the measured data well, which verifies the developed empirical formula and the HFMI simulation system. Fig. 2.6 shows

the comparison of longitudinal RS obtained by simulation and X-ray measurement. As can be seen from Fig. 2.6, compressive stress with a peak over 300 MPa is introduced in the treated zone. The HFMI-induced stresses decrease gradually with the distance from the treated zone center, with values close to 0 in areas u_p to 10 mm away from the weld toe. Overall, the calculated RS shows a good agreement with measured data. Therefore, the HFMI parameters and chosen hardening model in analysis are reasonable.

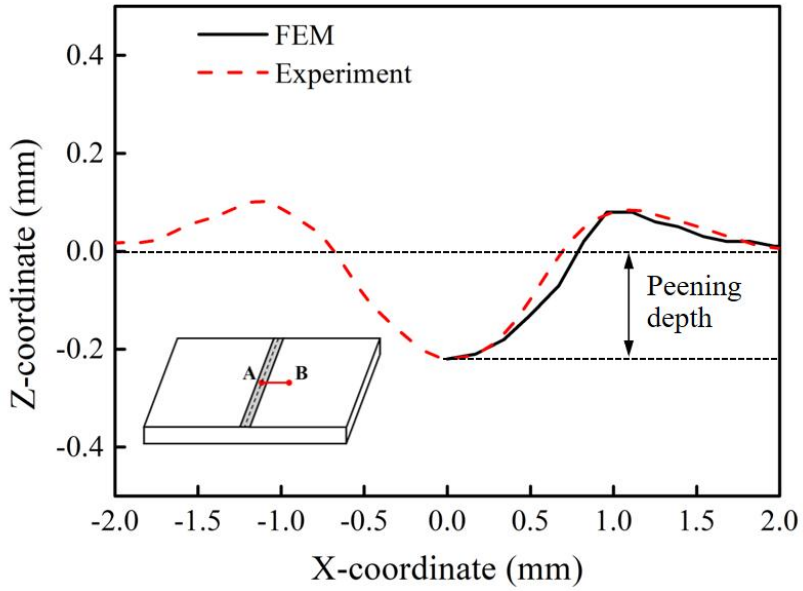

Fig. 2.5 Comparison of peening groove profile obtained by FEM and experiment along Path AB.

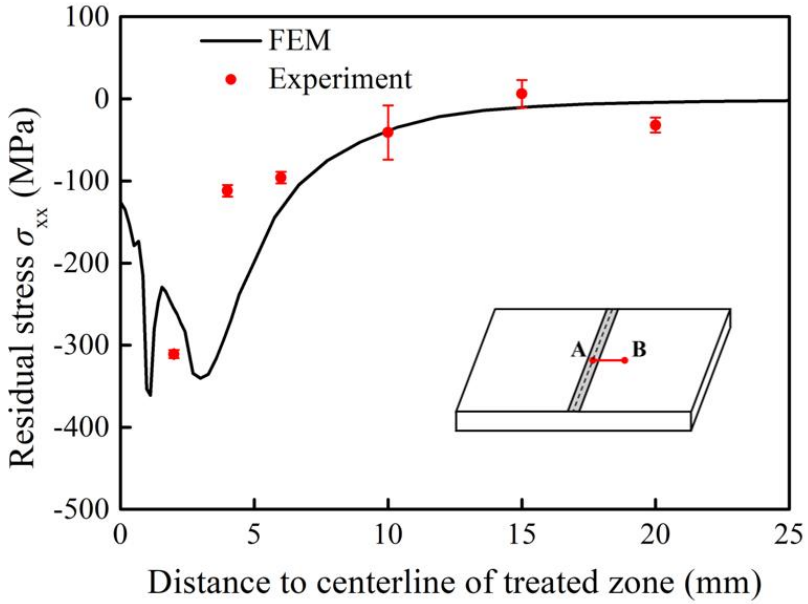

Fig. 2.6 Comparison of simulated RS (σ_{xx}) and X-ray measurement along Path AB.

2.5 Effect of Analysis Condition

Model simplification and parameter optimization are important issues in simulation work. Reasonable simplification can greatly improve the efficiency of analysis while maintaining acceptable accuracy, which helps to extend the applicability of the simulation model, especially to more complex problems in practice. In this section, the effects of FE mesh size, peening length, and peening indentation are investigated numerically. These simulation results help to determine reasonable analysis conditions and give simulation recommendations.

2.5.1 Mesh size

Fig. 2.7 compares residual stress (σ_{xx}) distribution induced by HFMI treatment simulated by FE meshes of different sizes. The mechanical boundary condition, enforced indentation (0.2 mm), material properties, hardening model, and contact setting are the same in all four cases, as mentioned in section 2.3. It can be seen from Fig.2.6 that the distribution of residual stresses in the HFMI groove is highly complex. There is a large stress gradient in the through-thickness direction. Fig. 2.8 digitally presented the distribution of residual stresses along the through-thickness direction. The mesh sizes near the treated zone has a significant influence on residual stresses. To balance analysis efficiency and accuracy, the recommended mesh size is 0.15×0.15×0.15 mm. Herein, the ratio of pin radius to mesh size is 10.

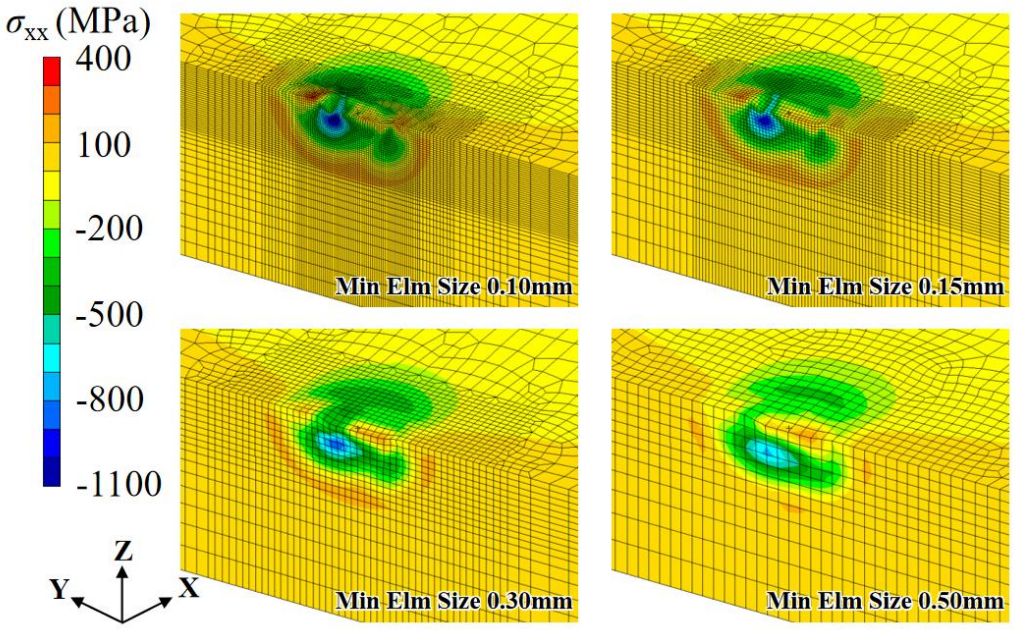

Fig. 2.7 Residual stress (σ_{xx}) contours after HFMI treatment simulated using FE meshes of

different sizes.

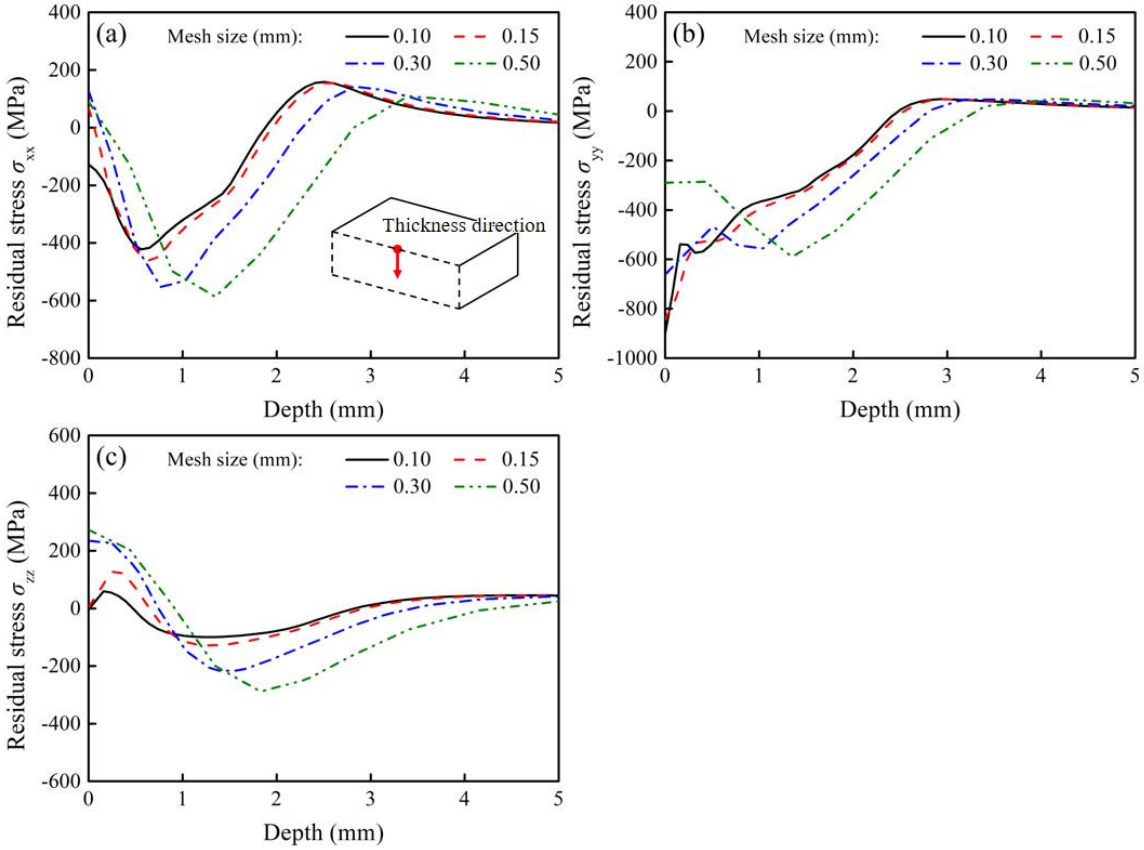

Fig. 2.8 The distribution of HFMI-induced residual stresses along the through-thickness direction simulated using FE meshes of different sizes. (a) σ_{xx} (b) σ_{yy} and (c) σ_{zz} stress components.

2.5.2 Peening length

Fig. 2.9 show the distribution of residual stresses along the through-thickness direction after HFMI treatment with different peening length. It can be seen that the peening length has a slight effect on residual stress when peening length > 4mm. To save the analysis time, HFMI simulation of 6 mm is sufficient to obtain an reasonable stress distribution.

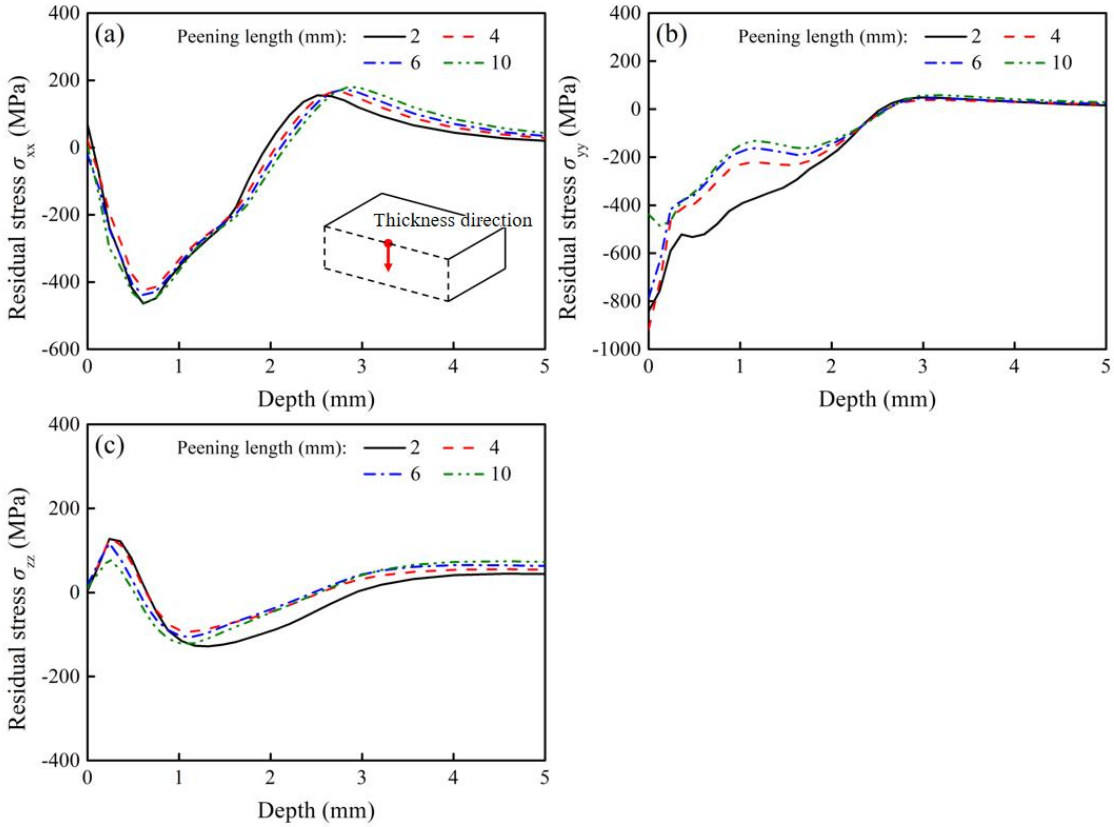

Fig. 2.9 The distribution of residual stresses along the through-thickness direction after HFMI treatment with different peening length. (a) σ_{xx} (b) σ_{yy} and (c) σ_{zz} stress components.

2.5.3 Peening indentation

Fig. 2.10 compares the residual stress distributions after HFMI treatment with different peening indentations. The peak and range of compressive stress in the through-thickness direction increase with peening indentation. For accurate evaluation of residual stress distribution, it is necessary to determine the simulation parameters, such as the amplitude of pin displacement, based on the measured peeing indentation values.

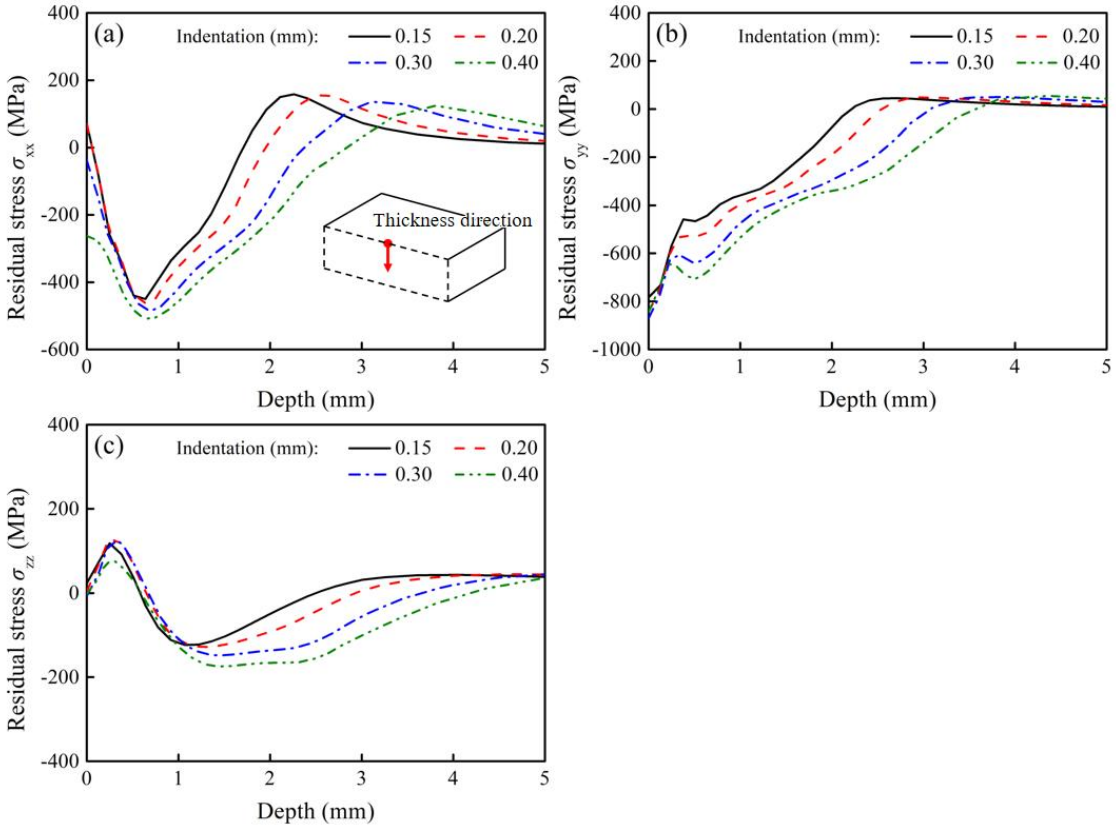

Fig. 2.10 The distribution of residual stresses along the through-thickness direction after HFMI treatment with different peening indentations. (a) σ_{xx} (b) σ_{yy} and (c) σ_{zz} stress components.

2.6 Summary

A dynamic explicit elastic-plastic FE (EP-FE) model is developed based on the commercial FE code MSC. Dytran. The elastic-plastic behavior of materials during the HFMI treatment is considered using a non-linear isotropic hardening model. The validity of the proposed HFMI simulation process is examined by comparing the results of flat plate peening obtained by numerical simulation with the experiment. The effects of FE mesh sizes, peening length, and peening indentation are investigated numerically. Following conclusion could be made:

(1) The residual stress and peening groove profile obtained by flat plate peening simulation match well with the measurements, which shows the validity of the developed analysis method and employed input parameters.

(2) Considerable compressive RS with peak of 686 MPa (σ_{xx}) and 725 MPa (σ_{yy}) is introduced by HFMI treatment in the vicinity of the treated zone.

(3) The mesh sizes near the treated zone has a significant influence on HFMI-induced residual stresses. The ratio of element size in the treated region to the tool's tip radius should be less than 0.1

(4) The peening length has a slight effect on residual stress. To save the analysis time, HFMI simulation of 6 mm is sufficient to obtain an reasonable stress distribution.

CHAPTER 3

Numerical simulation on the HFMI-treated gusset welded joint

3.1 Introduction

To evaluate the fatigue enhancement of welded structures caused by HFMI process, the introduced compressive RS and improved toe profile of the weld need to be investigated. The compressive RS affects the mean stress level under dynamic loading and thus improves the fatigue strength. The notch radius at the weld toe affects the stress concentration as well as the fatigue performance. However, few studies have presented the simulated shape profile at HFMI-treated weld toe and its validation, and they focused mainly on the HFMI-induced RS. In addition, there was no consensus on how to determine the parameters involved in the HFMI simulation, although the analytical framework has been established during the last decade.

The balance between accuracy and efficiency of calculation is an important issue in numerical studies. Ultra-fine mesh is necessary for HFMI simulation to calculate dramatically altered stresses at the treated regions. On the other hand, welding RS needs to be taken into account as an initial condition for HFMI analysis. Previous researchers have used the same ultra-fine mesh in welding analysis as in HFMI simulation, which results in an unnecessary waste of computational resources making it difficult to solve engineering problems, especially for large welded structures.

This chapter aims to propose a practical and efficient numerical simulation procedure for the HFMI treatment of welded joints. The local RS and shape profile were studied by performing thermal-elastic-plastic FE (TEPFE) welding and subsequent dynamic explicit FE (DEFE) HFMI analyses of the out-of-plane gusset welded joints. The zooming technique was employed, and the as-welded stress calculated by using a coarse FE mesh was transferred to the ultra-fine mesh as the initial loading of HFMI analysis. In HFMI analysis, an optimized DCS method was developed. The peening tool's FE mesh was modified so that the wide groove profile caused by the lateral movement of the tool can be simulated. The validation was carried out by comparing calculated HFMI groove profiles and the RS distributions with those measured by the 3-D Scanner and X-ray equipment. The details of simulation procedures are presented in current work and it will contribute to

clarifying how to conduct a practical HFMI simulation on welded joints (even with large sizes), determine necessary simulation parameters, and simplify analysis conditions.

3.2 Experimental work

3.2.1 Fabrication of the welded joint

The gusset welded joint with a longitudinal stiffener was manufactured using the gas metal arc welding method (see Fig. 3.1 for the geometric configurations). The welding parameters are listed in Table 3.1. The base metal was SM490 steel while the filler metal was MG50. The longitudinal stiffener and main plate were joined by the two-pass welding process. The start and end points of welds were located in the middle of the stiffener.

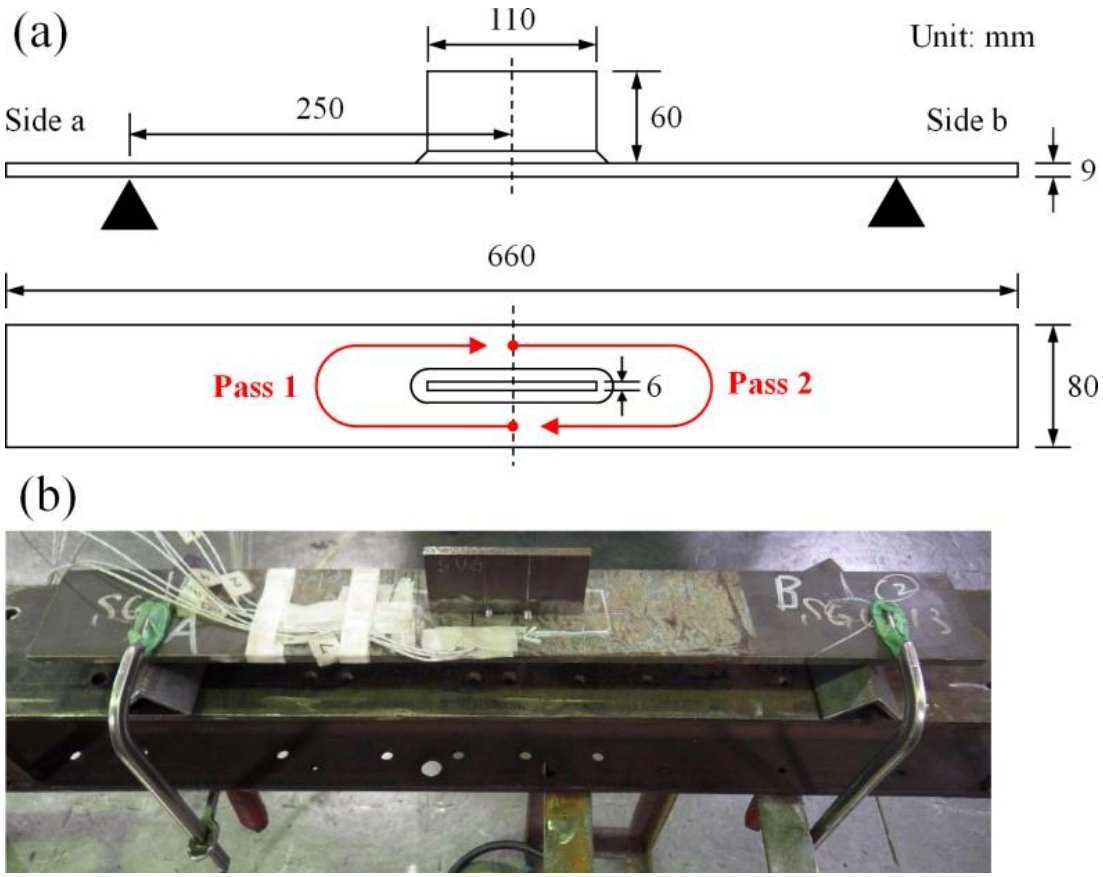

Fig. 3.1 (a) Specimen geometry and welding sequence, and (b) overall photo of specimen and welding clamps.

Table 3.1 Welding parameters.

Pass	Current	Voltage	Speed	Inter-pass

	(A)	(V)	(mm/s)	temperature (°C)
1	210	20	3	100
2	210	20	3	-

3.2.2 HFMI treatment

Subsequently to the welding process, the HFMI treatment was carried out along the welded toe with a travel speed of 5 mm/s and a hammering frequency of 80 Hz. A portable pneumatic needle peening devices (Model: NP1000F20) was used for treatment with an air pressure of 0.5 MPa. A peening tool with a tip radius of 1.5 mm was applied. Fig. 3.2 shows the appearance of the weld toe before and after the treatment.

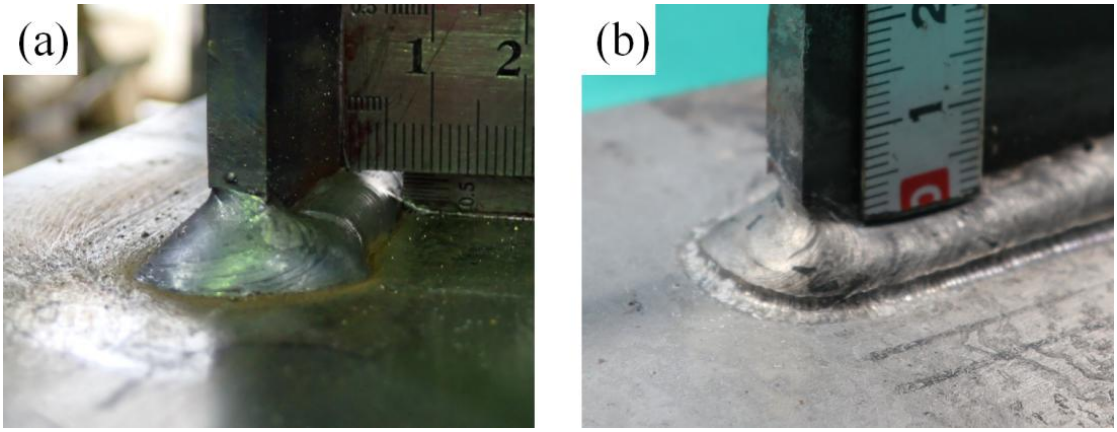

Fig. 3.2 Appearance of weld toe. (a) As-welded toe, and (b) HFMI-treated toe.

3.2.3 Measurements of thermal cycles, RS, and local shape profile

Measurements of thermal cycle, RS, and local deformed shape profile were performed. The locations of the measurements are shown in Fig. 3.3. Five thermo-couples (TC1-5) were used to record welding thermal cycles at the side of the main plate during the welding process (Fig. 3.3(a)). The as-welded and HFMI-induced RS at side b were measured by X-ray diffraction testing. The X-ray stress measurement conditions are listed in Table 3.2. The 3-D laser-scanner equipment was used to measure the local shape profile of the weld toe before and after HFMI treatment (Fig. 3.3(b)). The measured points of the welding thermal cycle and RS measurements are listed in Table 3.3.

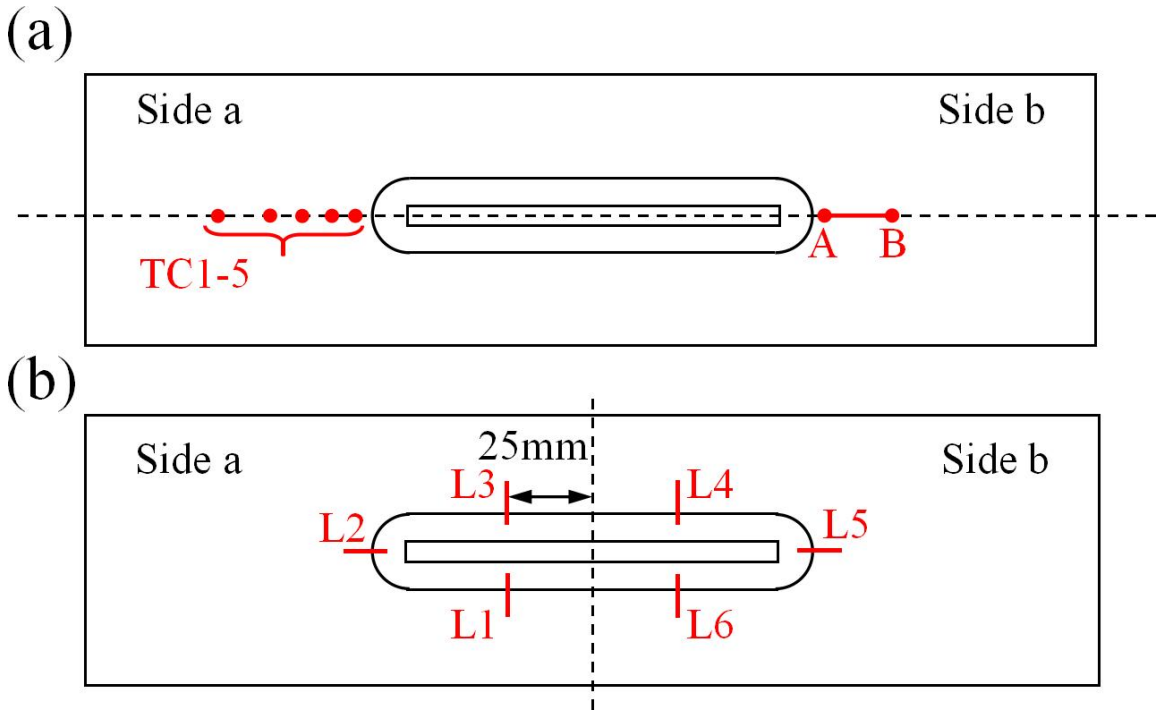

Fig. 3.3 Measurement point arrangement. (a) Thermal cycles, RS, and (b) local shape profiles.

Table 3.2 Parameters for X-ray diffraction stress measurement.

Category	
Mesurement method	Cos α
Characteristic X-ray	Cr-Kα
Diffraction plane	211
Diffraction angle (deg.)	156.4
Tube voltage (kV)	20
Tube current (mA)	1
X-ray incident angle (deg.)	45
Diameter of irradiated area (mm)	2

Table 3.3 Location of measured points.

Welding thermal cycle		As-weld RS		HFMI-induced RS	
TC number	Distance to the stiffener (mm)	Measured point number (along AB)	Distance to the weld toe (mm)	Measured point number (along AB)	Distance to the weld toe (mm)
1	10	1	2	1	2
2	15	2	3	2	3
3	20	3	7	3	5
4	30	4	12	4	7
5	50	5	22	5	9
				6	12
				7	22

3.3 FE analysis

A three-step numerical analysis system, including welding simulation, zooming technique, and HFMI simulation, was developed to predict the HFMI-induced compressive RS and the local shape profile. This system allows the consideration of welding RS as an initial load in the HFMI simulation. The flowchart of the proposed analysis system is shown in Fig. 3.4. Welding simulation is firstly carried out by using JWRIAN in-house code. JWRIAN is a TEPFE code with the ultra-high-speed of implicit analysis, which was developed by The Joining and Welding Research Institute (JWRI) of Osaka University [62-64]. For HFMI simulation, ultra-fine FE meshes are required. The ratio of element size in the treated region to the tool's tip radius should be less than 0.1 [65], e.g., a tool with a 1.5 mm radius tip and the element size less than 0.15×0.15×0.15 mm. However, applying such ultra-fine mesh in welding analysis results in unnecessary waste of computing resources, especially for welded structures with large dimensions. To balance computational efficiency and accuracy, the zooming technique was applied. A stress interpolation code was developed to transfer the as-welded RS from coarse to fine FE mesh used in the HFMI analysis. Using the commercial code MSC. Dytran, the DCS HFMI analysis is then

performed considering the initial load of interpolated welding RS.

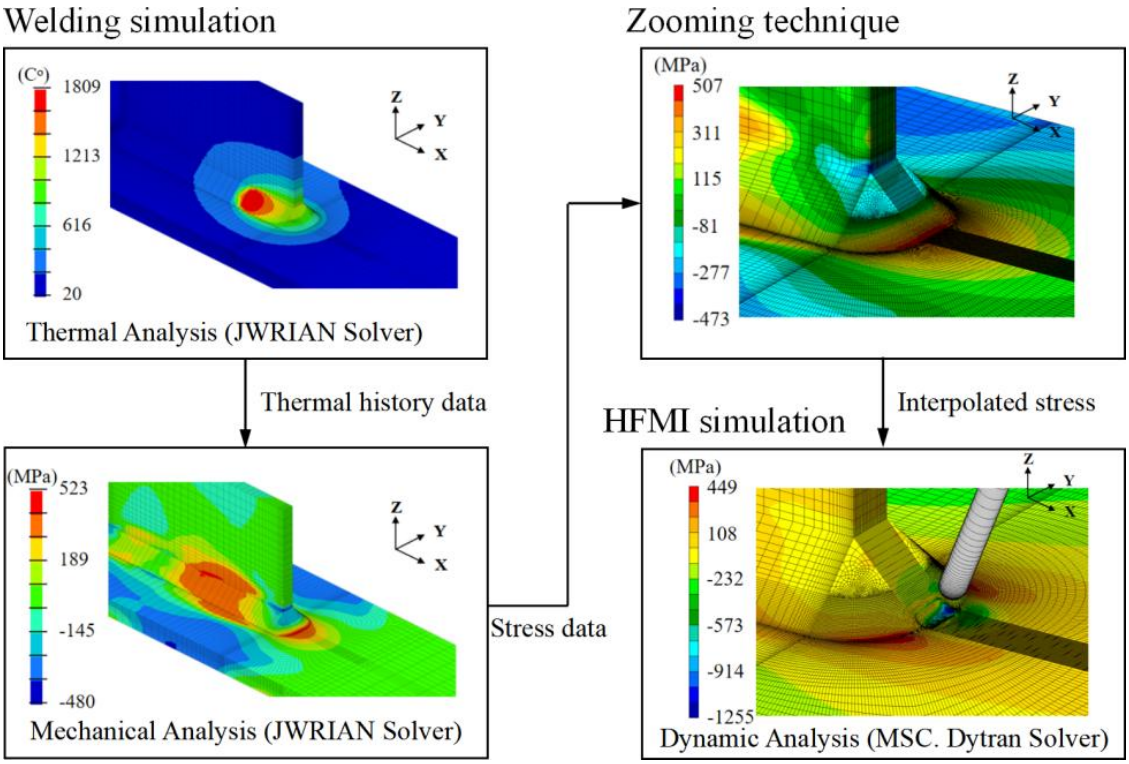

Fig. 3.4 Flowchart of the FE analysis procedure for HFMI treatment of welded joints.

3.3.1 FE modeling of the welding process

Based on the JWRIAN code, the 3-D FE analysis was performed to simulate the welding temperature field and RS. The measured geometry parameters of the as-welded fillet weld are presented in Table 3.4 and Fig. 3.5. In mesh modeling, the toe radius, flank angle, and weld leg were assumed to be 0.8 mm, 45°, and 8 mm, respectively. Other dimensions of FE mesh were the same as that of experimental mock-ups. There were 177,092 8-node brick elements and 193,639 nodes in the FE mesh, see Fig. 3.6. The finest elements with a size of 0.5×0.5×0.5 mm were designed at the rounded seam.

Table 3.4 Measured geometry parameters of the as-welded fillet weld.

Location	Toe radius (mm)	Flank angle (degree)	Weld leg 1 (mm)	Weld leg 2 (mm)
L1	0.8	35.5	7.0	8.6
L2	1.2	39.9	6.6	8.3

L3	0.9	40.3	8.4	8.0
L4	0.5	12.3	8.2	8.3
L5	0.6	47.7	7.2	8.6
L6	1.4	42.0	8.3	8.9

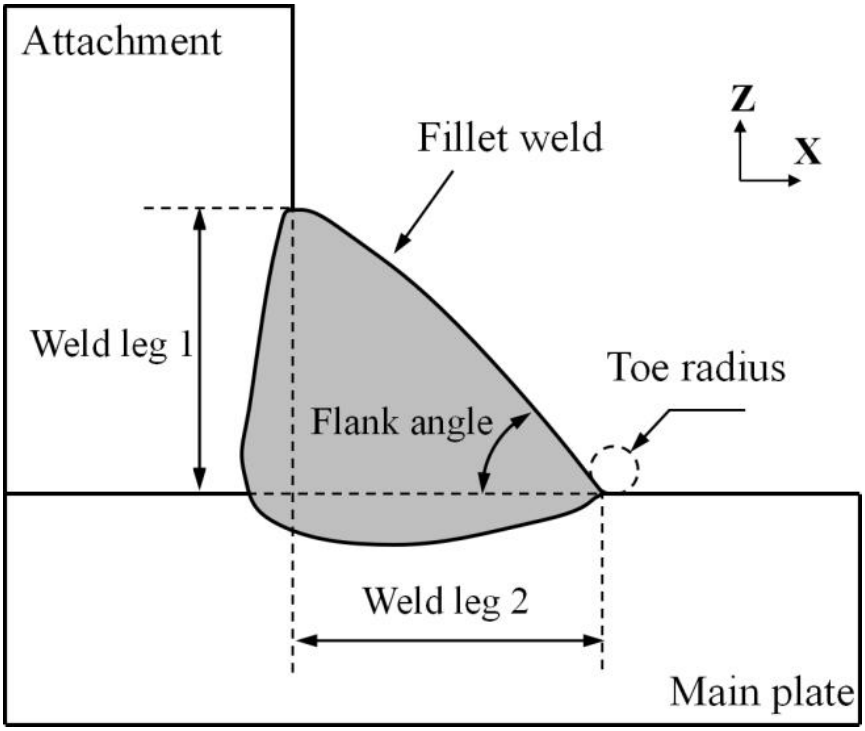

Fig. 3.5 Fillet weld profiles and their geometry.

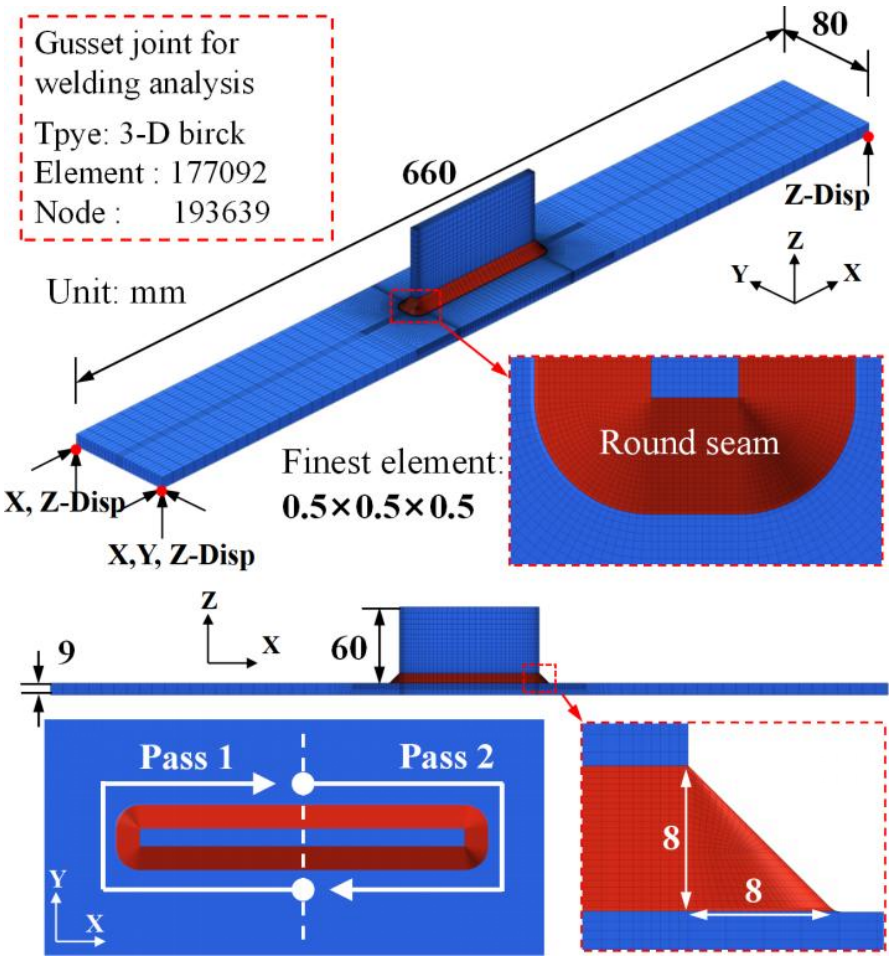

Fig. 3.6 Coarse FE mesh of the gusset joint used in welding analysis.

The thermal analysis was performed first to obtain the temperature history data. A half-ellipsoid moving heat source [66] with uniform density was employed. The area of action can be described as Eq. (10). The heat flux, q_h, is calculated by Eq. (11).

$$\frac{(x-vt)^2}{a^2}+\frac{y^2}{b^2}+\frac{z^2}{c^2}\le 1, \quad (z\le 0) \tag{10}$$

where x, y, and z are the coordinates (mm) in the reference system, t is the time, v is the welding speed, a, b, and c are the shape parameters of half-ellipsoid.

$$q_h=\frac{3Q\eta}{2\pi abc} \tag{11}$$

where Q is the power of heat source and η is the thermal efficiency, depending on the welding method.

The welding analysis parameters are listed in Table 3.5. The trial and error method was used to identify the shape parameters of the heat source. Heat losses from specimen to

environment were also considered by setting a temperature-dependent convection coefficient on the outer surface of the FE mesh. The inter-pass and ambient temperature in welding analysis were set to 100 °C and 20 °C, respectively.

Table 3.5 Parameters for welding analysis.

Pass	Q (W)	η	V (mm/s)	a (mm)	b (mm)	c (mm)
1	4200	0.8	3	7	5.5	5.5
2	4200	0.8	3	7	5.5	5.5

In TEPFE analysis, the temperature history data was employed as the thermal load to calculate stress, strain, and displacement. Only minimal constraints were applied in simulation to prevent the rigid body movement given the relatively weak external constraints in the experiment, see Fig. 3.6. The temperature-dependent material properties of SM490 (base metal) used in welding analysis were referenced in ASME sec II Part D [67] see Fig. 3.7. For filler metal MG50, its temperature-dependent yield strength was presumed according to its value at ambient temperature (445 MPa) and the properties of the base metal at high temperature. Other material properties of MG50 were assumed to be consistent with the base material. Sun et al. [68] investigated the effects of solid-state phase transformation (SSPT) and strain hardening on welding RS in weldments made by low-alloy structure S355 steel (f_y = 423MPa). The mixed strain hardening model combined with solid-state phase transformation can predict welding RS more accurately while using the ideal elastic-plastic model resulted in a 100 MPa discrepancy of longitudinal stress near the weld seam. Nonetheless, the phase transformation and strain hardening were ignored in the present welding analysis model to reduce tedious modeling.

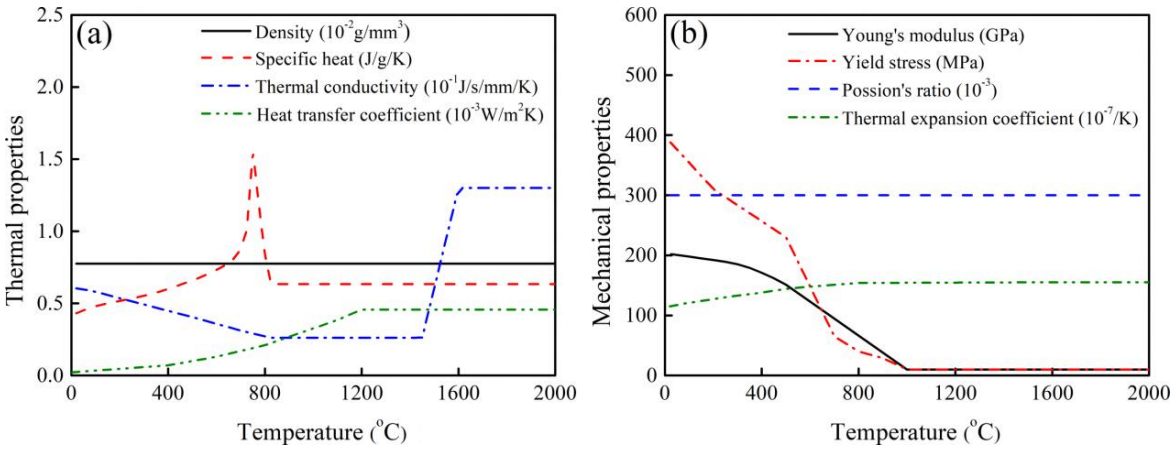

Fig. 3.7 Material properties of SM490. (a) Thermal properties, and (b) mechanical properties.

3.3.2 FE modeling of the HFMI treatment

3.3.2.1 FE mesh design and analysis condition

A 3-D FE mesh using the 8-node brick elements was built with the same geometry as that used in welding analysis, but the element sizes were smaller, see Fig. 3.8. The finest elements were designed near the round seam with element sizes of 0.15×0.15×0.15 mm. For the rest of the FE mesh, the elements' sizes increase with the distance to the treated zone to balance analysis efficiency and accuracy. Only half of the gusset joint was modeled to save the analysis time. The peening tool was modeled as the rigid surface using 4-node 2-D shell elements to reduce computational effort [69]. The radius of the tool's tip in the mesh model was artificially increased to 2.05mm while its value was 1.5 mm in the experiment. The trial and error method was used to determine the radius in the tool's FE mesh, which is presented in Section 3.3.2.

The initial location of the peening tool was identified by the profile of the HFMI-treated groove, as shown in Fig. 3.9. Point Q is the center of curvature of the peening groove, and the radius of the peening groove, ρ_h, can be determined from the measured data. Assuming that the origin of the coordinate system was at the upper surface of the main plate, the tip of the peening tool P (x_P, z_P) can be obtained by Eq. (12):

$$\begin{cases} z_P = d \\ x_P = x_Q - \cot\theta(\rho_h - u_p - d) \end{cases} \tag{12}$$

where d is the distance between the tool's tip and the main plate, which is assumed to be 1.0 mm; θ is the peening angle, which is assumed to be 67.5°; x_Q is the X-coordinate of point Q, which is determined by the origin of the coordinate system; ρ_h is the radius of the peening groove; and u_p is the permanent indentation caused by HFMI treatment.

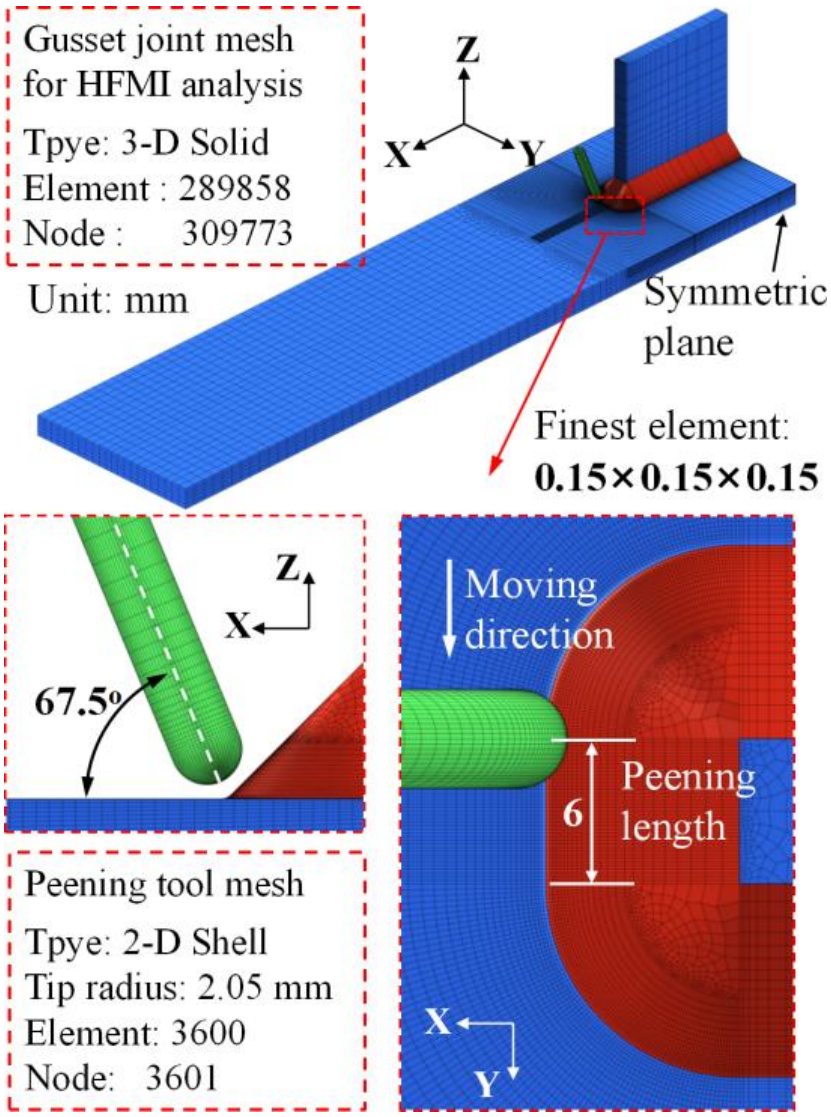

Fig. 3.8 Fine FE mesh of the gusset joint and peening tool in HFMI analysis.

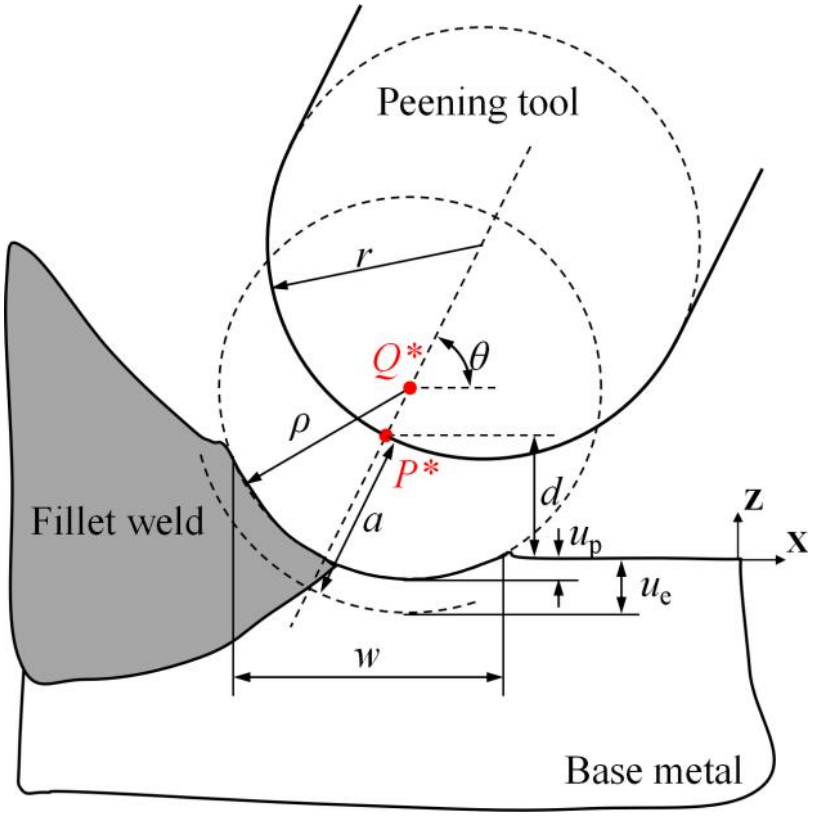

Fig. 3.9 Geometry of the HFMI-treated groove shape.

In HFMI simulation, all nodes on the bottom surface were fixed in X, Y, and Z-direction while the nodes on the symmetric plane were fixed in X-direction. The rotation of the peening tool was restricted and only linear motion in Y-direction and sine motion in the axial direction were allowed. A contact pair was defined between the tool's tip (master surface) and the specimen (slave surface), using the penalty function method. The friction coefficient was set to 0.3. To save analysis time, the peening length was set to 6 mm in the current work.

Material hardening models play an important role in HFMI simulation. The effects of the chosen hardening models, including isotropic, kinematic, combined isotropic-kinematic, and strain rate-dependent models, have been examined by Foehrenbach et al. [42] and Khurshid et al. [43]. The kinematic hardening behavior was described by Chaboche model [70]. While excellent agreements with the experiments have been observed with the combined isotropic-kinematic and stain rate-dependent model, a good predicted RS can be obtained by using DCS considering the simplified isotropic hardening model. Therefore, a non-linear isotropic hardening model was chosen in this work, and material data was obtained from tensile tests, as shown in Fig. 3.10. MSC. Dytran allows the engineering stress-strain data to be used as the standard input data. In addition, the effect of strain rate-

dependent hardening was ignored.

The load rate scaling method was used to reduce analysis time [71]. The concept of this method is to artificially increase the impact velocity and frequency so that the same simulated process is completed in a shorter time step while keeping the similar effect of the experiment. The load rate scaling method is used to shorten the simulation time and achieve good accuracy if the model has rate-independent materials. To choose a suitable scaling rate, four HFMI simulation cases (without initial stress) with different up-scaling rates were performed. Fig. 3.11 shows the RS from DCS simulations for four different up-scaling rates. It can seem that up-scaling rates have a negligible effect (less than 5%) on RS if its values were less than 80. Therefore, the up-scaling rate was set to 80 in formal cases, which means that the travel speed and hammering frequency in the simulation were 80 times faster than that of the experiments.

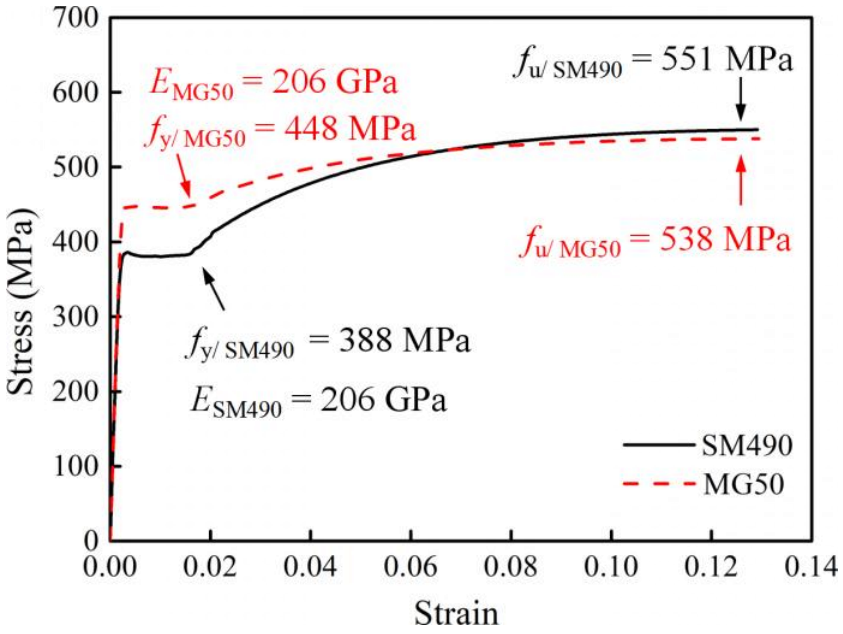

Fig. 3.10 Stress-Strain curves of SM490 and MG50 (presumed).

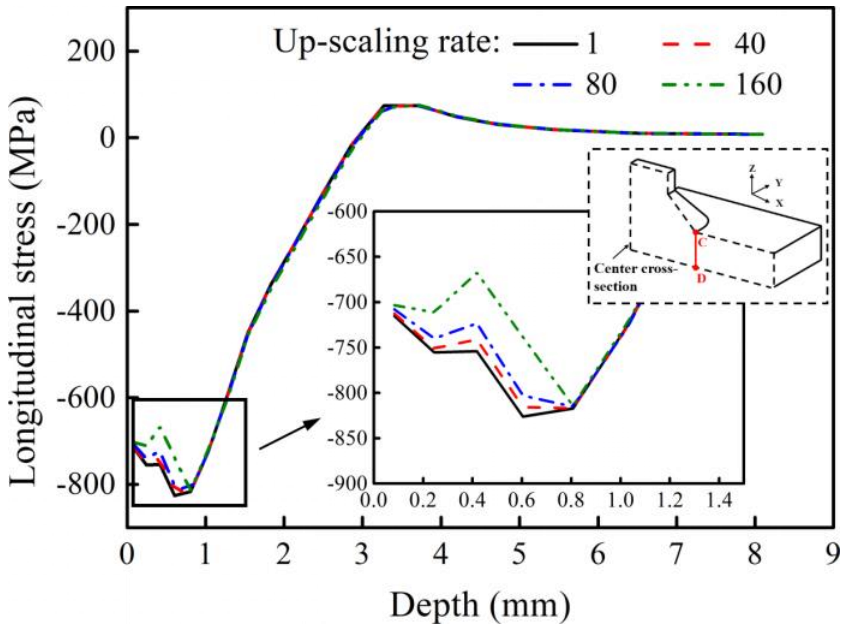

Fig. 3.11 Simulated RS using different up-scaling rates.

3.3.2.2 Identification of parameters for displacement controlled HFMI simulations

For the DCS method, the displacement of the peening tool was set following the given path. The axial cyclic movement of the tool was simplified as a sinusoidal motion in simulations. The *x* and *z* components of the tool's motion are given by Eq. (13):

$$\begin{cases} X_x = a\cos\theta\sin(2\pi ft) \\ X_z = a\sin\theta\sin(2\pi ft) \end{cases} \tag{13}$$

where a is the amplitude; θ is the peening angle; f is the peening frequency; and t is the time.

The amplitude a (see Fig. 3.9) relates to the peening depth, which can be calculated by Eq. (14):

$$a = \frac{1}{\sin\theta}[d + u_e - r(1-\sin\theta)] \tag{14}$$

where u_e is the enforced indentation; and r is the radius of the tool's tip.

It is difficult to directly measure u_e due to the elasticity of the material. One solution is to investigate the relationship between enforced indentation u_e and permanent indentation u_p where u_p is easily obtained from measurements. For this purpose, four HFMI analysis cases with assumed u_e of 0.15, 0.20, 0.25, and 0.30 mm were performed to obtain simulated u_p. The fitted curve is given by Eq. (15). The measure u_p is 0.132mm so that u_e of 0.148 mm was applied in the simulation.

$$u_e = 1.002\,u_p + 0.016 \qquad (R^2 = 1.000) \tag{15}$$

In DCS, the peening tool mesh was modeled as a rigid surface and its movement was also simplified as mentioned. However, the tool's aberration and lateral movement may increase the radius of the peening groove ρ_h and the peening width w. To consider its effects, the radius of the pin's FE mesh, r, was artificially increased. Four cases with assumed r of 1.5, 2.0, 2.5, and 3.0 mm were performed to obtain simulated w. Then the relationship between r and w was determined, see in Eq. (16). Thus, the optimized r of 2.05 mm can be obtained based on the measured peening width of 2.68 mm.

$$r = 0.991\,w - 0.611 \qquad (R^2 = 0.993) \tag{16}$$

3.3.2.3 Zooming technique

Leitner et al. [45] used the same FE mesh for both welding and HFMI simulations. The as-welded stress obtained by welding analysis was directly applied in subsequent HFMI simulations. However, they used coarse FE mesh in HFMI simulation and it may affect the accuracy of simulated results. On the other hand, if the ultra-fine mesh is used for both welding and HFMI simulation, it will lead to unnecessary waste of computing resources. In this work, the zooming technique was applied in the proposed HFMI analysis system to balance the accuracy and efficiency. The welding RS was simulated using a coarse FE mesh, and then the interpolated stresses (normal stresses σ_x, σ_y, σ_z and shearing stresses τ_{xy}, τ_{yx}, τ_{xz}) were calculated using the Griddata function of Numpy [72]. These interpolated stresses were included in Dytran's input file and used as the initial stresses for HFMI simulation. Table 3.6 compares the computational time of welding process using a fine FE mesh and a coarse one. Only half of the gusset joint was modeled (Y-Z plane as symmetric plane). The zooming technique allows the usage of a coarse FE mesh in welding analysis and thus saves up to 80% of analysis time.

It should be noted that the interpolated stresses are not directly calculated by the laws of mechanics, which means the initial stress in HFMI simulation may not be in equilibrium. This phenomenon was observed in the study by Schubnell et al. [73]. To remove this noise in the interpolated stress values, 10% of the critical damping was applied, and a short time of 0.002 sec was added letting initial stress settle down. Fig. 3.12 shows the comparison among as-welded RS from welding analysis, interpolated welding RS, and stable initial stress in HFMI analysis. The as-welded RS was in good agreement with interpolated RS,

which verifies the accuracy of the developed interpolation code. The maximum variation of about 100 MPa between interpolated RS and balanced one occurred in the vicinity of the weld toe. The main reasons for this difference are that the interpolated RS in fine mesh re-establish the balance due to the notch effect and different element types used for welding and HFMI simulation. However, the initial welding RS close to the weld toe has a negligible effect on subsequent simulation, as those stresses will be replaced by the large compressive stresses introduced by HFMI. Overall, the initial stress obtained by the developed interpolation code was reliable.

Table 3.6 The computational time of welding process using fine and coarse FE mesh.

FE mesh	Element number	Node Number	Computational time (h)
Fine	309,773	289,858	47.0
Coarse	88,546	97,776	8.7

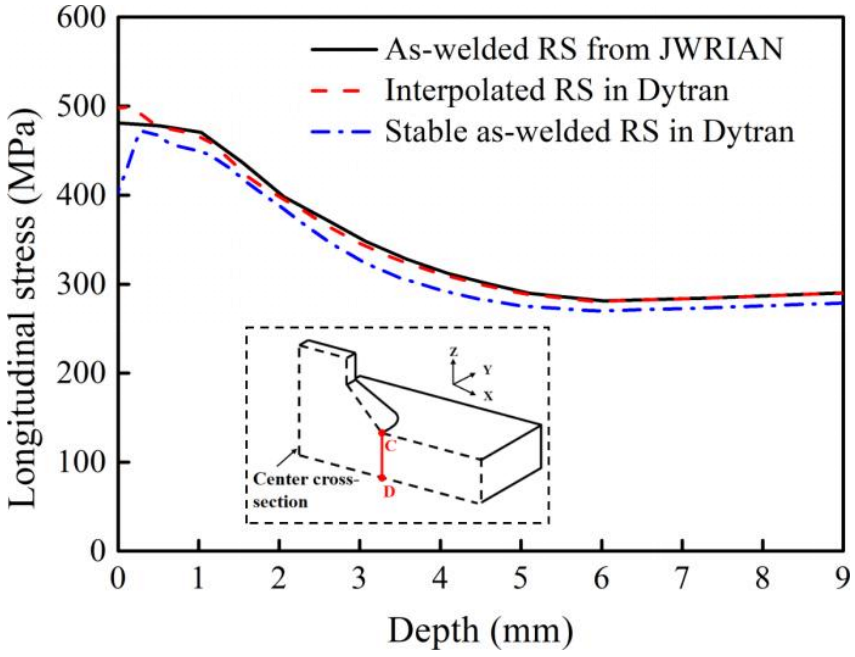

Fig. 3.12 Through-thickness longitudinal RS distribution.

3.4 Results

3.4.1 Welding analysis results

For the validation of the welding simulation, the measurements of the thermal cycles

and as-welded stress were carried out. The predicted results of the thermal analysis were compared with the measured welding thermal cycles, as shown in Fig. 3.13. The predicted peak temperature and cooling rate of the welding thermal cycle matched well with the measurements. Fig. 3.14 compares the welding RS predicted by FEM and the measurements. For the areas 5 mm away from the weld toe, simulated RS was about 100 MPa larger than the measured one. The reason is the initial compressive RS on the surface of plates before welding, which was not taken into account in the simulation. On the contrary, the simulated results were in good agreement with the measured RS for regions close to the weld bead, as the material was heated to a high temperature and the initial stress was released.

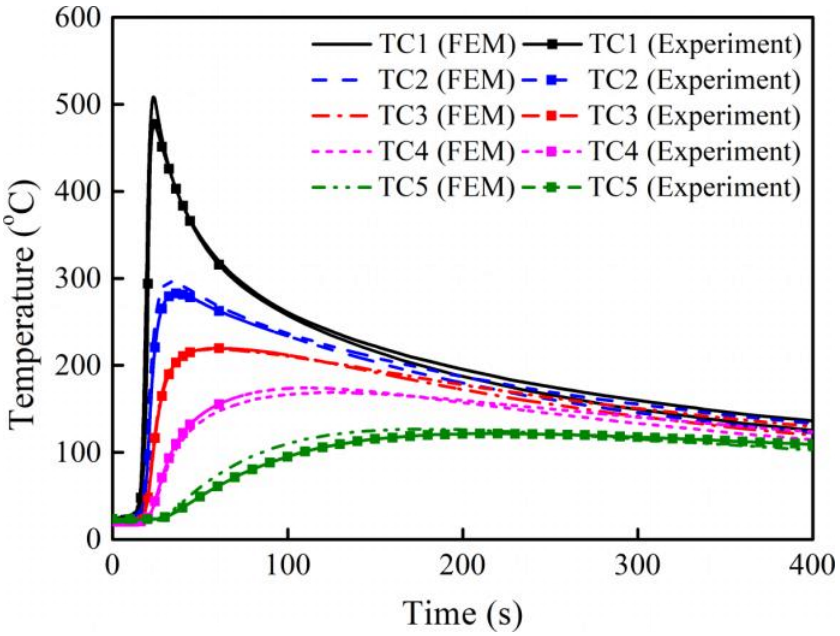

Fig. 3.13 Comparison of the predicted and measured thermal cycles of first welding pass for side a of the specimen.

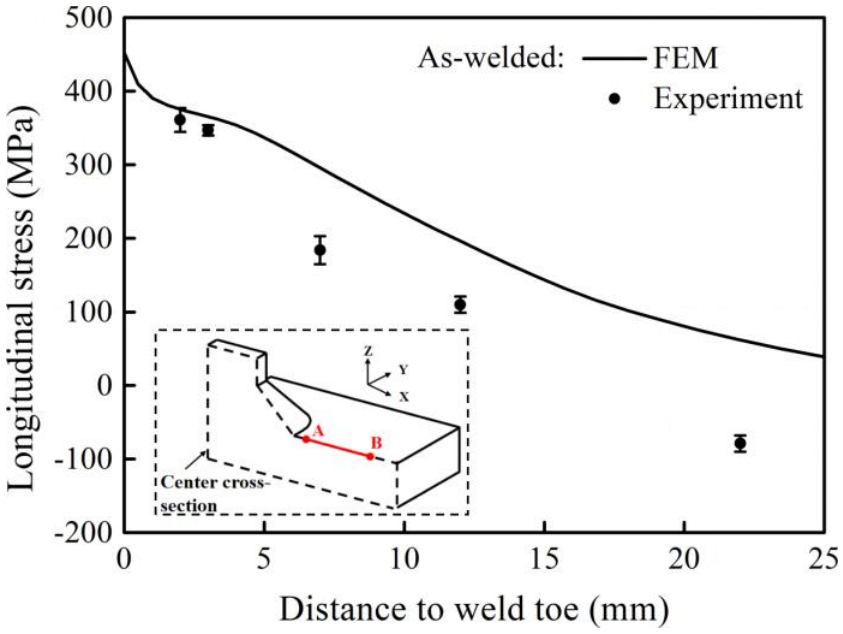

Fig. 3.14 Comparison of the predicted and measured welding RS on the upper surface for side b of the specimen.

3.4.2 Shape profile and RS distribution induced by HFMI treatment

The local shape profiles for the HFMI-treated zone were measured by the 3-D laser scanner. The analysis parameters used to control the tool's motion were obtained by the identification method presented in Section 3.2.2. The radius of the tool's FE mesh r was modified to account for the effects of lateral movement of the pin. Fig. 3.15 shows the local shape profiles calculated by FEM with r of 1.50 and 2.05 mm as well as the measured results. The r of 1.50 mm was the true radius of the peening tool in the experiment while the 2.05 mm was the optimized one. The predicted result with r = 2.05 mm matched best the measured shape profile.

Fig. 3.16 compares the HFMI-induced RS predicted by FEM with measured results. The simulated RS was in good agreement with measured data for regions close to the weld toe. However, the stress discrepancy of about 100 MPa occurred in the areas 7 mm away, which is similar to the situation with welding stresses. Such a difference is acceptable because the stress away from the weld toe will not affect the fatigue strength of structures, and the stress near the weld toe is the focus of this work. Considerable compressive RS was introduced by the HFMI treatment in the vicinity of the treated zone compared with the as-welded condition, see Figs. 3.17 and 3.18. For as-welded conditions, the material at the weld toe was in a multi-axial stress state, with longitudinal stresses reaching 508 MPa and transversal stresses of 300 MPa. After HFMI, the tensile stresses in the vicinity of the weld toe were

converted to high compressive stresses, where the stresses in the peening groove were approximately -400 to -700 MPa for the longitudinal component and -700 to -1000 MPa for the transversal component. The introduced compressive RS can be superimposed on the stresses due to external loads, reducing the local stress ratio and thus improving the fatigue life of the structure [52].

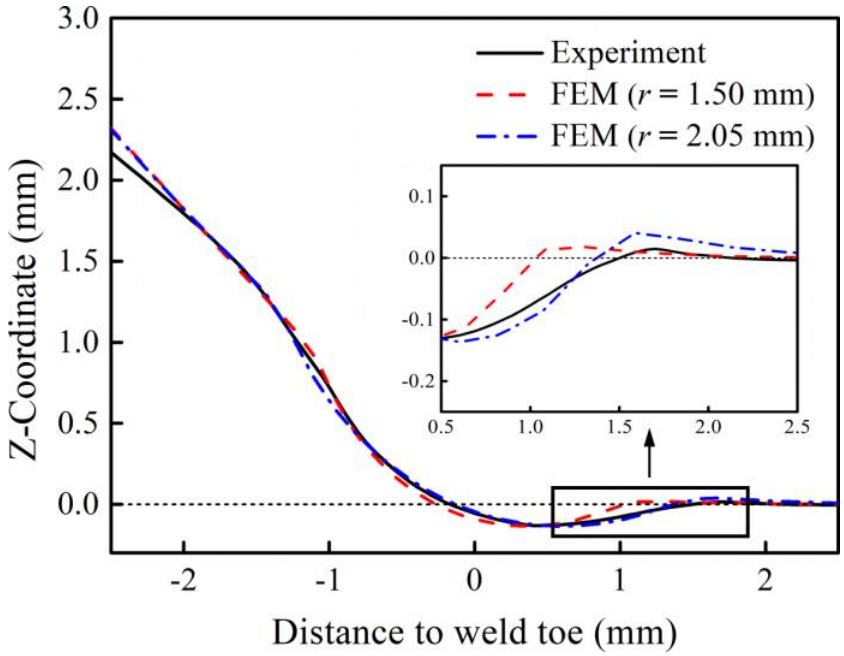

Fig. 3.15 Comparison of the predicted and measured local shape profiles for side b of the specimen.

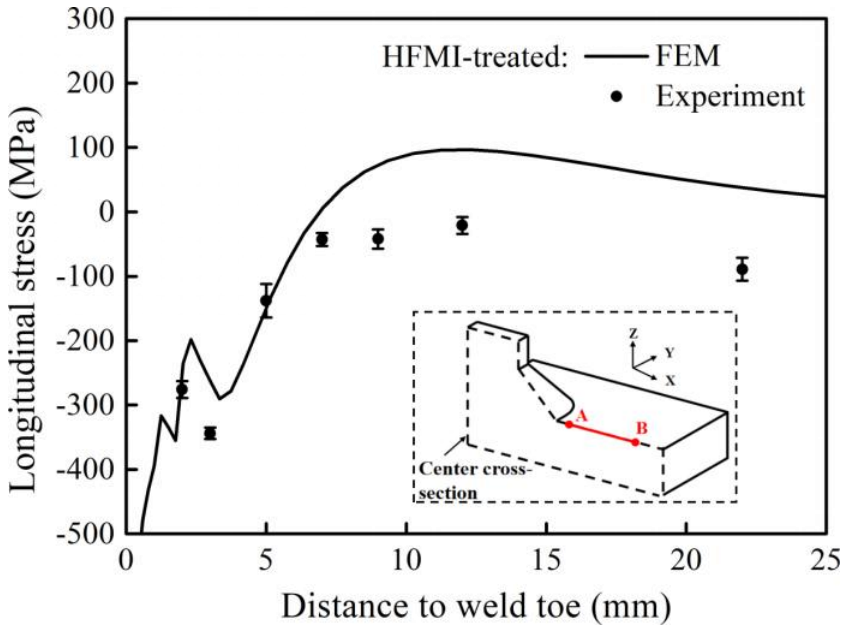

Fig. 3.16 Comparison of the predicted and measured stress distribution after HFMI treatment for side b of the specimen.

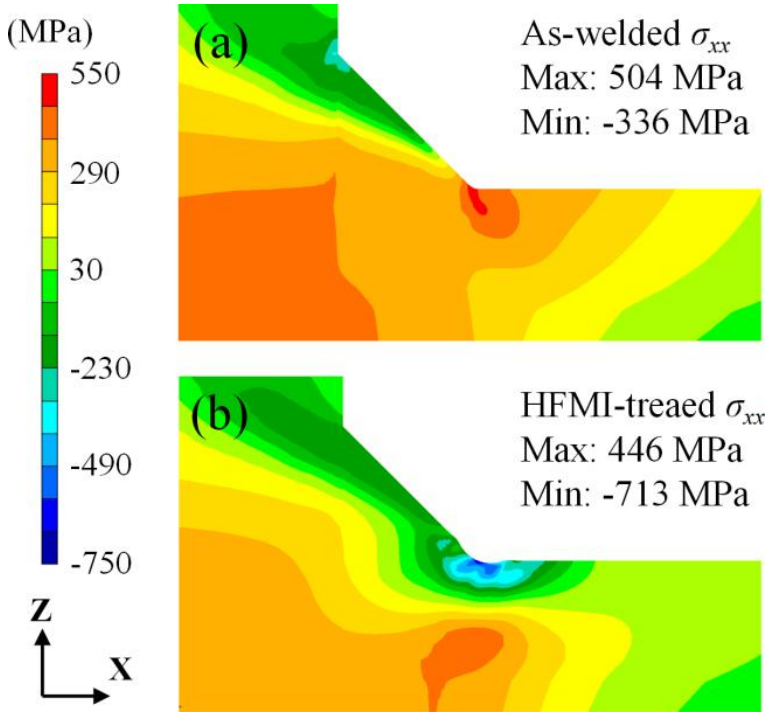

Fig. 3.17 Longitudinal stress (σ_{xx}) distribution on center cross-section. (a) As-welded, and (b) HFMI-treated joint.

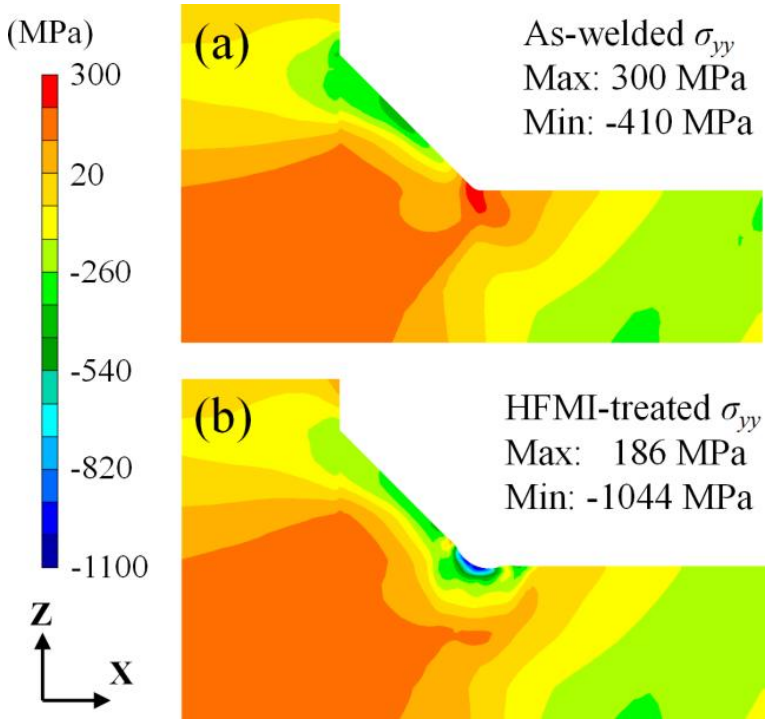

Fig. 3.18 Transversal stress (σ_{yy}) distribution on center cross-section. (a) As-welded, and (b) HFMI-treated joint.

3.5 Discussion

3.5.1 Material hardening model

A reasonable material model and HFMI analysis conditions are essential for the accurate prediction of local RS and deformed shape profiles induced by HFMI treatment. In the current work, the effect of SSPT and strain hardening were ignored for welding analysis while only an isotropic hardening model was considered in HFMI analysis. The results in Fig. 3.14 and 3.16 show a good agreement between the predicted RS distribution with this simplified material model and the measured results for welded joints made with SM490 steel. However, for high-strength steels, SSPT will strongly influence as-welded stress according to studies by Sun et al. [74], and its effect on HFMI-induced RS needs further study.

The introduced compressive RS is not stable due to the stress relaxation under the cyclic loading [75]. The stress relaxation analysis followed by the HFMI simulation is necessary for assessing fatigue life. In such analysis, the Bauschinger effect of the material cannot be neglected when the structure is subjected to cyclic loading, especially with variable amplitude. The applicability of the isotropic hardening model needs further investigation in the sequential simulation of HFMI and RS relaxation.

3.5.2 Boundary condition in FE analyses

A strong mechanical boundary condition was considered in the HFMI analysis, i.e. all nodes on the back face of the base plate were constrained in X, Y, and Z-direction. Such boundary conditions are not suitable for subsequent stress relaxation simulation under cyclic loading, although they are appropriate in HFMI analysis. If changing boundary conditions in cyclic load analysis, unwanted stress relaxation may occur due to the sensitivity of the stresses at the notch, when HFMI-induced RS is used as the initial load. Therefore, the effect of boundary conditions on RS still needs to be clarified.

In addition, a more accurate reproduction of the treated local profile is possible by modifying the tip radius of the pin mesh, which is beneficial for assessing the local stress concentration and RS relaxation under cyclic loading in subsequent studies.

It is known that the RS contained in welded joints superimposes with fatigue loads, thus affecting fatigue life. However, existing design standards [21] provide only a rough assessment of the RS-induced mean stress effect, by introducing an enhancement factor which is the function of stress ratio and the type of joints. Future work is focused on

establishing a fatigue assessment system for as-welded or HFMI-treated joints quantitatively considering the RS and the stress ratio of fatigue loads. The follow-up studies of fatigue assessments will be based on current work. Once the relation between the HFMI process, the introduced RS, and the improvement in fatigue life have been established, the proposed simulation procedure and the fatigue assessment method can be applied in industries to optimize the HFMI parameters and confirm limits to the usage.

3.6 Summary

In this work, a practical and efficient numerical simulation procedure for HFMI treatment of welded joints was proposed. The recommendations of the FE modeling and determination of DCS parameters were presented in detail. The validity of the HFMI simulation was studied numerically and experimentally in an out-of-plane gusset welded joint. Following conclusions can be drawn.

(1)The simulated welding thermal cycles, as-weld stress, HFMI-induced RS, and peening groove were in good agreement with the measurements. This indicates that the proposed simulation system can effectively predict the HFMI-induced RS with the consideration of the as-welded stress.

(2) The proposed numerical analysis system allowed the use of the different FE mesh in the welding and HFMI simulation steps so that good computational efficiency and accuracy can be achieved.

(3) The radius of the peening tool has been modified to enable more accurate reproduction of the treated local profile. This facilitates the consideration of local stress concentrations and RS relaxation in subsequent fatigue assessment.

(4) Considerable compressive RS (-700 MPa) near the weld toe was introduced after the HFMI treatment compared with the as-welded condition (500 MPa). To accurately evaluate the improvement by the HFMI process the fatigue life of the structures, it is needed to perform stress relaxation analyses after HFMI simulation and investigate the mean stress effect induced by the RS in future work.

CHAPTER 4

Local MIL-HDBK-5D equivalent stress based fatigue assessment for the post weld heat treated gusset welded joint

4.1 Introduction

In Chapter 3, a practical and efficient numerical simulation system for the HFMI treatment of welded joints has been developed. The proposed simulation system can calculate the HFMI-induced compressive RS and improvement of the weld toe profile with the consideration of initial as-welded stress. The final goal of this study is to develop a fatigue assessment approach for HFMI-treated joints, which can quantitatively evaluate the effects of introduced compressive RS and local geometric improvement at the weld toe.

When a welded structure is subjected to cyclic loading, the residual stress can affect the mean stress of stress cycles, thus influencing the fatigue life of the structure. To quantify the mean stress effect, the MIL-HDBK-5D approach is employed in this work. A mean stress-independent stress range can be obtained by this method by local stress ratio correction. The effectiveness of the MIL-HDBK-5D approach for welded structures needs to be first verified by post-weld heat treatment of the joints. This means that only the factor of residual stresses is considered, while maintaining the as-welded toe profile.

In this chapter, a local equivalent stress parameter based on local elastic-plastic stress cycle is applied to evaluate the fatigue life of as-welded and post weld heat treated joints. This new stress parameter allows quantitative assessment of residual stress effect on fatigue life. A set of as-welded and PWHT gusset joints is fabricated using SS400 steel, followed by stress measurements and bending fatigue tests with stress ratios of R=-1. To obtain the stress distributions of specimens, welding, PWHT, and cyclic external load analysis were performed by using elastic-plastic finite element (FE) code JWEIAN. The mean stress effect related to RS was analyzed by using the equivalent stress parameter in MIL-HDBK-5D approach.

4.2 Experimental work

4.2.1 Fabrication of the out-of-plane gusset welded joint

A set of as-welded and PWHT gusset joints were made from SS400 plates with a 16mm thickness to investigate the relationship between RS and fatigue performance. The appearance and dimension of specimens are shown in Fig.4.1, and the mechanical properties of base and filler metal are listed in Table 4.1. The thickness of the gusset plate and base metal is 16mm. The gusset plate is joined to the base metal by CO_2 gas arc welding process, and the wire is JIS YGW11 (equivalent to AWS ER70S-G). The welding parameters are listed in Table 4.2. The toe radius is 0.5 mm.

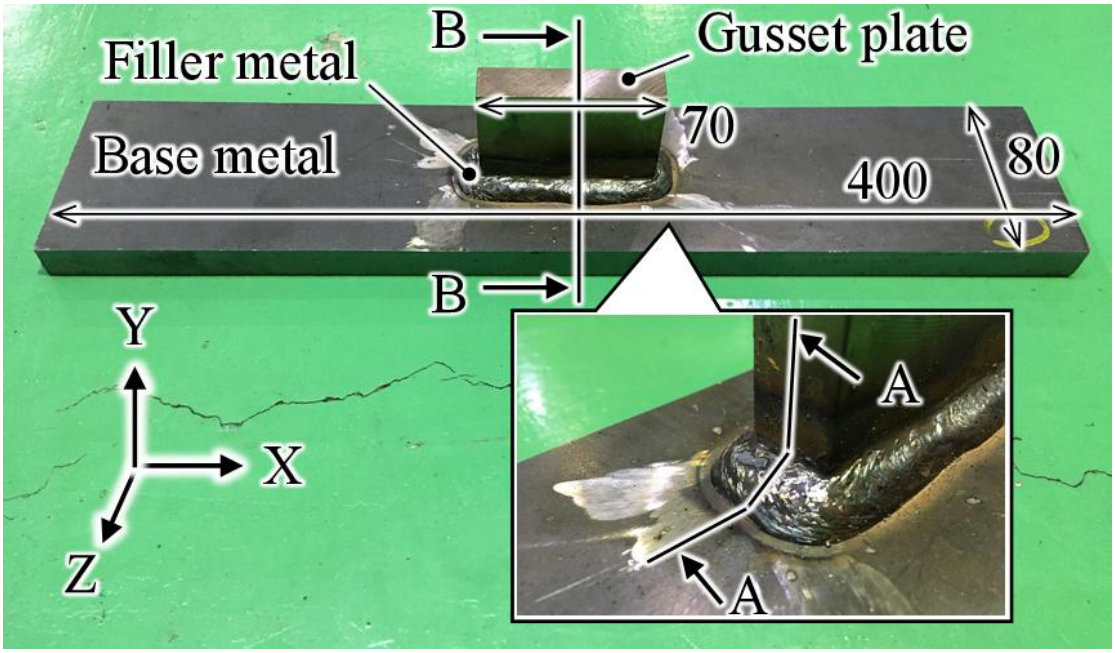

Fig. 4.1 Gusset welded joints and their dimensions (Unit: mm).

Table 4.1 Mechanical properties for out-of-plane gusset welded specimens.

Material	Grade	Yield strength (MPa)	Tensile strength (MPa)
Base metal	SS400	297	467
Gusset plate	SS400	297	467
Filler metal	TGW11	409	501

Table 4.2 Welding parameters.

Weld bead	Current (A)	Voltage (V)	Speed (mm/s)
Fillet	250	28	30

4.2.2 Post-weld heat treatment on the out-of-plane gusset welded joint

After welding, PWHT process is performed with the 1.5 h holding time and 600 °C holding temperature to relieve welding RS. The Furnace temperature histories of PWHT specimens is shown in Fig 4.2.

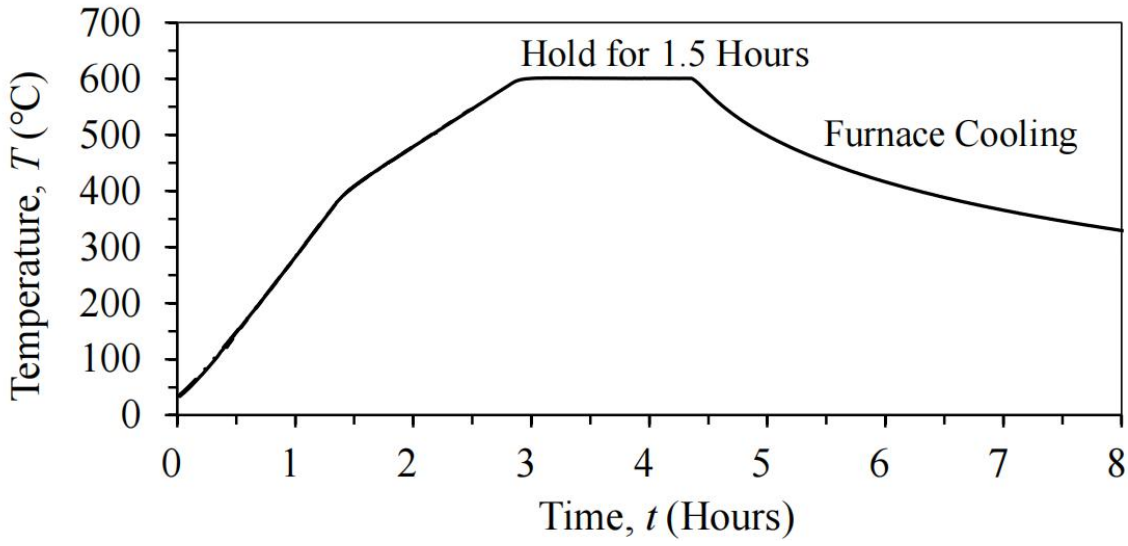

Fig. 4.2 Furnace temperature histories of PWHT specimens.

4.2.3 Residual Stress Measurement

RS in gusset joints are measured by an X-ray stress measurement device (μ-X360s). Electrochemical polishing is used prior to the stress measurement to have a smoother surface and reduce the effect of surface oxides and roughness. The measurement point arrangement for gusset welded joints is shown in Fig 4.3.

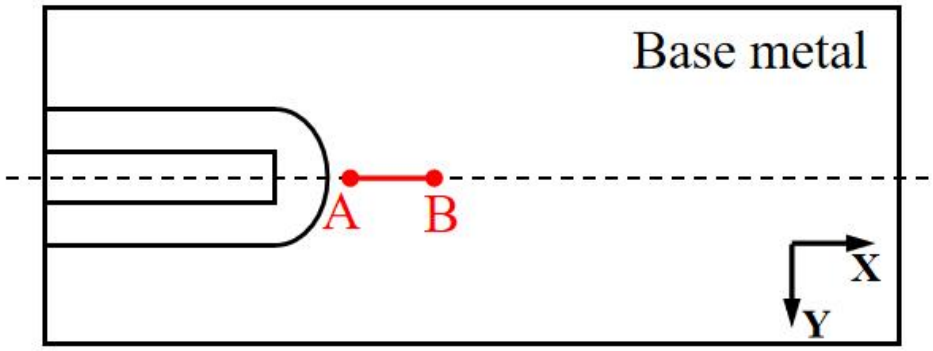

Fig. 4.3 Location of residual stress measurement.

4.2.4 Fatigue Test

4-point bending fatigue tests were conducted for as-welded and PWHT gusset joints, as shown in Fig. 4.4. The Sinusoidal load with a frequency of 8 Hz is applied to the specimen by 4 test fixtures. Stress ratio R of test load were -1. Nominal stress in SN curves is corrected to 0.8 times the surface stress according to JSSC standard [22].

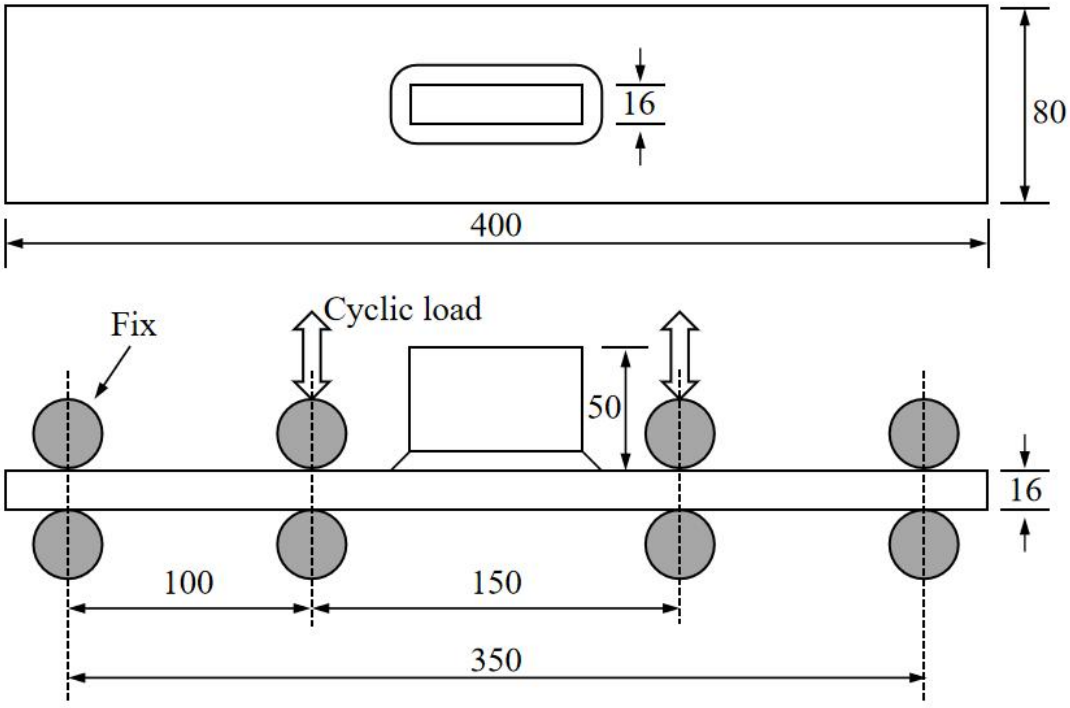

Fig. 4.4 Fatigue test setup (Unit: mm).

4.3 FE Analysis

In the present study, thermal elastic-plastic FE analysis of welding and PWHT processes was performed by FE code JWRIAN which is developed by the Joining and Welding Research Institute (JWRI) of Osaka University [62-64]. Then external cyclic loading analysis was carried out to obtain local elastic-plastic stress cycles considering the as-welded and stress relived RS.

Fig. 4.5 shows the target FE mesh and its geometric details. The FE mesh dimensions follow the experimental specimen. The weld toe radius is 0.5 mm. The total element numbers and nodes are 168,396 and 177,159, respectively. The ultra-fine mesh, with a size of 0.15×0.15×0.15 mm, was applied near the weld toe of the mock-up to accurately calculate local stress.

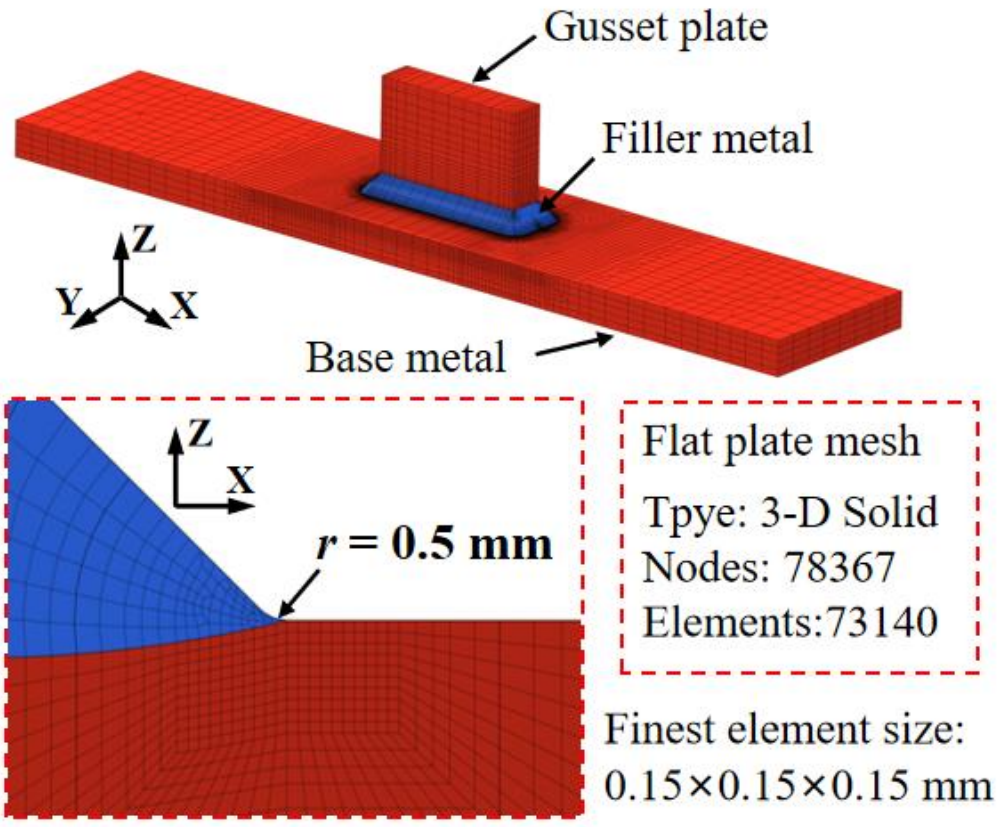

Fig. 4.5 The FE mesh for out-of-plane gusset joints.

In welding simulation, thermal analysis was first carried out to calculate the temperature history data of each node. Heat input from the welding arc was simulated by a half ellipsoid moving heat source with uniform density [66]. The area of heat source action in thermal analysis is given by Eq. (17):

$$\frac{(x-vt)^2}{a^2}+\frac{y^2}{b^2}+\frac{z^2}{c^2}\le 1, \quad (z\le 0) \tag{17}$$

where x, y and z are the coordinates (mm); a, b and c are the shape parameters (mm); v is the forward speed of the heat source (mm/s); t is the time (s). The heat flux q_{h} of moving heat source is calculated by Eq. (18):

$$q_{\mathrm{h}}=\frac{3UI\eta}{2\pi abc} \tag{18}$$

where U is the arc voltage (V); I is the welding current (A); η is the thermal efficiency. The parameters of the heat source are determined and calibrated according to the size of fusion zone obtatined from experiment. Temperature-dependent material properties of base and filler metal [76, 77] were taken into account (Fig. 4.6). Heat transfer between the welded joint and environment was considered by using a temperature-dependent convection coefficient on the outer surface of specimens. The ambient temperature history data obtain by the thermal analysis. The same FE mesh was used for mechanical analysis. The total strain increments can be decomposed into four component (Eq. 19):

$$d\varepsilon_{\mathrm{total}}=d\varepsilon_{\mathrm{e}}+d\varepsilon_{\mathrm{p}}+d\varepsilon_{\mathrm{cr}}+d\varepsilon_{\mathrm{t}} \tag{19}$$

where ε_{e}, ε_{p}, $\varepsilon_{\mathrm{cr}}$ and ε_{t} are the elastic strain, plastic strain, creep strain, and thermal strain, respectively. The elastic behavior follows the isotropic Hooke's rule with temperature-dependent mechanical properties. The plastic strain was calculated based on flow plasticity theory and Von Mises yield surface. Creep behavior was considered in the welding and PWHT processes, and Norton-Bailey law [78] was used to calculate the creep strain as below:

$$\varepsilon_{\mathrm{cr}}=C_0\sigma_v^{\,C_1}t^{C_2}e^{-\frac{C_{\mathrm{T}}}{T+273.15}} \tag{20}$$

where T is temperature; σ_v is Von Mises stress; C_0, C_1, C_2, and C_{T} are the creep parameters, and their values are listed in Table 4.3. The thermal strain was determined

by simulated temperature histories, and the thermal expansion coefficient of the material was assumed to be the same in all directions. A minimal external constraint was applied in welding and PWHT simulation only to prevent rigid body movement of mock-up.

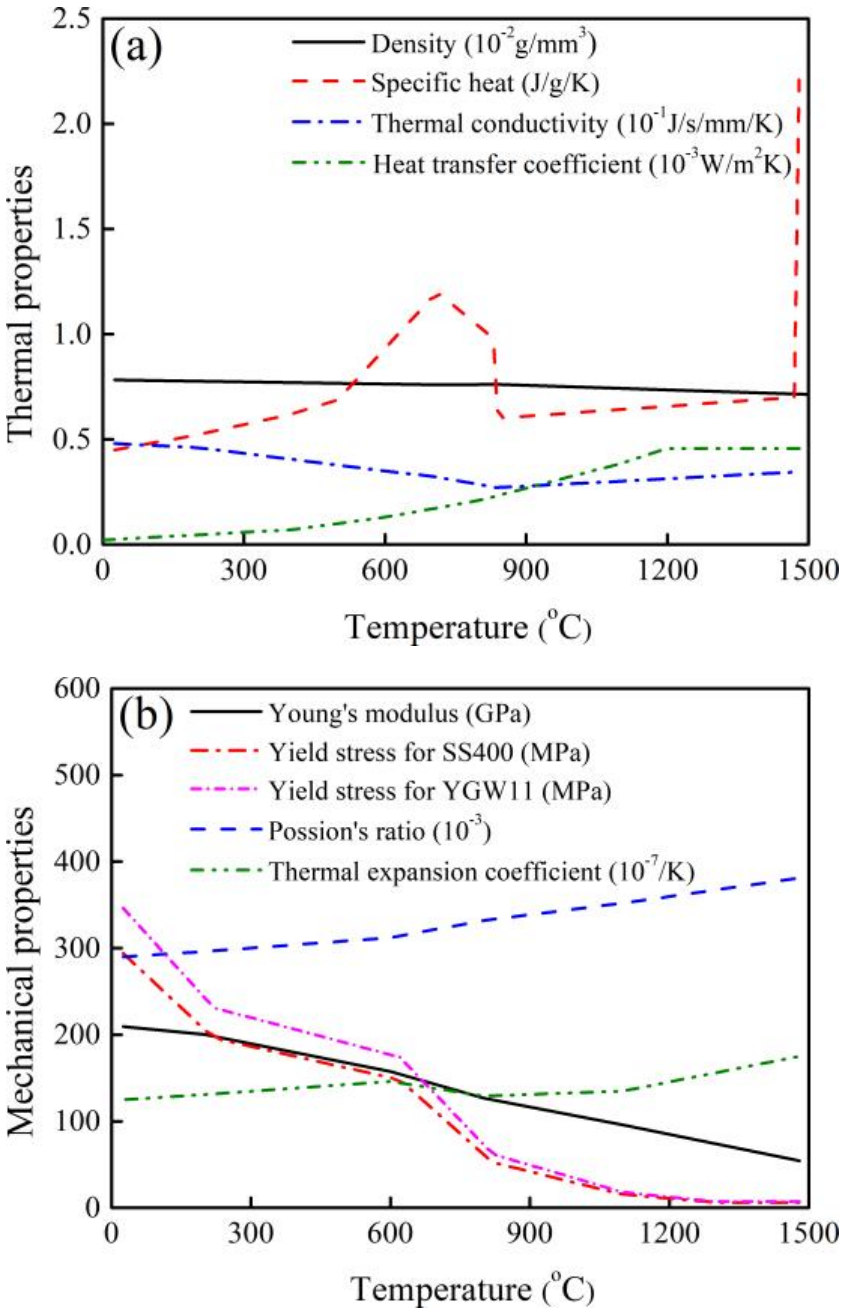

Fig. 4.6 Material properties of SS400 and YGW11: (a) thermal properties, (b) mechanical properties.

Table 4.3 Creep parameters of SS400.

C_0 (MPa^{-1})	C_1	C_2	C_T (°C)
1.43×10^{-7}	1.9	0.46	2315.8

The cyclic loading analysis was carried out considering as-welded and stress relived RS. External loads are applied to the specimen by means of nodal forces. The locations of applied nodal force correspond to that of fixtures used in fatigue tests (Fig. 4.4). Only three load cycles are considered in the simulations.

4.4 Comparison of simulated RS results with experiment

The distributions of RS in the longitudinal component near the weld toe of gusset joints are shown in Fig. 4.7. It can be observed that high tensile stress with a peak of 400 MPa was introduced around the weld toe after the welding process. This high tensile RS increases the mean stress level of the local stress cycle induced by fatigue loading and thus affects the initiation and propagation of fatigue cracks. After PWHT at 600 °C for 1.5h, the RS near the weld toe decreased significantly, with a peak stress of 65 MPa. Fig. 4.8 shows the comparison of simulated and X-ray-measured RS (σ_{xx}) near the weld toe. Red dots include the RS test data on six as-welded specimens while blue square dots represent measured data from three PWHT specimens. The measured data are slightly scattered due to the slight differences in actual welding conditions and the initial state of the material among each joint. Overall, the simulated RS shows a good agreement with measured data which validates the simulation model used.

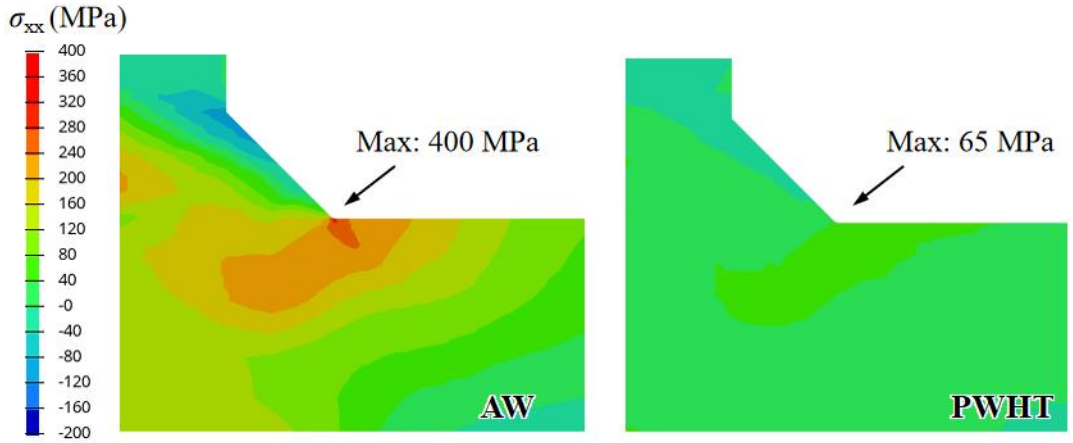

Fig. 4.7 The distributions of longitudinal stress (σ_{xx}) near the weld root of gusset joints

in as-welded and stress-relieved conditions

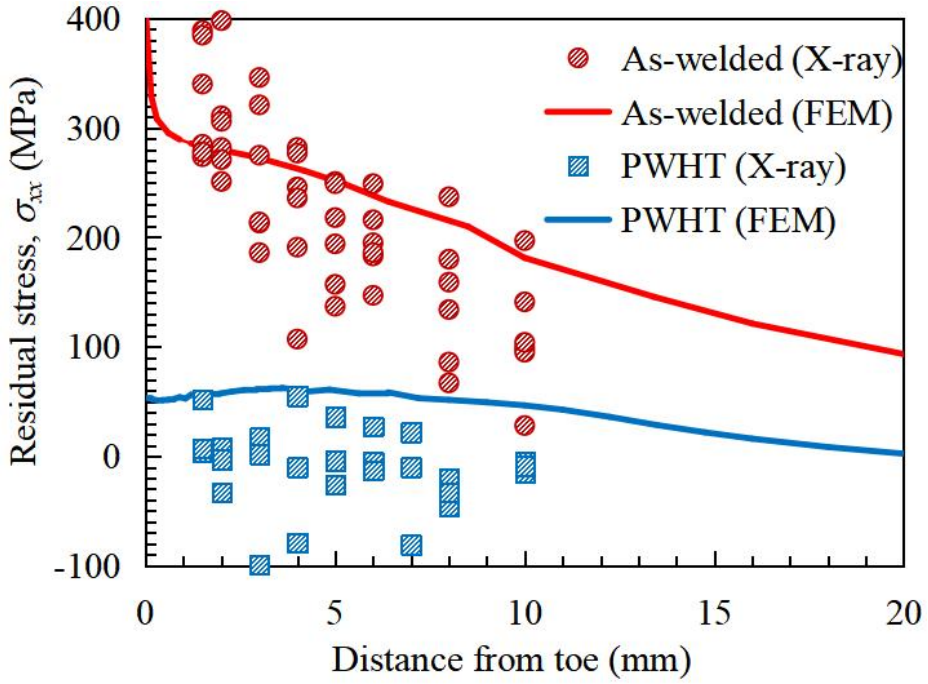

Fig. 4.8 Comparison of simulated and X-ray-measured RS (σ_{xx}) near the weld toe of gusset joints.

4.5 Local MIL-HDBK-5D equivalent stress based fatigue data

Fig. 4.8 presents the relationship between the fatigue life of specimens and applied nominal stress range (0.8 times the surface stress range [22]). It is observed that the fatigue life of stress-relieved joints is approximately 2.5 times longer than as-welded ones with a stress ratio = -1. The mean stress effect results in each group of specimens having its own trend in S-N data, even though they have the same geometrical details.

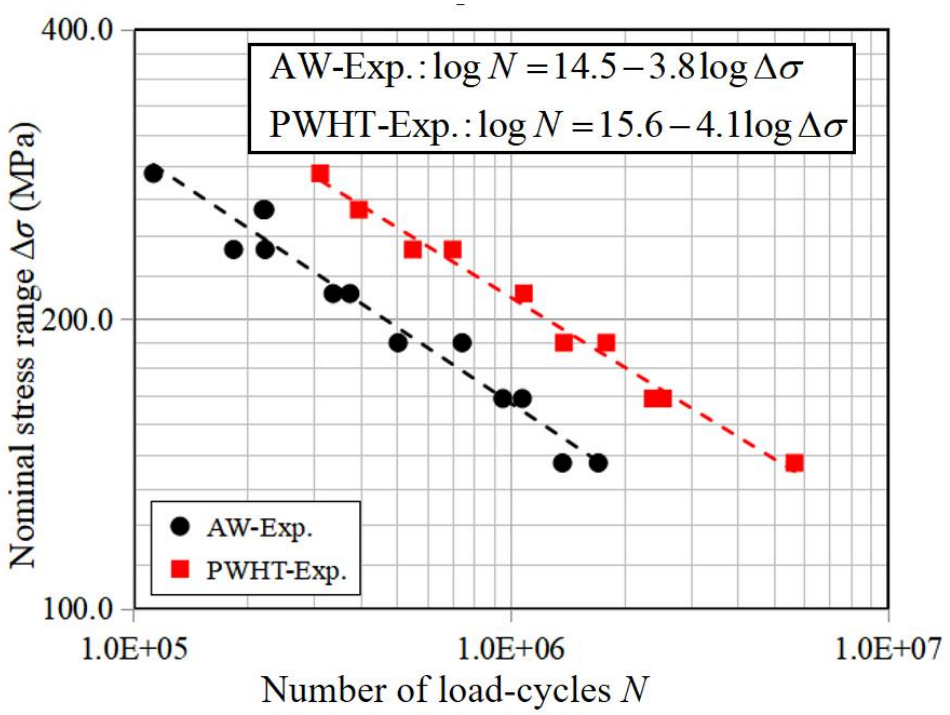

Fig. 4.8 Nominal stress based S-N data for as-welded and stress-relieved gusset joints

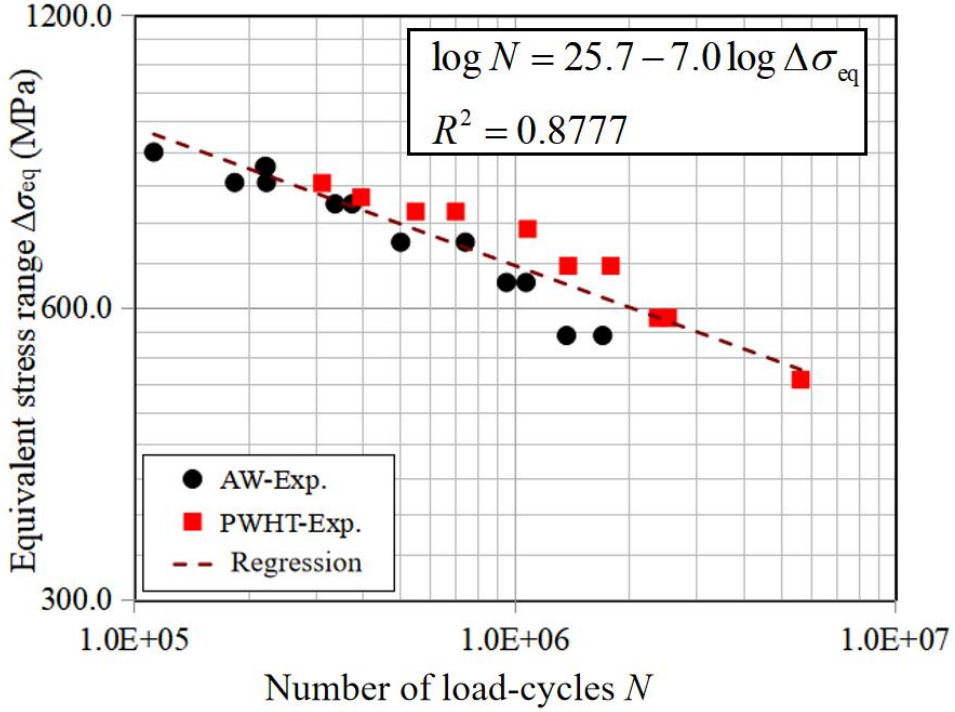

Fig. 4.9 Local equivalent stress based S-N data for as-welded and stress-relieved gusset joints

To consolidate the S-N data with or without stress relief and stress ratios, MIL-

HDBK-5D approach [60-61] was used in the current work. Equivalent stress based on the local elastic-plastic stress cycle was applied as the stress parameter of the S-N plot, as below:

$$\Delta\sigma_{eq} = \left(\sigma_{t-max}\right)^{1-\alpha}\left(\Delta\sigma_{t}\right)^{\alpha} \;;\; \alpha = 0.6485 \tag{21}$$

where $\Delta\sigma_t$ is the range of the tangential stress component on the surface of the weld toe/peening groove; $\sigma_{t\text{-}max}$ is the maximum value of the tangential stress cycle. α is a fitted constant. Only single cyclic loading was performed by elastic-plastic FE analysis, as the plastic behavior occurs mainly in the first cycle for constant amplitude loads. By examining the local stress cycles near the weld toe in each case, the local equivalent stress based S-N plot can be obtained, as shown in Fig. 4.10. It is observed that the fatigue data from the gusset joints with different RS essentially fall into the same band.

It is noted that the present approach is based on the local elastic-plastic stress cycle calculated using ultra-fine FE mesh (0.15 mm), which avoids the notch singularity of elastic FE analysis and takes the RS effect into account. Therefore, this approach differs from the effective notch stress method [79] using virtual notches mesh. In addition, the actual notch size of each specimen varies while the FE mesh size at the weld toe was referenced to the average size of specimens. This uncertainty leads to an increase in S-N band dispersion. This potential impact is acceptable from the local equivalent stress-based S-N data (Fig. 4.10). The results in Fig. 4.10 suggest that local equivalent stress can be used to establish a design S-N curve independent of RS and stress ratios and allows a quantitative assessment of the effect of RS on fatigue performance.

4.6 Summary

Both numerical and experimental investigations were carried out to study the mean stress effect on fatigue performance based on as-welded and stress-relieved gusset joints. The main conclusions can be summarized as follows:

(1) The as-welded and stress-relieved RS obtained by thermal elastic-plastic FE analysis match well with the X-ray measured ones, which validates the developed analysis method and employed input parameters.

(2) The RS level in stress-relieved joints decreased significantly compared with that

in the as-welded condition, with its peak value dropping from 400 MPa to 65 MPa. The fatigue life of stress-relieved joints is approximately 2.5 times longer than as-welded ones with a stress ratio = -1.

(3) The fatigue data of as-welded and PWHT specimens can be approximated by a single local equivalent stress based S-N curve. This reference SN-curve can be used for evaluating the fatigue life of welding joints at arbitrary RS and stress ratios.

CHAPTER 5

Local MIL-HDBK-5D equivalent stress based fatigue assessment of the gusset welded joint improved by high-frequency mechanical impact treatment

5.1 Introduction

The objective of this chapter is to propose a local approach for fatigue life assessment of HFMI-treated joints which can consider the influence of HFMI-induced RS and improved weld toe geometry. The local MIL-HDBK-5D equivalent stress (LMES) range $\Delta\sigma_{eq}$ [59-61] is employed as the stress parameter for fatigue assessment. This stress parameter is identified from the local stress cycle along the surface of the HFMI groove for specimens subjected to cyclic loads. The local stress cycle is simulated by a muti-process simulation system including thermal-elastic-plastic FE (TEP-FE) welding analysis, dynamic explicit elastic-plastic FE (EP-FE) HFMI analysis, and EP-FE cycling loading analysis. To validate the proposed fatigue assessment approach, a set of AW and a set of HFMI out-of-plane gusset joints are fabricated using SM490 steel, followed by uni-axial fatigue tests with stress ratios of R = 0. Combined with the simulated stress results, the LMES based S-N curve is calculated, which enables a quantitative evaluation of the improvement effects of HFMI treatment.

5.2 Experimental work

In total, 13 out-of-plane gusset joints (1 Type-1 joint and 12 Type-2 joints) are fabricated using SM490 steel with a thickness of 9mm for the main plate and 6mm for the longitudinal stiffener. The longitudinal stiffener is joined to the main plate by the two-pass welding process. The weld type is fillet weld. The specimen geometry and welding sequence are shown in Fig. 5.1. Herein, the Type-1 joint is used to investigate the RS in AW and HFMI conditions as presented in our prior work [80]. Type-2 joints are used for the fatigue test. The welding method is gas metal arc welding using the shield gas of 80% Ar and 20% CO_2, and the filler metal is YGW11 (MG50). All specimens are fabricated using the same welding parameters, as listed in Table 5.1.

Subsequent to the welding, the HFMI treatment is performed along the entire length of the weld toe of gusset joints. A portable pneumatic needle peening device (Toyo

Seiko NP1000F20) is employed for treatment with an air pressure of 0.5 MPa. A peening tool with a tip radius of 1.5 mm is used. The travel speed for treatment is 5 mm/s and the hammering frequency is 80 Hz. The IIW recommendations [33] stipulate that the HFMI must have a hammering frequency f of 90 Hz or higher. However, because it is considered that the fatigue improvement effect for the case with f = 80 Hz is equivalent to that for f = 90 Hz, the hammering treatment performed by the chosen tool is described as HFMI treatment in this work.

Uni-axial fatigue tests are performed for AW and HFMI joints following the JSSC standard [22], as shown in Fig. 5.2. The fatigue test machine is a customized electro-hydraulic servo testing machine manufactured by Shimadzu Corporation. The sinusoidal load is applied to the specimen. The testing frequency is 10 Hz, and the stress ratio R is 0. The number of cyclic loads experienced for each specimen is recorded until totally fractured. The effects of welding-induced misalignment (1 mm) on fatigue performance are estimated by IIW recommended formula [21]. The misalignment effects are presented by a magnification factor of k_m = 1.07, which is discussed in Appendix A.

Table 5.1 Welding parameters.

Pass	Current (A)	Voltage (V)	Speed (mm/s)	Inter-pass temperature (oC)
1	210	20	3	100
2	210	20	3	-

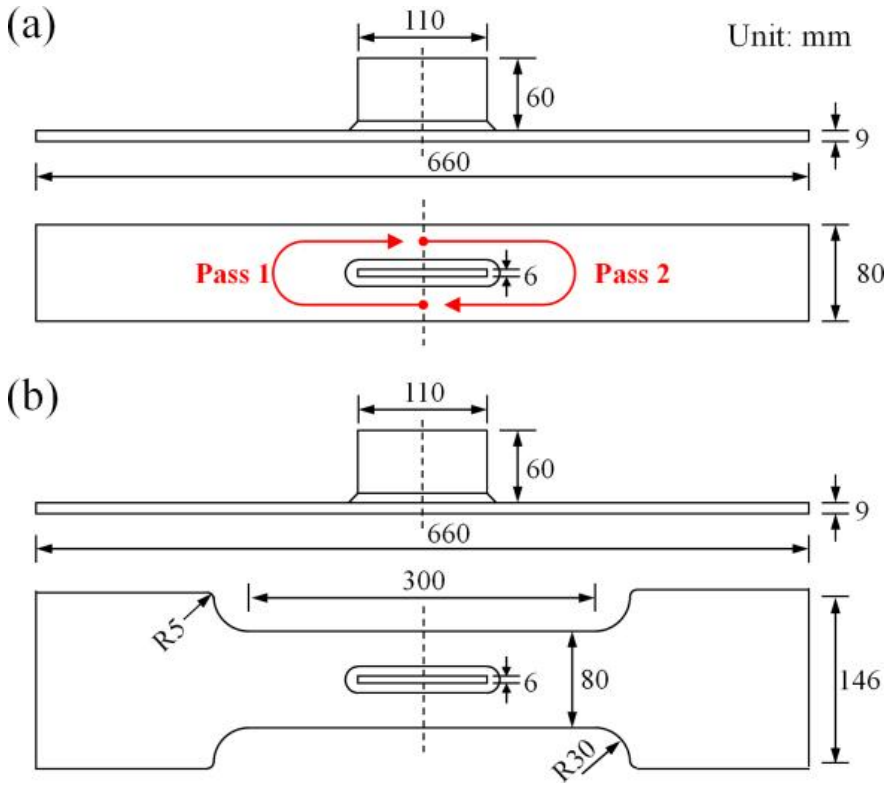

Fig. 5.1 Specimen geometry and welding sequence. (a) Type-1 joint, (b) Type-2 joint.

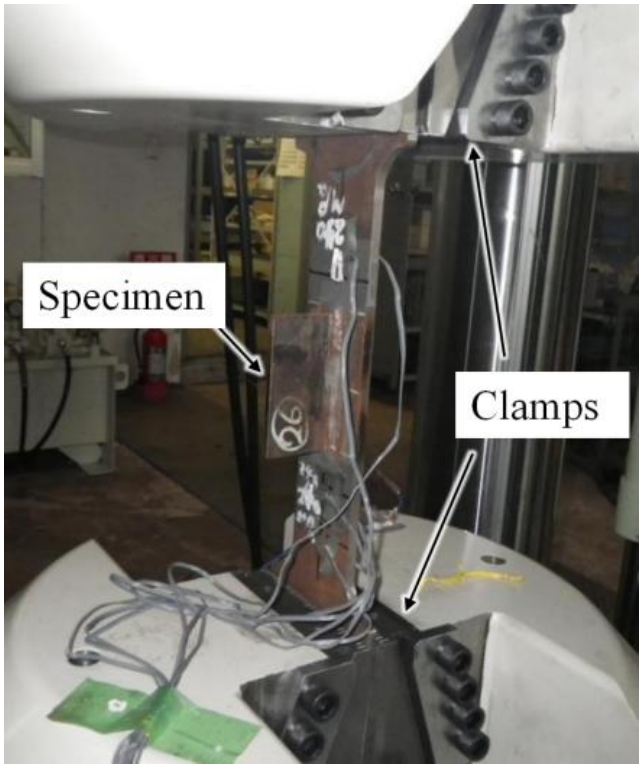

Fig. 5.2 Fatigue test setup.

5.3 Numerical assessment approach of fatigue Life

The flowchart of the proposed fatigue life assessment is shown in Fig. 5.3. This approach allows the consideration of the local RS and weld profile. To obtain the local stress response due to fatigue loads, simulations of welding, HFMI treatment, and cyclic loading are carried out in sequence. TEP-FE analysis of the welding process is first performed by JWRIAN, which is an FE code with high computing speed developed by The Joining and Welding Research Institute (JWRI) of Osaka University [19, 20]. Then, dynamic explicit EP-FE analysis of the HFMI treatment is performed by commercial FE code MSC. Dytran using an ultra-fine FE mesh. A stress interpolation code is developed based on the Griddata function of Numpy [21] to transfer stresses from welding analysis output (coarse FE mesh) to HFMI analysis input (ultra-fine FE mesh) as initial stress load. Subsequently, EP-FE analysis of cyclic loading is carried out by MSC. Dytran using the same mesh as that in HFMI analysis but considering the local deformation induced by HFMI. The applied cyclic loads follows experimental fatigue loads. Finally, based on the MIL-HDBK-5D approach [15-17], the LMES is calculated according to elastic-plastic local stress cycle (EP-LSC) obtained by EP-FE analysis. In combination with the fatigue test data, local equivalent stress based S-N curve is derived. This new S-N curve can be used for evaluating the fatigue lives of welding joints with arbitrary RS distribution and stress ratios.

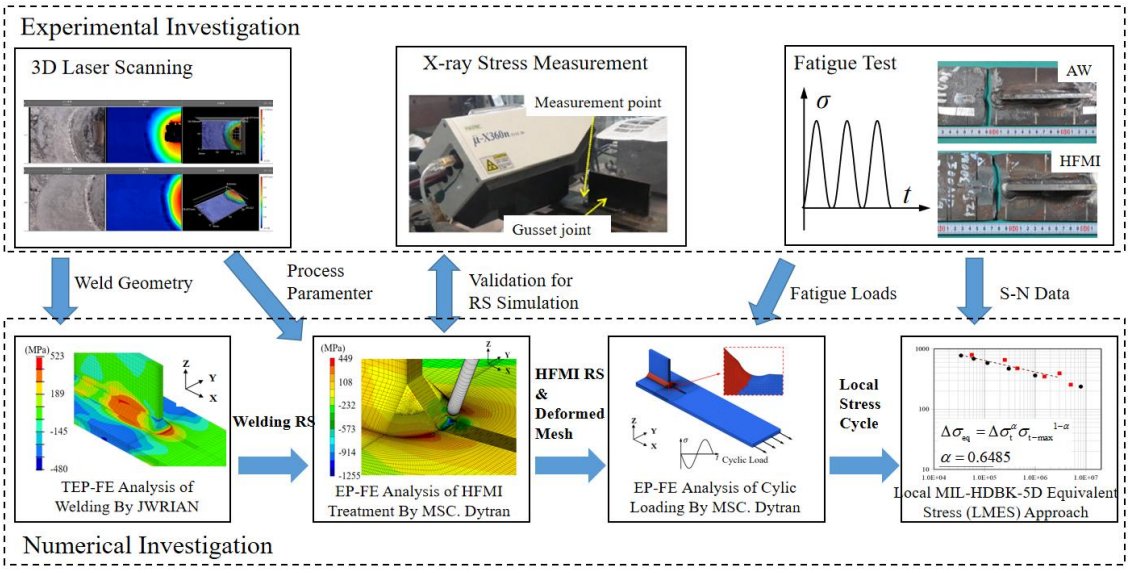

Fig. 5.3 Flowchart of the FE analysis and LMES based fatigue assessment.

5.3.1 Welding simulation

A 3-D FE mesh model is built with the same size as the experimental specimen, as shown in Fig. 5.4. The finest element with dimensions of 0.5×0.5×0.5 mm is arranged near the round seam, where the weld toe in this region is the target region for subsequent HFMI treatment. The weld log is 8 mm and the flank angle of the weld seam is 45^{o}. The element type used is an 8-node solid element with 8 Gauss integration points. The total number of elements is 177, 092 while the number of nodes is 193, 639.

Thermal analysis is first performed to calculate the transient temperature field. A half-ellipsoid moving heat source is employed to simulate welding heat input, and its heat flux distribution of the heat source model is assumed to be uniform [66]. The welding parameters and sequence in simulations are consistent with the experiment. The inter-pass and ambient temperatures in simulations are set to 100 ^{o}C and 20 ^{o}C, respectively. The heat loss from the specimen to environment is considered through a thermal boundary on the outer surface with a temperature-dependent convection coefficient [80]. After thermal analysis, mechanical FE analysis is then performed to calculate welding RS and deformation. The transient temperature history data obtained by thermal analysis is applied as a thermal load. Three nodes on the bottom surface of the main plate are constrained in XYZ, XZ, and Z-directions respectively to prevent rigid body movement. Temperature-dependent material properties of SM490 (base metal) are used [80], as shown in Fig.5.5. The material properties of the filler metal are assumed to be the same as the base material. For welded joints made of low-alloy structure steel, the solid-state phase transformation and strain hardening has negligible effects (< 100MPa) on welding RS [68]. Therefore, an ideal elastic-plastic material model without consideration of the strain hardening and phase transformation is used in the welding simulation.

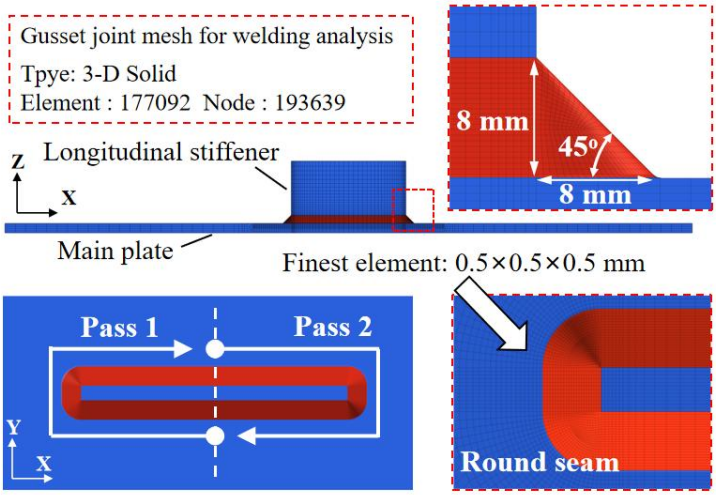

Fig. 5.4 Coarse FE mesh of gusset joint used in welding analysis.

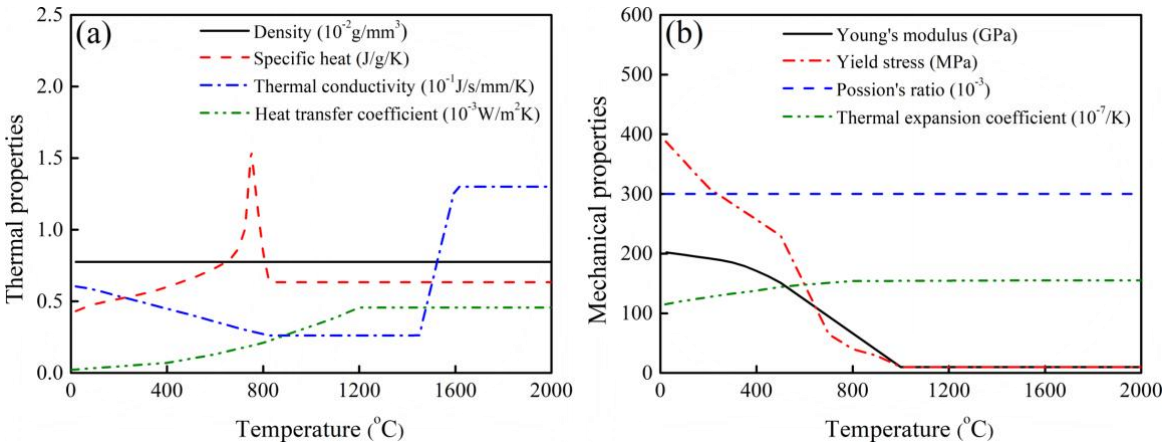

Fig. 5.5 Material properties of SM490. (a) Thermal properties, and (b) mechanical properties.

5.3.2 HFMI simulation

After a welding analysis, a simulation is conducted for HFMI treatment using a fine FE mesh with a minimum element size of 0.15×0.15×0.15 mm in the peening treated zone. As shown in Fig. 5.6, only one half of the gusset joints are considered in the analysis to save time, with the Y-Z plane serving as the symmetric plane. The peening tool is modeled as a rigid surface using 4-node 2D shell elements. For convenience, the tip radius of the tool is increased to 2.05 mm in the FE model, while its actual size is 1.5 mm, to consider the tool's aberration and lateral movement [80]. This optimized tool shape helped improve the accuracy of the simulated local profile. The initial stress of the HFMI simulation is AW stress simulated by the JWRIAN code. Due to

differences in FE mesh, the interpolated AW stress, including 6 stress components (normal stresses σ_x, σ_y, σ_z, and shear stresses τ_{xy}, τ_{yx}, τ_{xz}), is calculated using a stress interpolation code developed based on the Griddata function of Numpy [72]. The interpolated stress is then written in Dytran's input file, which is used for HFMI simulation. In addition, the load rate scaling method is employed to save analysis time. The up-scaling rate is set to 80 [80].

The displacement-controlled simulation method is employed in HFMI analysis, due to easier access to analysis parameters and shorter computation times compared to the force-controlled method [41-44]. The movement of the peening tool is given, as follows:

$$\begin{cases} X_x = a\cos\theta\sin(2\pi ft) \\ X_y = v_F t \\ X_z = a\sin\theta\sin(2\pi ft) \end{cases} \tag{22}$$

where X_x and X_z represent the componets of tool's axial motion; X_y is the motion in the forward direction along the welding toe; v_F is the forward speed; a is the peening stroke (see Fig. 5.6); θ is the peening angle; f is the peening frequency; and t is the time. The peening stroke a can be calculated by following equations:

$$a = \frac{1}{\sin\theta}[d + u_e - r(1-\sin\theta)] \tag{23}$$

where u_e is the enforced indentation; and r is the radius of the tool's tip. It is hard to directly identify the enforced indentation u_e by measurements due to the elasticity of the material. Therefore, the relation between ue and the peening depth is established in trial and error manner. From this relation, then ue can be determined based on measured peening depth [80]. In mechanical analysis, all nodes on the back face of the main plate are constrained in Z-directions, and nodes on the symmetric plane are constrained in the X direction. The contact between the pin and the weld bead / base metal is modeled as follows: The FE mesh of the peening tool is defined as the master surface in the contact pair, while the upper surface of the specimen is defined as the slave surface. The friction coefficient in the contact model is assumed to be 0.3.

In HFMI modeling, the choice of the material hardening model is crucial due to the

substantial local plastic deformation brought on by repeated hits. The non-linear isotropic hardening model is chosen in this work without the consideration of strain rate-dependency. In MSC. Dytran, the elastic modulus E and yield strength f_y are updated with incremental steps according to the stress-strain curve [80] and accumulated plastic strain ε_p. The initial elastic modulus E and initial yield strength f_y are set to 210 GPa and 388 MPa, respectively. The Poisson's ratio ν is set to 0.3.

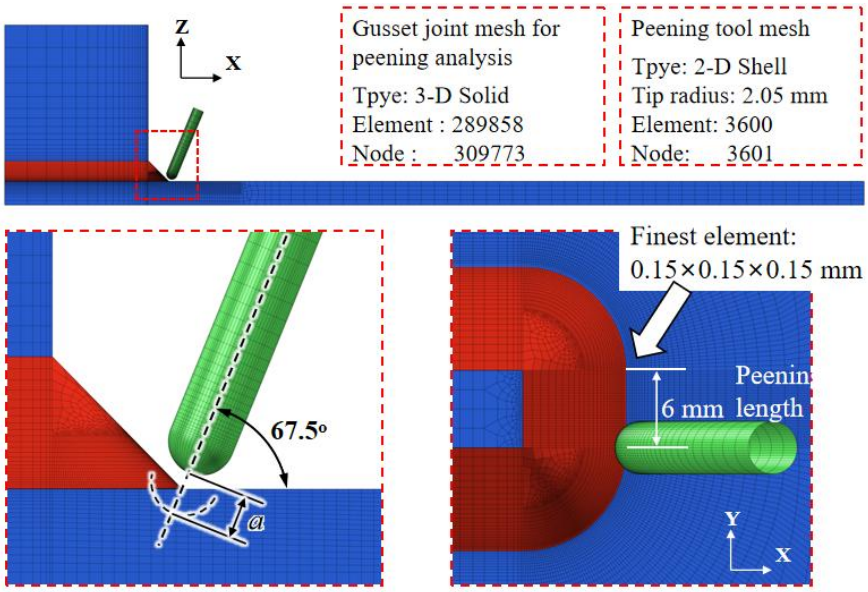

Fig. 5.6 Fine FE mesh of gusset joint and peening tool in HFMI analysis.

5.3.3 Cyclic fatigue load simulation

After the welding and peening simulation, the EP-FE analysis of cyclic loading is conducted using MSC. Dytran to investigate the local stress response under fatigue load. A total of 12 simulation cases are performed based on the loading condition of each fatigue test, as listed in Table 2. Only three load cycles are considered in the simulations. To save analysis time, the frequency of the cyclic load in simulations is assumed to be 600 Hz [41]. For Cases AW-1 to AW-6, the interpolated AW stress is given as the initial stress. The fine mesh with original weld toe radius of 0.8 mm is used, and its element size near the weld toe is 0.08 × 0.08 × 0.08 mm. For Cases HFMI-1 to HFMI-6, the HFMI-induced RS and equivalent plastic strain are given as the initial state, and the deformed mesh model is applied to consider the weld toe geometry improvement by HFMI treatment, as shown in Fig. 7. The nodes in the specimen's back face are constrained in the Z-direction, and a symmetric boundary condition is imposed

to the Y-Z plane simultaneously. It should be emphasized that the test specimens are not symmetric about the Y-Z plane. According to the elastic FE analysis, such an additional symmetric constraint leads to a local stress (hot spot stress) increase of 3%, which is considered negligible in the present study (see in Appendix B). The material properties and hardening model are consistent with those used in the peening analysis.

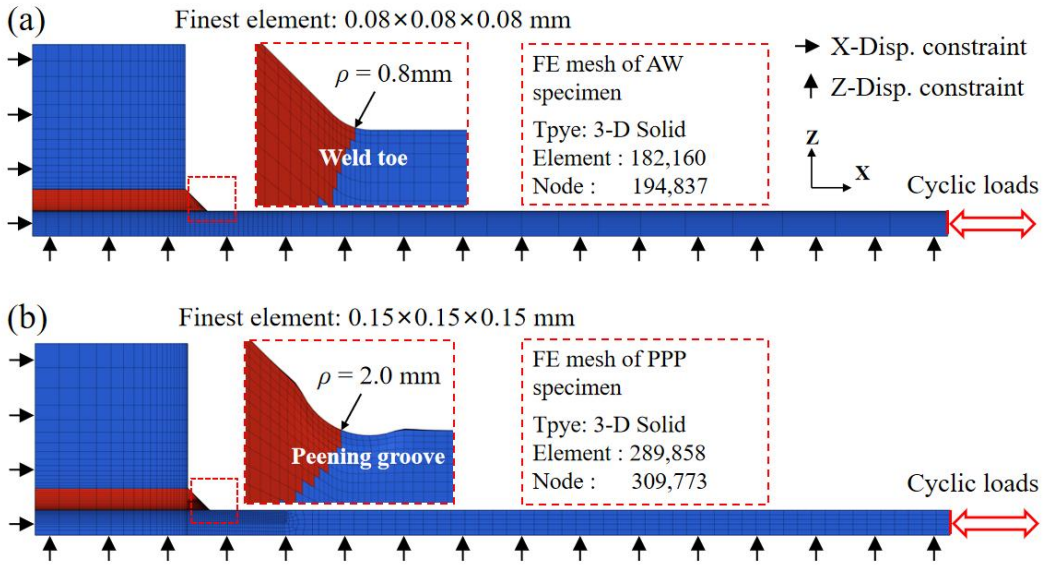

Fig. 5.7 Fine FE mesh of the gusset joint used for cyclic load analysis. (a) AW case; (b) HFMI case.

Table 5.2 Simulation cases for cyclic loading.

Specimen number	Nominal stress range $\Delta\sigma$ (MPa)	Stress Ratio R	Number of Cycle N
AW-1	53.6 (0.14 f_y)	0	3
AW-2	103.0 (0.27 f_y)	0	3
AW-3	152.2 (0.39 f_y)	0	3
AW-4	203.7 (0.53 f_y)	0	3

AW-5	252.4 (0.65 f_y)	0	3
AW-6	301.8 (0.78 f_y)	0	3
HFMI-1	150.9 (0.39f_y)	0	3
HFMI-2	171.8 (0.44 f_y)	0	3
HFMI-3	181.6 (0.47 f_y)	0	3
HFMI-4	201.6 (0.52 f_y)	0	3
HFMI-5	252.5 (0.65 f_y)	0	3
HFMI-6	304.3 (0.78 f_y)	0	3

5.3.4 LMES based fatigue assessment approach

It is well-known that the RS has a significant impact on the fatigue behavior of welded joints. The tensile RS increases the mean stress level of the fatigue cycle, resulting in a reduction in the fatigue life of structures. Additionally, the stress ratio R also has a considerable effect on fatigue life, particularly for stress-relieved or HFMI-treated joints. This is because the compressive stresses introduced by these treatments, which improve fatigue performance, relax under fatigue loading. The stress relaxation induced by the cyclic load increases with the stress ratio R. The stress relaxation reduces the fatigue improvement achieved by HFMI treatment, as listed in Table 5.3.

For load-control fatigue data, MIL-HDBK-5D Standard [59] provides an approach to consolidate the S-N data of aluminum alloy materials at various stress ratios based on an equivalent stress parameter Δσn-eq. The new S-N curve is described by the following equation:

$$\Delta\sigma_{\text{n-eq}} = \sigma_{\max}\left(1-R\right)^{\alpha} \tag{24}$$

$$\log N = c_1 + c_2 \log \Delta\sigma_{\text{n-eq}} \tag{25}$$

where $\sigma_{\max}$ is the maximum value in the nominal stress cycle; R is the stress ratio; N is the number of cycles to failure; c_1, c_2, and α are material parameters.

Matsuoka et al.[60, 61] investigated the fatigue crack initiation life of welded joints using the MIL-HDBK-5D approach. The hot-spot stress component based equivalent stress range $\Delta\sigma_{\text{h-eq}}$ can be described as the following equation:

$$\Delta\sigma_{\text{h-eq}} = (K\Delta\sigma)^{\alpha} \left(K\Delta\sigma_{\max} + \sigma_{\text{RS}}^{*} \right)^{1-\alpha} \tag{26}$$

$$\sigma_{\text{RS}}^{*} = \begin{cases} f_{\text{y}} - K\Delta\sigma_{\max} & ;\ f_{\text{y}} < K\Delta\sigma_{\max} + \sigma_{\text{RS}} \\ \sigma_{\text{RS}} & ;\ \text{otherwise} \\ -f_{\text{y}} - K\Delta\sigma_{\min} & ;\ -f_{\text{y}} > K\Delta\sigma_{\min} + \sigma_{\text{RS}} \end{cases} \tag{27}$$

where f_{y} is the yield stress; K is the structural stress concentration factor; $\Delta\sigma$ is the nominal stress range; $\sigma_{\min}$ is the minimum stress in the fatigue cycle; σ_{RS} is the residual stress; $\sigma_{*\text{RS}}$ is the stabilized residual stress. Stress relaxation is determined by the yield strength of materials and the hot-spot stress. Eq. (27) explains the variation in the RS due to fatigue loading. In their study, a series of fatigue test data in AW conditions were analyzed. The welding RS for each specimen was estimated by the inherent strain method. Matsuoka utilized the least squares method to fit the material parameter α = 0.6485 in Eq. (26). Yamamoto [81] examined the effectiveness of the modified MIL-HDBK-5D approach using the available data (failure life) of HFMI-treated joints and as-welded joints. Then, he applied this method to the actual fatigue damages in the end connection of side longitudinal stiffeners of midsize double hull tanker.

The current study develops a multi-process simulation system, including welding, HFMI, and fatigue loading, to access the local stress cycle. The effects of local elastic-plastic material behavior, initial RS, and stress ratios R are taken into account in the local stress simulated by EP-FE analysis. Therefore, the LMES range $\Delta\sigma$eq can be simplified as follows:

$$\Delta\sigma_{\text{eq}} = \left(\Delta\sigma_{\text{t}} \right)^{\alpha} \left(\sigma_{\text{t-max}} \right)^{1-\alpha} \tag{28}$$

where $\Delta\sigma_{\text{t}}$ is the range of the tangential stress component on the surface of the weld

toe/peening groove; $\sigma_{t\text{-}max}$ is the maximum value of the tangential stress cycle. The $\Delta\sigma_{eq}$ is assumed to be 0, if $\Delta\sigma_{t\text{-}max} < 0$. It should be noted that the stress parameter utilized in this study is obtained through elastic-plastic FE analysis, using a mesh model featuring the actual notch shape. This differs from the effective notch stress approach [79], which employs a fictitious notch with a radius of 1 mm.

Table 5.3 Reduction of FAT class in fatigue strength improvement by HFMI based on stress ratio R [33].

Stress ratios R	Minimum FAT class reduction
$R \leq 0.15$	No reduction due stress ratio
$0.15 < R \leq 0.28$	One FAT class reduction
$0.28 < R \leq 0.4$	Two FAT class reduction
$0.4 < R \leq 0.52$	Three FAT class reduction
$0.52 < R$	No data available

5.4 Results and discussion

5.4.1 Residual stress for AW and HFMI specimens

In Fig. 5.8, the predicted welding RS along the Path AB on the upper surface is compared to the X-ray stress measurement from the previous studies by our lab [80]. The simulation showed that the RS is about 100 MPa larger than the measured one in areas 5-20 mm away from the weld toe. This difference is attributed to the initial compressive RS on the surface of the plates before welding, which is not accounted for in the simulation. However, the simulated results are in good agreement with the measured RS in regions close to the weld bead. This is because the material in these regions was heated to a high temperature during welding, which caused the initial stresses to be released and thus have negligible effects on final stress distribution.

Fig. 5.9 compares the HFMI-induced RS predicted by FEM with the measured

results [18]. It is observed that the HFMI treatment introduces considerable compressive RS in the vicinity of the treated zone compared to the AW condition. The simulated RS is in good agreement with the measured data for regions close to the weld toe. However, a stress discrepancy of about 100 MPa occurred in areas 7 mm away, similar to the welding RS situation. Since this work focuses on the stress near the weld toe, which is related to the fatigue strength of structures, rather than other regions, this difference is considered to be acceptable.

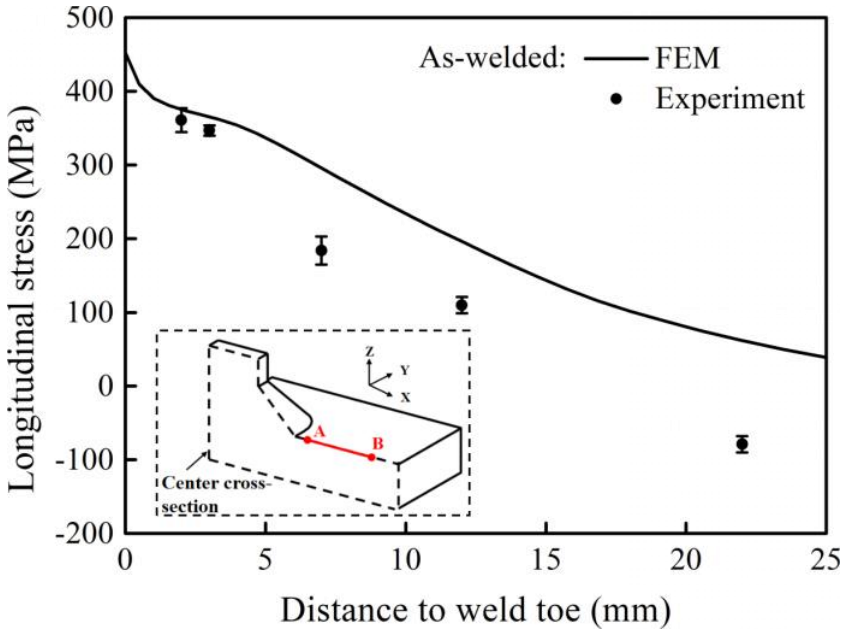

Fig. 5.8 Comparison of the predicted and measured RS distribution along the Path AB on the upper surface for AW Specimen.

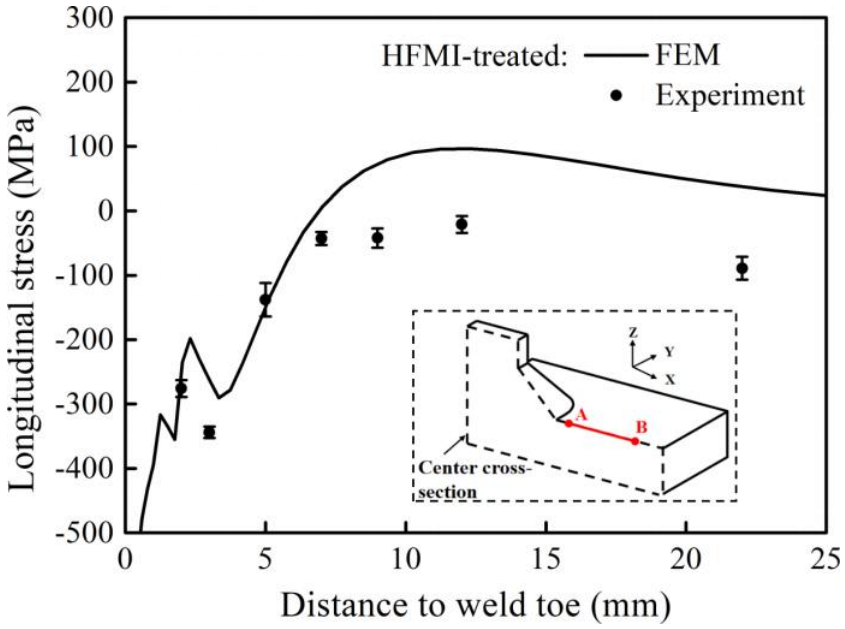

Fig. 5.9 Comparison of the predicted and measured RS distribution along the Path AB on the upper surface for HFMI Specimen.

Fig. 5.10 compares the predicted HFMI-induced RS along the thickness direction with available measured data from Ref. [82-84]. The RS distribution along the thickness direction shows that HFMI treatment introduces the compressive RS up to a depth of 2 mm. For regions close to the surface of the HFMI groove, the compressive RS is higher than the yield stress of the material. The RS measured data [82-84] show a scatter to some extent, which may be due to differences in the yield stress of materials and process parameters (including welding and HFMI). However, the trend of simulated RS distribution in the present work is consistent with the RS measured data in previous studies. This indicates that the FE model used in this study can effectively simulate the distribution of HFMI-induced RS along the thickness direction.

It should be noted that only 6 mm of the peening treatment along the weld toe is carried out in simulations to save the solution time, while all weld toes on the specimens are enhanced by the HFMI treatment in experiments. However, the simulated RS distribution on the cross-section still matches the stress measurements as presented in Fig. 5.9 and 5.10, which indicate that the peening-induced RS is a highly localized and self-equilibrated stress and the stress at remote areas has less impact on the RS near the peening-treated zone. Therefore, in the subsequent cyclic loading analysis, the RS stress field simulated by 6 mm of the HFMI treatment is applied as the

initial state of the simulations

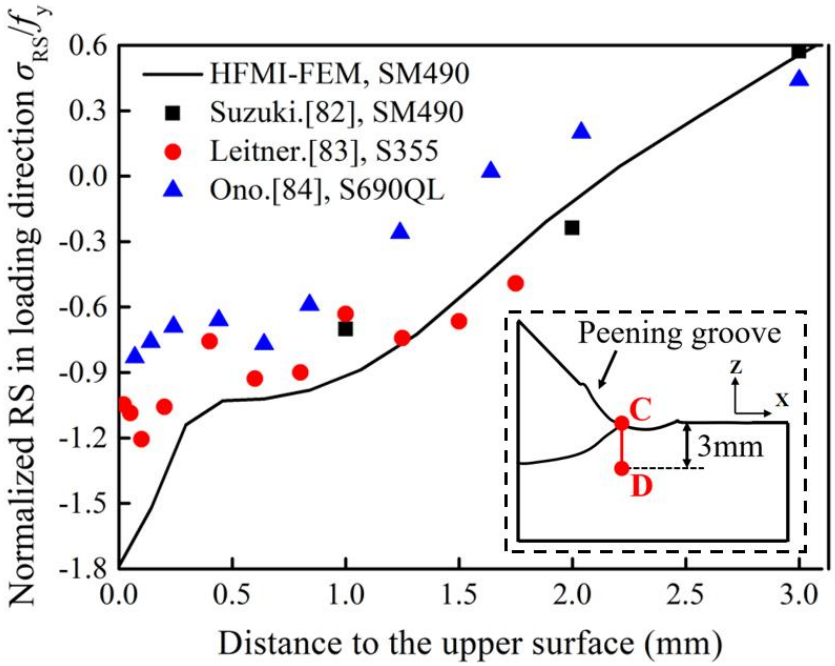

Fig. 5.10 Comparison of the predicted HFMI-induced RS Path CD and available measured data [82-84].

Table 5.4 Detailed information of HFMI specimen and RS measurement method from Ref. [82-84].

Ref.	Steel Grade (f_y)	Joint Type	Main Plate Thickness	Method of RS measurement
Suzuki. [82]	SM490 (≥ 325 MPa)	Cruciform	16 mm	Neutron diffraction
Leitner. [83]	S355 (≥ 350 MPa)	Cruciform	13 mm	X-ray diffraction
Ono. [84]	S690QL (832 MPa)	Cruciform	6 mm	Neutron diffraction

5.4.2 RS distribution after the fatigue load-cycle

Fig. 5.11 compares the RS distribution (σ_{xx}) near the weld toe before and after 3 load-cycles for AW and HFMI cases. It is observed that fatigue load-cycles lead to RS

relaxation for both AW and HFMI cases. For Case AW-3 ($\Delta\sigma$ = 0.47 f_y), the peak of tensile RS decreases from 510 MPa to 310 MPa. For Case HFMI-1 ($\Delta\sigma$ = 0.47 f_y), the peak of HFMI-induced compressive RS decreases from -694 MPa to -532 MPa. Fig. 5.11 (b) and (d) show the simulated local stress (σ_{xx}) cycle at the Point A and B. The results show that each stress cycle has almost the same peak stress and amplitude, indicating that stress relaxation induced by the constant-amplitude fatigue loading occurs mainly during the first cycle. Subsequent cycles are purely elastic cycles without plastic deformation. A similar phenomenon was reported in research by Leitner et al. [45]. They estimated the RS relaxation in HFMI-treated joints using experimental, analytical, and numerical methods, and found that the difference of redistributed RS between the case after the first load-cycle and 5th load-cycle was less than 5%. Therefore, FE analysis for 3 cycles of repetitive loading is sufficient to obtain all necessary stress parameters used for fatigue assessment.

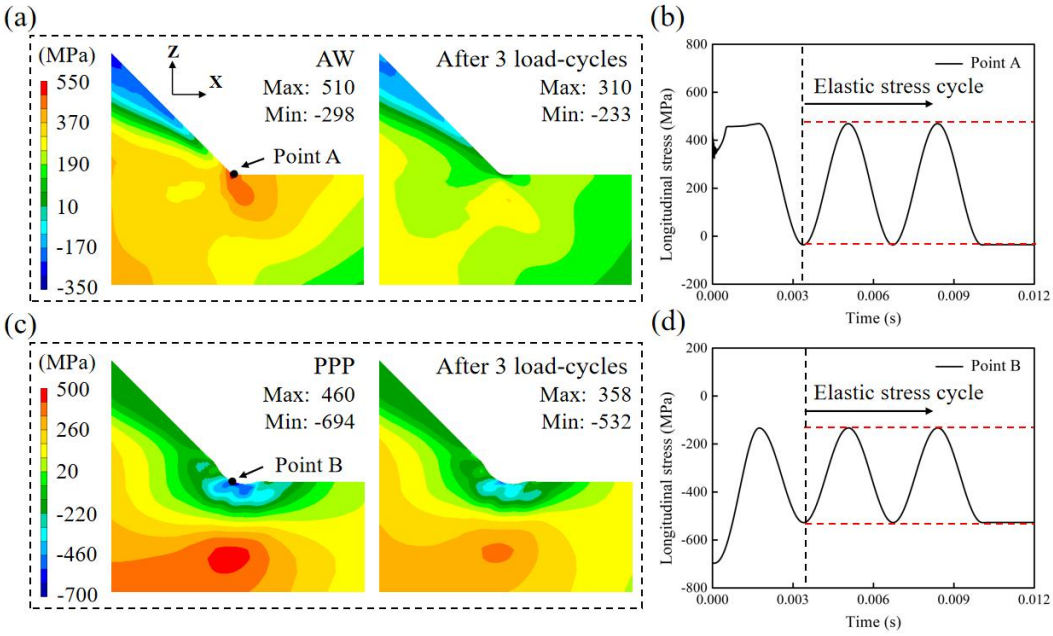

Fig.5.11 The distribution of longitudinal RS σ_{xx} near the weld toe before and after 3 load-cycles. (a) Case AW-3 ($\Delta\sigma$ = 0.47 f_y); (b) local stress cycle (σ_{xx}) at Point A; (c) Case HFMI-1 ($\Delta\sigma$ = 0.47 f_y); (d) local stress cycle (σ_{xx}) at Point B.

Fig.5.12 shows the longitudinal RS (σ_{xx}) distribution along the thickness direction after the first load-cycle for AW and HFMI cases. The degree of stress relaxation increases with the growing nominal stress range $\Delta\sigma$. For Case HFMI-6, stress

relaxation of about 70% occurs near the top surface after the 3rd load-cycle, while the peak tensile RS reduces from 510 MPa to -449 MPa for Case AW-6. Matsuoka et al. [16, 17] proposed an approximate estimation of the stable welding RS after fatigue loads (see Eq. (27)). However, this estimate is difficult to apply for specimens with complex stress states, such as HFMI cases. The EP-FE analysis of cyclic loading is a more accurate and reliable method to obtain local stress parameters used for fatigue analysis. These stress parameters incorporate the effects of the plastic deformation behavior of the material, RS, and load stress ratios.

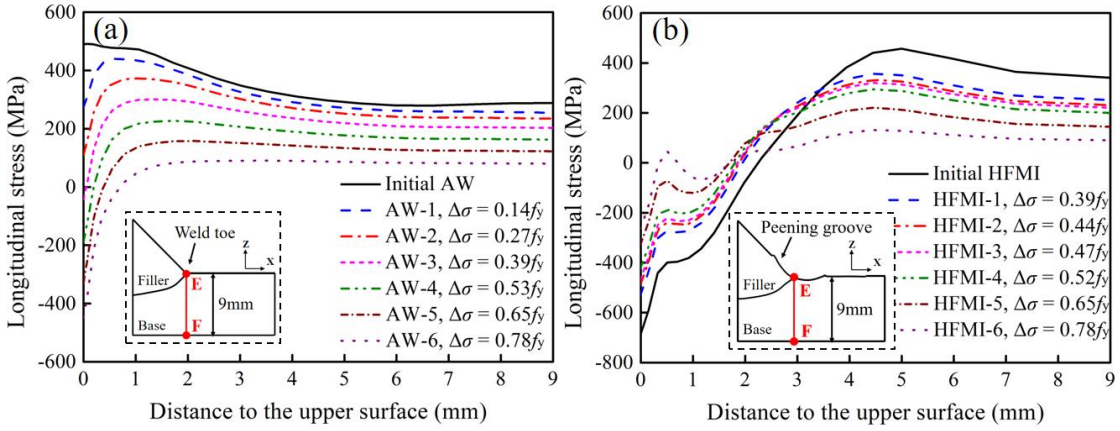

Fig. 5.12 Longitudinal RS (σ_{xx}) distribution along the thickness direction (Path EF) after a single load-cycle for (a) AW cases and (b) HFMI cases.

5.4.3 Nominal stress based S-N data

Fig. 5.13 shows the nominal stress-based S-N data and their regression curves for AW and HFMI conditions. All S-N data is tested under the constant-amplitude loading at stress ratio R = 0. According to the structural detail and yield strength (f_y = 388 MPa), the FAT for AW and HFMI specimens is classified as 71 and 125 following IIW recommendations [33], respectively. JSSC Class [22] for AW and HFMI specimens in this work are also added in Fig. 5.13. It can be seen that the S-N data of HFMI specimens is relatively scattered compared with the fatigue data from AW specimens. This is due to the uncertainty of the HFMI treatment, namely the slight differences in the shape of the peening groove and the introduced compressive RS between each specimen. The fatigue life of HFMI-treated joints is significantly improved compared to that in AW conditions. The fatigue strength at 2×10^6 cycles is increased from 80 MPa for AW cases to 164 MPa for HFMI cases. The corresponding slope of the

experimental S-N curve becomes slower. This indicates that HFMI parameters applied in the fabrication of the specimens are reasonable and can effectively increase the fatigue strength of gusset joints, although the hammering frequency of 80 Hz does not strictly conform to the IIW recommended > 90 Hz.

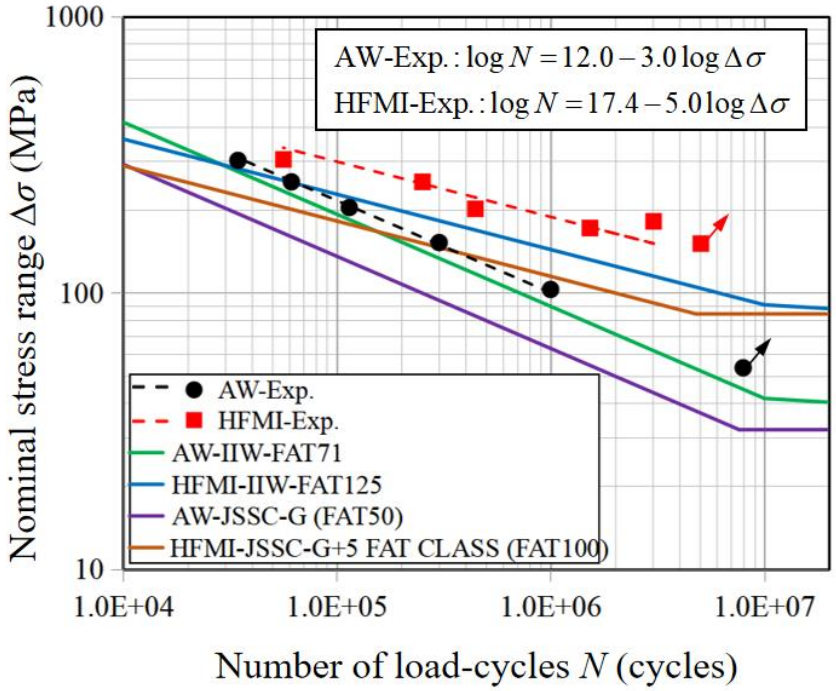

Fig. 5.13 Nominal stress based S-N data with the stress ratio R = 0 for AW and HFMI joints.

5.4.4 Calculation of LMES

Local stress response due to the cyclic load is obtained by EP-FE analysis as discussed in section 5.4.2. The tangential stress range $\Delta\sigma_t$ and the maximum tangential stress $\sigma_{t\text{-}max}$ on elements near the weld toe and peening groove is extracted from the cyclic load simulation results. The LMES range $\Delta\sigma_{eq}$ is then calculated using Eq. (28). Fig. 5.14 compares the $\Delta\sigma_{eq}$ distribution near the weld toe for AW and HFMI cases. It is observed that the maximum $\Delta\sigma_{eq}$ appears on Element 13 for both Case AW-3 with $\Delta\sigma$ = 0.47 fy and AW-6 with $\Delta\sigma$ = 0.78 f_y. For Case HFMI-1, however, there are two critical points at Element 4 and 15, and they shift to Element 14 with the growth of applied Δσ from 0.47 f_y to 0.78 f_y.

The location of the maximum Δσeq can be considered to be the possible crack

initiation site of specimens. The simulated distribution of $\Delta\sigma_{eq}$ suggests that the fatigue crack always emerges at the weld toe (Element 13) for AW cases. However, the crack initiation site for HFMI cases may shift when increasing the cyclic fatigue loads. For HFMI cases, the reason for the shift of crack initiation site may be the relaxation of compressive RS under the cyclic loads. For HFMI-1 with $\Delta\sigma$ = 0.47 f_y, local compressive stresses are not completely released, shifting the crack initiation site to the region close to the edges of the peening groove. However, more RS are released for HFMI-6 with $\Delta\sigma$ = 0.78 f_y, as shown in Fig. 5.12 (b). Therefore, the stress concentration becomes the major factor and together with compressive RS determines the location of crack initiation.

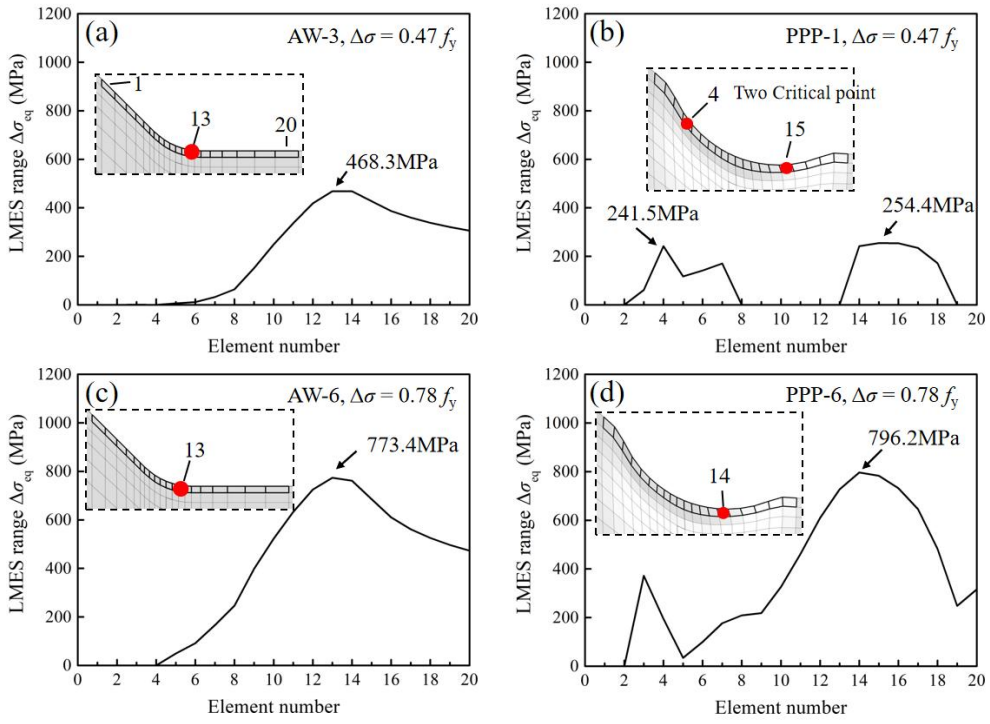

Fig. 5.14 The distribution of LMES range Δσeq near the weld toe for (a) AW-3 with $\Delta\sigma$ = 0.47 f_y, (b) HFMI-1 with $\Delta\sigma$ = 0.47 f_y, (c) AW-6 with $\Delta\sigma$ = 0.78 f_y, (b) HFMI-6 with $\Delta\sigma$ = 0.78 f_y.

Ono et al. [84] observed a similar shift of the crack initiation site. They investigated the crack initiation site of HFMI-treated high-strength steel welded joints using both experimental and damage-based numerical approaches and found that the initial HFMI-induced RS caused a crack initiation site on the boundary of the weld and HFMI groove when peak stress = 0.7 f_y. They also point out that the crack initiation site gradually

shifted from the edge to the middle of HFMI groove with increasing applied peak stress. Despite different material yield strengths, their experimental observations on the crack initiation site of HFMI-treated joints show a similar trend to numerical results in this study, which validates the proposed simulation model.

5.4.5 LMES based S-N data

Based on the maximum LMES range $\Delta\sigma_{eq}$ for each specimen, the LMES based S-N data and its regression curve are obtained, as shown in Fig. 5.15. Detailed information on stress parameters and fatigue test data is listed in Table 5.5. It can be seen that the fatigue data of AW and HFMI specimens essentially fall into the same band, which can be described by Eq. (29).

$$\log N = 19.6 - 5.2 \log \Delta\sigma_{eq} \tag{29}$$

Although the nominal S-N plot (Fig. 5.13) shows that the two types of joints have different regression curves, the LMES range versus life plot exhibits a potential that a single S-N curve can describe the fatigue lives of welded joints with different RS levels. This unified S-N curve enables a quantitative consideration of the RS on fatigue performance.

As mentioned before, the fatigue improvement by HFMI treatment is mainly contributed by three factors: introduced compressive RS, modification of the local weld toe geometry, and local grain refinement. For LMES approach, the used stress parameter $\Delta\sigma_{eq}$ is determined by the elastic-plastic local stress cycle which is calculated by EP-FE analysis using the fine FE mesh. Therefore, the effects of initial RS, cyclic stress relaxation, and local weld toe geometry on fatigue performance are automatically taken into account in the stress parameter $\Delta\sigma_{eq}$. However, the material parameter α in Eq. (26) is determined from AW specimens with various RS states[60, 61]. Here, the effect of the microstructural improvement of material is not considered in the determination of maximum $\Delta\sigma_{eq}$. Nevertheless, equivalent stress based S-N data for both AW and HFMI specimens show a good convergence to the single regression curve (Fig. 5.15), implying that the neglect of the microstructural improvement may be reasonable. Yamaguchi et al. [34] compared the fatigue improvement by three peening methods: needle peening (or HFMI peening), micro-needle peening, and shot peening.

They found that needle peening introduced a crack-like defect perpendicular to the treated surface, which offsets the improvement effects of the grain refinement on fatigue life enhancement. As stated above, process factors may cause uncertainty in terms of fatigue performance. Thus, further studies on peening-treated specimens with various process parameters are necessary to verify the reliability of the proposed method.

The local equivalent stress is calculated the based on local stress cycle that is simulated by elastic-plastic FE analysis of the HFMI treatment and cyclic loading processes. The S-N data for AW and HFMI specimens can be approximated by a single LMES-based S-N curve, which indicates that this local approach enables a quantitative evaluation of fatigue improvement by peening-induced RS. Since the effects of the material yield stress and load ratio on fatigue behaviors are related to local stress response, this local approach has the potential to combine fatigue data from different welded joints (made of steels with different yield strengths or tested under different load ratios) into a single S-N curve. But it still needs to be proved by further experiments and numerical investigations. Furthermore, the authors will investigate the fatigue life of HFMI-treated T-joints made of ultra-thick (> 50 mm) plates using the proposed LMES approach in future work.

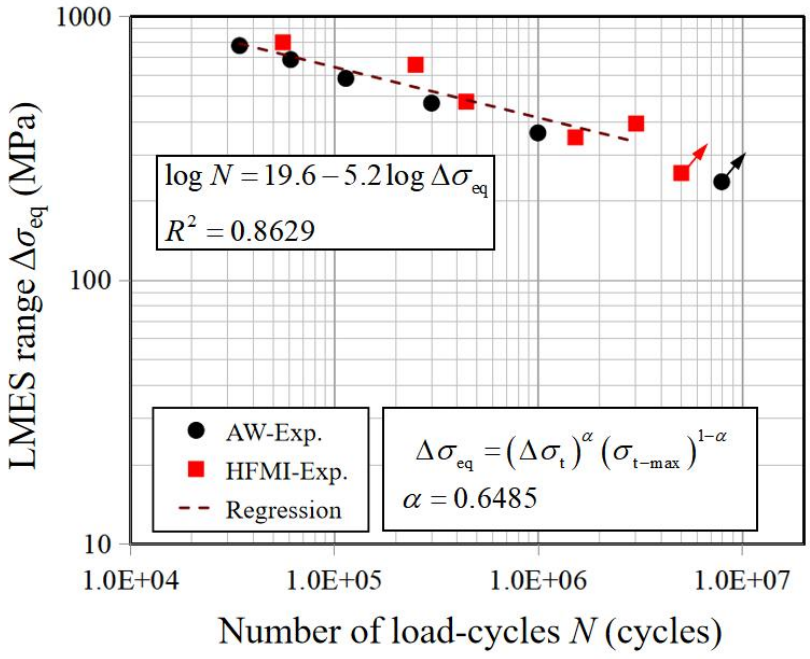

Fig. 5.15 LMES based S-N data for AW and HFMI joints.

Table 5.5 Fatigue test results and LMES results.(Stress radio R = 0)

Specimen Number	Nominal stress range $\Delta\sigma$ (MPa)	Maximum LMES range $\Delta\sigma_{eq}$ (MPa)	Number of cycles to complete failure N (cycle)	Crack initiation
AW-1	53.6	235.7	7957742	Run-out
AW-2	103.0	361.2	999855	Weld toe
AW-3	152.2	468.3	300969	Weld toe
AW-4	203.7	581.2	114328	Weld toe
AW-5	252.4	684.8	61319	Weld toe
AW-6	301.8	773.4	34462	Weld toe
HFMI-1	150.9	254.4	5043698	Run-out
HFMI-2	171.8	347.4	1527149	Weld toe
HFMI-3	181.6	392.0	3030539	Weld toe
HFMI-4	201.6	474.5	444621	Weld toe
HFMI-5	252.5	654.9	251510	Weld toe
HFMI-6	304.3	796.2	56217	Weld toe

5.5 Summary

In this work, the local equivalent stress approach is implemented to study the fatigue behavior of AW and HFMI-treated gusset joints made of SM490 steel. The LMES range $\Delta\sigma eq$ is determined by the elastic-plastic local stress cycle (tangential stress component) calculated by EP-FE analysis, and used for fatigue assessments. To ensure that the effects of initial RS, stress relaxation, and stress concentration due to weld toe geometry are contained in the elastic-plastic local stress cycle, muti-process simulations, including welding, HFMI treatment, and fatigue cyclic load processes, are performed. Fatigue tests for AW and HFMI joints were carried out. The local equivalent stress based S-N curve is obtained using the proposed approach and compared with the nominal stress based S-N data. The main conclusions of this paper are summarized below:

(1) For AW specimens, high tensile RS with σ_{xx} component of 510 MPa (1.30 f_y) occurred at the weld toe. After HFMI treatment, the non-uniform distributed compressive RS with a range of -400 to -694 MPa (-1.00 to -1.78 f_y) is introduced near the treated regions. The simulated AW stress and HFMI-induced RS agree with the measured one, which validates the muti-process numerical simulation procedures used.

(2) Stress relaxation behavior is observed numerically for AW and HFMI specimens subjected to cyclic loads. The stabled RS decreases gradually with the growth of the applied nominal stress range $\Delta\sigma$.

(3) The total lives to failure of the HFMI-treated specimens is significantly improved compared with the AW specimens. The fatigue strength at 2×10^6 cycles is increased from 80 MPa for AW cases to 164 MPa for HFMI cases based on the fatigue test.

(4) The location of the maximum MIL-HDBK-5D equivalent stress range $\Delta\sigma_{eq}$ at the surface of the peening groove changes under various magnitudes of load, which suggests a shift of the crack initiation site for HFMI-treated specimens. For AW cases, the crack initiation site is always located at the weld toe.

(5) Although the nominal stress S-N plot of the AW and HFMI joints have different S-N data trends, all S-N data are consolidated into a single curve by the local MIL-

HDBK-5D equivalent stress approach. This local equivalent S-N curve can be used for evaluating the fatigue life of welded joints treated by the HFMI process, considering the initial RS, cyclic stress relaxation, and local weld toe geometry.

CHAPTER 6

Conclusions

The objective of this study is to propose a multi-process numerical simulation model to estimate local RS and improved shape profiles induced by HFMI treatment in welded joints. Then, a local MIL-HDBK-5D equivalent stress (LMES) based fatigue assessment approach is proposed to investigate the fatigue lives of HFMI-treated gusset welded joints made of SM490. The LMES range is identified by the elastic-plastic local stress cycle simulated by the muti-process finite element analysis, including welding, HFMI, and fatigue loading processes. The main findings of this study are as follows.

(1) HFMI simulation on a flat plate:

a) The residual stress and peening groove profile obtained by flat plate peening simulation match well with the measurements, which shows the validity of the developed analysis method and employed input parameters.

b) Considerable compressive RS with peak of 686 MPa (σ_{xx}) and 725 MPa (σ_{yy}) is introduced by HFMI treatment in the vicinity of the treated zone.

c) The mesh sizes near the treated zone has a significant influence on HFMI-induced residual stresses. The ratio of element size in the treated region to the tool's tip radius should be less than 0.1

d) The peening length has a slight effect on residual stress. To save the analysis time, HFMI simulation of 6 mm is sufficient to obtain an reasonable stress distribution.

(2) HFMI simulation on a gusset welded joint:

a) The simulated welding thermal cycles, as-weld stress, HFMI-induced RS, and peening groove were in good agreement with the measurements. This indicates that the proposed simulation system can effectively predict the HFMI-induced RS with the consideration of the as-welded stress.

b) The proposed numerical analysis system allowed the use of the different FE mesh in the welding and HFMI simulation steps so that good computational efficiency and accuracy can be achieved.

c) The radius of the peening tool has been modified to enable more accurate

reproduction of the treated local profile. This facilitates the consideration of local stress concentrations and RS relaxation in subsequent fatigue assessment.

d) Considerable compressive RS (-700 MPa) near the weld toe was introduced after the HFMI treatment compared with the as-welded condition (500 MPa). To accurately evaluate the improvement by the HFMI process the fatigue life of the structures, it is needed to perform stress relaxation analyses after HFMI simulation and investigate the mean stress effect induced by the RS in future work.

(3) LMES based fatigue assessment for the post weld heat treated gusset welded joint:

a) The as-welded and stress-relieved RS obtained by thermal elastic-plastic FE analysis match well with the X-ray measured ones, which validates the developed analysis method and employed input parameters.

b) The RS level in stress-relieved joints decreased significantly compared with that in the as-welded condition, with its peak value dropping from 400 MPa to 65 MPa. The fatigue life of stress-relieved joints is approximately 2.5 times longer than as-welded ones with a stress ratio = -1.

c) The fatigue data of as-welded and PWHT specimens can be approximated by a single local equivalent stress based S-N curve. This reference SN-curve can be used for evaluating the fatigue life of welding joints at arbitrary RS and stress ratios.

(4) LMES based fatigue assessment for the HFMI-treated gusset welded joint:

a) For AW specimens, high tensile RS with σ_{xx} component of 510 MPa (1.30 f_y) occurred at the weld toe. After HFMI treatment, the non-uniform distributed compressive RS with a range of -400 to -694MPa (-1.00 to -1.78 f_y) is introduced near the treated regions. The simulated AW stress and HFMI-induced RS agree with the measured one, which validates the muti-process numerical simulation procedures used.

b) Stress relaxation behavior is observed numerically for AW and HFMI specimens subjected to cyclic loads. The stabled RS decreases gradually with the growth of the applied nominal stress range $\Delta\sigma$.

c) The total lives to failure of the HFMI-treated specimens is significantly improved compared with the AW specimens. The fatigue strength at 2×10^6 cycles is increased from 80 MPa for AW cases to 164 MPa for HFMI cases based on the fatigue test.

d) The location of the maximum MIL-HDBK-5D equivalent stress range $\Delta\sigma_{eq}$ at the surface of the peening groove changes under various magnitudes of load, which suggests a shift of the crack initiation site for HFMI-treated specimens. For AW cases, the crack initiation site is always located at the weld toe.

e) Although the nominal stress S-N plot of the AW and HFMI joints have different S-N data trends, all S-N data are consolidated into a single curve by the local MIL-HDBK-5D equivalent stress approach. This local equivalent S-N curve can be used for evaluating the fatigue life of welded joints treated by the HFMI process, considering the initial RS, cyclic stress relaxation, and local weld toe geometry.

Appendix

A The misalignment effect induced by angular welding distortion

The angular misalignment effects due to the welding distortion can be estimated by a stress magnification factor k_m [21], as below:

$$k_m = 1 + \frac{3\alpha_w l}{2T} \cdot \frac{\tanh(\beta/2)}{\beta/2} \tag{A1}$$

$$\beta = \frac{2l}{T} \cdot \sqrt{\frac{3\sigma_m}{E}} \tag{A2}$$

where α_w is the angular misalignment; σ_m is the membrane stress range; l is the distance from the weld to the fixed end of the main plate; T is the thickness of the main plate; E is the elastic modulus (210 GPa). For the gusset joint presented in this work, the angular distortion is less than 1 mm (α = 0.0036) from the experimental observation. The k_m under axial fatigue loads can be calculated, as listed in Table A1.

Table A1 Estimation of the stress magnification factor k_m

σ_m (MPa)	α_w	l (mm)	T (mm)	k_m
100	0.0036	125	9	1.069
200	0.0036	125	9	1.064
300	0.0036	125	9	1.060

According to k_m values, the angular misalignment effects on fatigue lives are less than 7%. In addition, the fatigue specimens subjected to different axial loads have a similar k_m value, which means the misalignment may lead to the translational shift of the SN curve but it does not affect the slope of the SN curve. Thus, the misalignment effects do not affect the main conclusions of this study.

B The effects of the boundary condition in the cyclic loading analysis on the local stress

The single-side gusset joint used in this work is not symmetry in the thickness direction. In cyclic loading simulation, however, a symmetry boundary condition (BC) in the lower back face was applied, as shown in Fig. B1 (a). This is due to the fact that the HFMI and the subsequent cyclic loading simulation were actually included in one simulation job, and it is difficult to change the BC during the analysis in Dytran.

To evaluate the BC effects, two elastic simulation cases with cyclic loads (Case1 with symmetry BC and Case 2 with a clamp BC) were performed by MSC. marc. The nominal stress range was $\Delta\sigma = 100$ MPa with a stress ratio $R = 0$. The initial stress for each element was set to 0. The hot-spot stress was evaluated by linear extrapolation [21] (Eq. B1).

$$\sigma_{hs} = 1.67\sigma_{0.4T} - 0.67\sigma_{1.0T} \tag{B1}$$

where σ_{hs} is the structural hot-spot stress; $\sigma_{0.4T}$ and $\sigma_{1.0T}$ are nodal stresses at two reference points 0.4T and 1.0T; T is the thickness of the main plate.

The simulated hot-spot stress range $\Delta\sigma_{hs}$ (Table A2) indicate that the effects of the BC are less than 3%, which can be ignored.

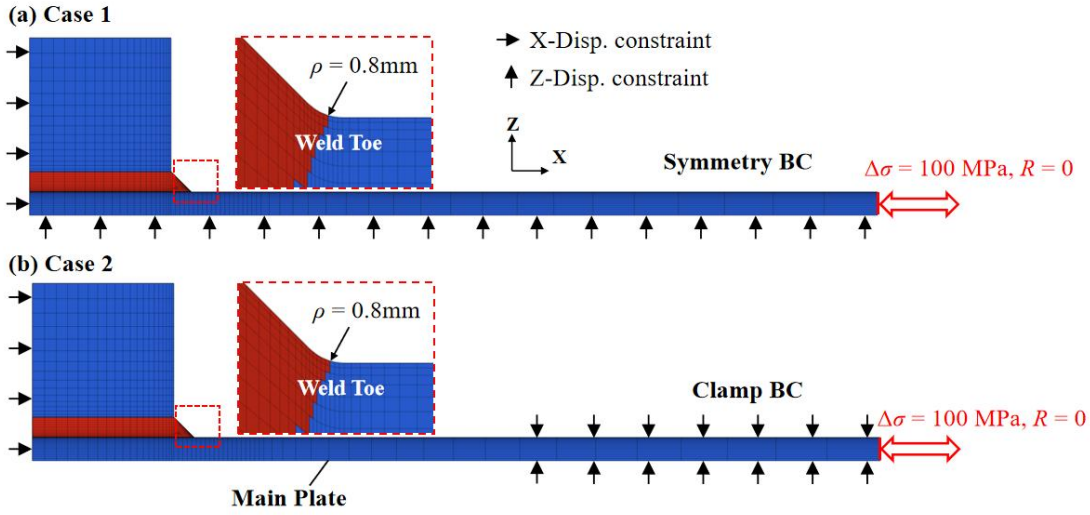

Fig. B1 Estimation of the hot-spot stress range $\Delta\sigma_{hs}$ based on elastic finite element analysis with (a) the symmetry boundary condition (BC) and (b) the clamp BC. For both cases, the nominal stress range $\Delta\sigma = 100$ MPa and stress ratio $R = 0$.

Table B1 Hot-spot stress range $\Delta\sigma_{hs}$ for Case 1 and Case 2

Case	BC	$\Delta\sigma$ (MPa)	R	$\Delta\sigma_{hs}$ (MPa)
1	Symmetry	100.0	0	142.9
2	Clamp	100.0	0	146.7

References

[1]T.L. Anderson, Fracture mechanics: fundamentals and application, Third Edit, Taylor & Francis Group, 2005.

[2]S. Subra, Fatigue of materials. Cambridge university press, 1998.

[3]M.J. Ottersböck, M. Leitner, M. Stoschka, W. Maurer, Effect of weld defects on the fatigue strength of ultra high-strength steels, Procedia Engineering, 2016;160:214-222. https://doi.org/10.1016/j.proeng.2016.08.883

[4]D. Radaj, C.M. Morris, W. Fricke. Fatigue assessment of welded joints by local approaches, second ed., Woodhead publishing, 2006.

[5]S.J. Maddox, Fatigue strength of welded structures, second ed., Abington Publishing, Cambridge, 1991.

[6]H.L.J. Pang, Analysis of weld toe profiles and weld toe cracks, International journal of fatigue, 1993;15(1):31-36. https://doi.org/10.1016/0142-1123(93)90074-Z

[7]C.Y. Hou, Fatigue analysis of welded joints with the aid of real three-dimensional weld toe geometry, International Journal of Fatigue, 2007;29(4):772-785. https://doi.org/10.1016/j.ijfatigue.2006.06.007

[8]K. Rother, W. Fricke, Effective notch stress approach for welds having low stress concentration, International Journal of Pressure Vessels and Piping, 2016;147:12-20. https://doi.org/10.1016/j.ijpvp.2016.09.008

[9]M.J. Ottersböck, M. Leitner, M. Stoschka, Characterisation of actual weld geometry and stress concentration of butt welds exhibiting local undercuts, Engineering Structures, 2021;240:112266. https://doi.org/10.1016/j.engstruct.2021.112266

[10] G. Meneghetti, P. Lazzarin, The peak stress method for fatigue strength assessment of welded joints with weld toe or weld root failures, Welding in the World, 2011;55:22-29. https://doi.org/10.1007/BF03321304

[11] F. Berto, A. Campagnolo, F. Chebat, M. Chebat, M. Cincera, M. Santini, Fatigue strength of steel rollers with failure occurring at the weld root based on the local strain energy values: modelling and fatigue assessment, International Journal of Fatigue, 2016;82:643-657. https://doi.org/10.1016/j.ijfatigue.2015.09.023

[12] H.R. Raftar, E. Dabiri, A. Ahola, T. Björk,Weld root fatigue assessment of load-carrying fillet welded joints: 4R method compared to other methods, International Journal of Fatigue, 2022;156:106623. https://doi.org/10.1016/j.ijfatigue.2021.106623

[13] W. Fricke, IIW guideline for the assessment of weld root fatigue, Welding in the World, 2013;57:753-791. https://doi.org/10.1007/s40194-013-0066-y

[14] S.J. Maddox, Recent advances in the fatigue assessment of weld imperfections, Welding journal 1993;72(7):42-51.

[15] M.A. Wahab, M.S. Alam, The significance of weld imperfections and surface peening on fatigue crack propagation life of butt-welded joints, Journal of Materials Processing Technology, 2004;153:931-937. https://doi.org/10.1016/j.jmatprotec.2004.04.150

[16] T. Lassen, N. Recho, Fatigue life analyses of welded structures: flaws, John Wiley & Sons, 2013.

[17] R.M. Andrews, The effect of misalignment on the fatigue strength of welded cruciform joints, Fatigue & Fracture of Engineering Materials & Structures, 1996;19(6):755-768. https://doi.org/10.1111/j.1460-2695.1996.tb01320.x

[18] J.M. Ferreira, C.M. Branco, Influence of misalignment on the fatigue strength of butt welds, International journal of fatigue, 1991;13(5):405-409. https://doi.org/10.1016/0142-1123(91)90597-R

[19] W. Zhou, P. Dong, An analytical method for consistent treatment of axial and angular misalignments in fatigue evaluation of welded joints, Thin-Walled Structures, 2022;173:109003. https://doi.org/10.1016/j.tws.2022.109003

[20] I. Lotsberg, Assessment of the size effect for use in design standards for fatigue analysis, International journal of fatigue, 2014;66:86-100.

[21] A.F. Hobbacher, Recommendations for fatigue design of welded joints and components, Springer International Publishing, Switzerland, 2016. https://doi.org/10.1007/978-3-319-23757-2

[22] Japanese Society of Steel Construction, Fatigue design recommendations for steel structures, Gihodo; 2012 (in Japanese).

[23] Z. Feng, Processes and mechanisms of welding residual stress and distortion. Elsevier,

2005.

[24] Ueda Y, Murakawa H, Ma N, Welding deformation and residual stress prevention. 1st ed. New York: Elsevier, 2012.

[25] L.E. Lindgren, H. Runnemalm, M.O. Näsström, Simulation of multipass welding of a thick plate, International journal for numerical methods in engineering 1999;44(9):1301-1316. https://doi.org/10.1002/(SICI)1097-0207(19990330)44:9<1301::AID-NME479>3.0.CO;2-K

[26] L.J. Zhang, J.X. Zhang, A. Gumenyuk, M. Rethmeier, S.J. Na, Numerical simulation of full penetration laser welding of thick steel plate with high power high brightness laser, Journal of materials processing technology, 2014;214(8):1710-1720. https://doi.org/10.1016/j.jmatprotec.2014.03.016

[27] J. Krebs, M. Kassner, Influence of welding residual stresses on fatigue design of welded joints and components, Welding in the World, 2007;51(7):54-68. https://doi.org/10.1007/BF03266586

[28] J.C. Pang, S.X. Li, Z.G. Wang, Z.F. Zhang, General relation between tensile strength and fatigue strength of metallic materials, Materials Science and Engineering: A, 2013;564:331-341. https://doi.org/10.1016/j.msea.2012.11.103

[29] J.D.M. Costa, J.A.M. Ferreira, L.P.M. Abreu, Fatigue behaviour of butt welded joints in a high strength steel, Procedia Engineering, 2010;2(1):697-705. https://doi.org/10.1016/j.proeng.2010.03.075

[30] H. Guo, J. Wan, Y. Liu, J. Hao, Experimental study on fatigue performance of high strength steel welded joints, Thin-Walled Structures, 2018;131:45-54. https://doi.org/10.1016/j.tws.2018.06.023

[31] P.J. Haagensen, S.J. Maddox, IIW recommendations on methods for improving the fatigue strength of welded joints, first ed. Woodhead Publishing, Cambridge, 2013; 29-37. https://doi.org/10.1016/B978-1-78242-064-4.50009-3

[32] W.L. Chan, K.F. Cheng, Hammer peening technology—the past, present, and future, The International Journal of Advanced Manufacturing Technology, 2022;118:683-701. https://doi.org/10.1007/s00170-021-07993-5

[33] G.B. Marquis, Z. Barsoum, IIW recommendations for the HFMI treatment, first ed., Springer, Singapore, 2016. https://doi.org/10.1007/978-981-10-2504-4

[34] N. Yamaguchi, T. Shiozaki, Y. Tamai, Micro-needle peening method to improve fatigue strength of arc-welded ultra-high strength steel joints, Journal of Materials Processing Technology, 2021;288:116894. https://doi.org/10.1016/j.jmatprotec.2020.116894

[35] R. Baptista, V. Infante, C. Branco, Fully dynamic numerical simulation of the hammer peening fatigue life improvement techniqu, Procedia Engineering, 2011;10:1943-1948. https://doi.org/10.1016/j.proeng.2011.04.322

[36] Y. Hu, L. Shen, S. Nie, B. Yang, W. Sha, FE simulation and experimental tests of high-strength structural bolts under tension, Journal of Constructional Steel Research, 2016;126:174-186. https://doi.org/10.1016/j.jcsr.2016.07.021

[37] C. Deng, Y. Liu, B. Gong, D. Wang, Numerical implementation for fatigue assessment of butt joint improved by high frequency mechanical impact treatment: A structural hot spot stress approach, International Journal of Fatigue, 2016;92:211-219. https://doi.org/10.1016/j.ijfatigue.2016.07.008

[38] C. Ernould, J. Schubnell, M. Farajian, A. Maciolek, D. Simunek, M. Leitner, M. Soschka, Application of different simulation approaches to numerically optimize high-frequency mechanical impact (HFMI) post-treatment process, Welding in the World, 2019;63(3):725-738. https://doi.org/10.1007/s40194-019-00701-8

[39] J. Schubnell, C. Eichheimer, C. Ernould, A. Maciolek, J. Rebelo-Kornmeier, M. Farajian, The influence of coverage for high frequency mechanical impact treatment of different steel grades, Journal of Materials Processing Technology, 2020;277:116437. https://doi.org/10.1016/j.jmatprotec.2019.116437

[40] V. Hardenacke, M. Farajian, D. Siegele, Modelling and simulation of High frequency mechanical impact (HFMI) treatment of welded joints, 68th IIW Annual Assembly, IIW Document XIII-2533-14, 2015.

[41] H. Ruiz, N. Osawa, S. Rashed, A practical analysis of residual stresses induced by high-frequency mechanical impact post-weld treatment, Welding in the World, 2019;63(5):1255-1263. https://doi.org/10.1007/s40194-019-00753-w

[42] J. Foehrenbach, V. Hardenacke, M. Farajian, High frequency mechanical impact treatment (HFMI) for the fatigue improvement: numerical and experimental investigations to describe the condition in the surface layer, Welding in the World,

2016;60(4):749-755. https://doi.org/10.1007/s40194-016-0338-4

[43] M. Khurshid, M. Leitner, Z. Barsoum, C. Schneider, Residual stress state induced by high frequency mechanical impact treatment in different steel grades–Numerical and experimental study, International Journal of Mechanical Sciences, 2017;123:34-42. https://doi.org/10.1016/j.ijmecsci.2017.01.027

[44] Y. Banno, K. Kinoshita, Z. Barsoum, Numerical investigation of influence of under- and over-treatment on residual stress state induced by HFMI, Welding in the World, 2021;65(11):2135-2146. https://doi.org/10.1007/s40194-021-01159-3

[45] M. Leitner, M. Khurshid, Z. Barsoum, Stability of high frequency mechanical impact (HFMI) post-treatment induced residual stress states under cyclic loading of welded steel joints, Engineering Structures, 2017;143:589-602. https://doi.org/10.1016/j.engstruct.2017.04.046

[46] J. Schubnell, E. Carl, M. Farajian, S. Gkatzogiannis, P. Knodel, T. Ummenhofer, R. Wimpory, H. Eslami, Residual stress relaxation in HFMI-treated fillet welds after single overload peaks, Welding in the World, 2020;64(6):1107-1117. https://doi.org/10.1007/s40194-020-00902-6

[47] H. Ruiz, N. Osawa, S. Rashed, Study on the stability of compressive residual stress induced by high-frequency mechanical impact under cyclic loadings with spike loads, Welding in the World, 2020;64(11):1855-1865. https://doi.org/10.1007/s40194-020-00965-5

[48] H.C. Yildirim, G.B. Marquis, Z. Barsoum, Fatigue assessment of high frequency mechanical impact (HFMI)-improved fillet welds by local approaches, International Journal of Fatigue, 2013;52:57-67. https://doi.org/10.1016/j.ijfatigue.2013.02.014

[49] H.C. Yıldırım, G.B. Marquis, Fatigue design of axially-loaded high frequency mechanical impact treated welds by the effective notch stress method, Materials & Design, 2014;58:543-550. https://doi.org/10.1016/j.matdes.2014.02.001

[50] M. Leitner, M. Stoschka, W. Eichlseder, Fatigue enhancement of thin-walled, high-strength steel joints by high-frequency mechanical impact treatment, Welding in the World, 2014;58: 29-39. https://doi.org/10.1007/s40194-013-0097-4

[51] M. Leitner, Z. Barsoum, Effect of increased yield strength, R-ratio, and plate thickness on the fatigue resistance of high-frequency mechanical impact (HFMI)–treated steel

joints, Welding in the World 2020;64(7):1245-1259. https://doi.org/10.1007/s40194-020-00914-2

[52] M. Leitner, M. Stoschka, Effect of load stress ratio on nominal and effective notch fatigue strength assessment of HFMI-treated high-strength steel cover plates, International Journal of Fatigue, 2020;139:105784. https://doi.org/10.1016/j.ijfatigue.2020.105784

[53] K. Yuan, Y. Sumi, Simulation of residual stress and fatigue strength of welded joints under the effects of ultrasonic impact treatment (UIT), International Journal of Fatigue, 2016;92:321-332. https://doi.org/10.1016/j.ijfatigue.2016.07.018

[54] H. Al-Karawi, R.U.F. von Bock und Polach, M. Al-Emrani, Fatigue life extension of existing welded structures via high frequency mechanical impact (HFMI) treatment, Engineering Structures, 2021;239:112234. https://doi.org/10.1016/j.engstruct.2021.112234

[55] A. Ince, Computational crack propagation modeling of welded structures under as-welded and high frequency mechanical impact (HFMI) treatment conditions, Fatigue & Fracture of Engineering Materials & Structures, 2022;45(2):578-592. https://doi.org/10.1111/ffe.13619

[56] T. Nicholas, J.R. Zuiker, On the use of the Goodman diagram for high cycle fatigue design, International Journal of Fracture, 1996;80:219-235. https://doi.org/10.1007/BF00012670

[57] M.H.H. Shen, Reliability assessment of high cycle fatigue design of gas turbine blades using the probabilistic Goodman Diagram, International journal of fatigue, 1999;21(7):699-708. https://doi.org/10.1016/S0142-1123(99)00033-X

[58] T.J. George, M.H.H. Shen, O. Scott-Emuakpor, T. Nicholas, C.J. Cross, J. Calcaterra, Goodman diagram via vibration-based fatigue testing, Journal of Engineering Materials and Technology, 2005;127(1):58-64. https://doi.org/10.1115/1.1836791

[59] Military Standardization Handbook: Metallic Materials and Elements for Aerospace Vehicle Structures, MIL-HDBK-5D, USAF, 1983:16-18.

[60] K. Matsuoka, E. Fujii, An Evaluation Method on Fatigue Crack Initiation Life at Welded Joints in Steel Structures, Journal of the Japan Society of Naval Architects and Ocean Engineers, 1995;178:513-522.

https://doi.org/10.2534/jjasnaoe1968.1995.178_513

[61] N. Yamamoto, K. Matsuoka, Fatigue assessment method considering an effect of mean stress, Journal of the Japan Society of Naval Architects and Ocean Engineers, 2001;190:499-505. https://doi.org/10.2534/jjasnaoe1968.2001.190_499

[62] J. Wang, M. Shibahara, X. Zhang, H. Murakawa, Investigation on twisting distortion of thin plate stiffened structure under welding, Journal of Materials Processing Technology, 2012;212(8):1705-1715. https://doi.org/10.1016/j.jmatprotec.2012.03.015

[63] S. Ren, Y. Ma, N. Ma, S. Saeki, Y. Iwamotob, 3-D modelling of the coaxial one-side resistance spot welding of AL5052/CFRP dissimilar material, Journal of Manufacturing Processes, 2021;68:940-950. https://doi.org/10.1016/j.jmapro.2021.06.023

[64] R. Nishimura, N. Ma, Y. Liu, W. Li, T. Yasuki, Measurement and analysis of welding deformation and residual stress in CMT welded lap joints of 1180 MPa steel sheets, Journal of Manufacturing Processes, 2021;72:515-528. https://doi.org/10.1016/j.jmapro.2021.10.050

[65] H. Ruiz, N. Osawa, H. Mutakawa, S. Rashed, Stability of compressive residual stress introduced by HFMI technique, 37th International Conference on Ocean, Offshore and Arctic Engineering. Volume 4: Materials Technology, 2018. https://doi.org/10.1115/OMAE2018-77887

[66] J. Sun, X. Liu, Y. Tong, D. Deng, A comparative study on welding temperature fields, residual stress distributions and deformations induced by laser beam welding and CO2 gas arc welding, Materials & Design, 2014;63:519-530. https://doi.org/10.1016/j.matdes.2014.06.057

[67] ASME BPVC Committee on Materials, ASME Boiler & Pressure Vessel Code, Section II Materials, Part D Properties (Metric), The American Society of Mechanical Engineers, New York, 2015;757-791.

[68] J. Sun, J. Hensel, J. Klassen, T. Nitschke-Pagel, K. Dilger, Solid-state phase transformation and strain hardening on the residual stresses in S355 steel weldments, Journal of Materials Processing Technology, 2019;265:173-184. https://doi.org/10.1016/j.jmatprotec.2018.10.018

[69] L. Tang, A. Ince, J. Zheng, Numerical modeling of residual stresses and fatigue damage assessment of ultrasonic impact treated 304L stainless steel welded joints, Engineering Failure Analysis, 2020;108:104277. https://doi.org/10.1016/j.engfailanal.2019.104277

[70] J.L. Chaboche, Time-independent constitutive theories for cyclic plasticity, International Journal of Plasticity, 1986;2(2):149-188. https://doi.org/10.1016/0749-6419(86)90010-0

[71] S. Hu, C. Guo, D. Wang, Z. Wang, 3D dynamic finite element analysis of the nonuniform residual stress in ultrasonic impact treatment process, Journal of Materials Engineering and Performance, 2016;25(9):4004-4015. https://doi.org/10.1007/s11665-016-2206-1

[72] E. Bressert, SciPy and NumPy: an overview for developers, first ed. O'Reilly Media, Sebastopol, 2012; 22-25.

[73] J. Schubnell, V. Hardenacke, M. Farajian, Strain-based critical plane approach to predict the fatigue life of high frequency mechanical impact (HFMI)-treated welded joints depending on the material condition, Welding in the World, 2017;61:1199-1210. https://doi.org/10.1007/s40194-017-0505-2

[74] J. Sun, T. Nitschke-Pagel, K. Dilger, Influence of temperature-and phase-dependent yield strength on residual stresses in ultra-high strength steel S960 weldments, Journal of Materials Research and Technology, 2021;15:1854-1872. https://doi.org/10.1016/j.jmrt.2021.09.050

[75] E. Mikkola, H. Remes, G. Marquis, A finite element study on residual stress stability and fatigue damage in high-frequency mechanical impact (HFMI)-treated welded joint, International Journal of Fatigue, 2017;94:16-29. https://doi.org/10.1016/j.ijfatigue.2016.09.009

[76] H. Murakawa, I. Oda, S. Ito, H. Serizawa, M. Shibahara, H. Nishikawa, Iterative Substructure Method for Fast Computation of Thermal Elastic Plastic Welding Problems, Journal Kansai Society of Naval Architects Japan, 2005;243:67-70.

[77] H. Nishikawa, H. Serizawa, H. Murakawa, Actual Application of Large-scaled FEM for Analysis of Mechanical Problems in Welding, Quarterly Journal of the Japan Welding Society, 2006;24:168-173.

[78] K.G.O. Odquist, J. Hult, Kriechfestigkeit metallischer Werkstoffe, Springer, 1962.

[79] W. Fricke, IIW recommendations for the fatigue assessment of welded structures by notch stress analysis: IIW-2006-09. Woodhead Publishing, 2012.

[80] P. Dai, P.M. Kyaw, N. Osawa, S. Rashed, D. Ma, J. Okada, M. Honnami, Numerical study on local residual stresses induced by high frequency mechanical impact post-weld treatment using the optimized displacement-controlled simulation method, Journal of Manufacturing Processes, 2023;92:262-271. https://doi.org/10.1016/j.jmapro.2023.03.002

[81] N. Yamamoto, Fatigue evaluation of ship structures considering change in mean stress condition, Welding in the World, 2017;61:987-995. https://doi.org/10.1007/s40194-017-0461-x

[82] T. Suzuki, T. Okawa, H. Shimanuki, T. Nose, N. Ohta, H. Suzuki, A. Moriai, Effect of ultrasonic impact treatment (UIT) on fatigue strength of welded joints, Advanced Materials Research, 2014;996:736-742. https://doi.org/10.4028/www.scientific.net/AMR.996.736

[83] M. Leitner, W. Mössler, A. Putz, M. Stoschka, Effect of post-weld heat treatment on the fatigue strength of HFMI-treated mild steel joints, Welding in the World, 2015;59:861-873. https://doi.org/10.1007/s40194-015-0265-9

[84] Y. Ono, H. Yıldırım, K. Kinoshita, A. Nussbaumer, Damage-based assessment of the fatigue crack initiation site in high-strength steel welded joints treated by HFMI, Metals, 2022;12(1):145. https://doi.org/10.3390/met12010145

Publications related to this Thesis

Publications with full or peer review

1. **Dai, P.**, Kyaw, P. M., Ma, D., Okada, J., Honnami, M., Rashed, S., Osawa, N. Proposal on a Practical Numerical Simulation Technique of HFMI Treatment for Welded Joints. In The 32nd International Ocean and Polar Engineering Conference, 2022.
2. **Dai, P.**, Kyaw, P. M., Osawa, N., Rashed, S., Ma, D., Okada, J., Honnami, M. Numerical study on local residual stresses induced by high frequency mechanical impact post-weld treatment using the optimized displacement-controlled simulation method. Journal of Manufacturing Processes, 2023, 92, 262-271.
3. **Dai, P.**, Kagase, T., Osawa, N., Yoshihara, Y., Study on the Estimation Method for Welding Fatigue Mean Stress Effect Based on Local Elastic-Plastic Stress Cycle. In The 33rd International Ocean and Polar Engineering Conference, 2023.
4. Yoshihara, Y., Osawa, N., Murakawa, H., **Dai, P.,** Study on the Estimation Method for Welding Fatigue Mean Stress Effect Independently from Failure Mode and Joint Type, Journal of the Japan Society of Naval Architects and Ocean Engineers, 2023, 36, 69-79.

Conference proceedings

1. Numerical study on the effect of peening analysis condition on HFMI-induced local residual stresses, IIW annual assembly conference. XIII-2952-2022, 2022.
2. Numerical study on the effect of peening tool's movement on deformed profile and HFMI-induced residual stresses, IIW international conference, 2022.

Publication under review

1. **Dai, P.,** Osawa, N., Rashed, S., Ma, D., Okada, J., Honnami, M., Local MIL-HDBK-5D Equivalent Stress Based Fatigue Assessment of the Gusset Welded Joint Improved by Portable Pneumatic Needle-Peening Treatment, International Journal of Fatigue.